Tectonic and climatic control on the evolution of the Himalayan mountain front

A case study from the Kangra intermontane basin and the Dhauladhar range in the Northwestern Himalaya

Dissertation
vorgelegt von

Saptarshi Dey

Kumulative Dissertation zur Erlangung der Würde des akademischen Grades
Doktor Rerum Naturalium (Dr. rer. Nat)

In der Wissenschaftdisziplin

Geologie

Eingereicht am Institut für Erd- und Umweltwissenschaften der
Mathematisch-Naturwissenschaftlichen Fakultät der Universität Potsdam

Potsdam, August 2016

Declaration

This work has not been submitted to any other institution of higher education and has been carried out with the support of dedicated research funds provided by the graduate training center **DFG-GRK1364** (‘*Shaping Earth’s Surface in a Variable Environment: Interactions between tectonics, climate and biosphere in the African-Asian monsoonal region*’ financed by Deutsche Forschungsgemeinschaft) and additional support by the **Research Focus Earth Sciences** (RFES) of Universität Potsdam.

Potsdam, 24.08.2016

Saptarshi Dey

To

Those who teach me every little step in life and bring a smile to my face…

'Education is the manifestation of the perfection already in man'

- Swami Vivekananda (1894)

Table of contents

List of figures

Figures in Appendices

List of Tables

Abstract

Variations in the distribution of mass within an orogen may lead to transient sediment storage, which in turn might affect the state of stress and the level of fault activity. Distinguishing between different forcing mechanisms causing variations of sediment flux and tectonic activity, is therefore one of the most challenging tasks in understanding the spatiotemporal evolution of active mountain belts.

The Himalayan mountain belt is one of the most significant Cenozoic collisional mountain belt, formed due to collision between northward-bound Indian Plate and the Eurasian Plate during the last 55-50 Ma. Ongoing convergence of these two tectonic plates is accommodated by faulting and folding within the Himalayan arc-shaped orogen and the continued lateral and vertical growth of the Tibetan Plateau and mountain belts adjacent to the plateau as well as regions farther north. Growth of the Himalayan orogen is manifested by the development of successive south-vergent thrust systems. These thrust systems divide the orogen into different morphotectonic domains. From north to south these thrusts are the Main Central Thrust (MCT), the Main Boundary Thrust (MBT) and the Main Frontal Thrust (MFT). The growing topography interacts with moisture-bearing monsoonal winds, which results in pronounced gradients in rainfall, weathering, erosion and sediment transport toward the foreland and beyond. However, a fraction of this sediment is trapped and transiently stored within the intermontane valleys or 'dun's within the lower-elevation foothills of the range. Improved understanding of the spatiotemporal evolution of these sediment archives could provide a unique opportunity to decipher the triggers of variations in sediment production, delivery and storage in an actively deforming mountain belt and support efforts to test linkages between sediment volumes in intermontane basins and changes in the shallow crustal stress field. As sediment redistribution in mountain belts on timescales of 10^2-10^4 years can effect cultural characteristics and infrastructure in the intermontane valleys and may even impact the seismotectonics of a mountain belt, there is a heightened interest in understanding sediment-routing processes and causal relationships between tectonism, climate and topography. It is here at the intersection between tectonic processes and superposed climatic and sedimentary processes in the Himalayan orogenic wedge, where my investigation is focused on. The study area is the intermontane Kangra Basin in the northwestern Sub-Himalaya, because the characteristics of the different Himalayan morphotectonic provinces are well developed, the area is part of a region strongly influenced by monsoonal forcing, and the existence of numerous fluvial terraces provides excellent strain markers to assess deformation processes within the Himalayan orogenic wedge. In addition, being located in front of the Dhauladhar Range the region is characterized by pronounced gradients in past and present-day erosion and sediment processes associated with repeatedly changing climatic conditions. In light of these conditions I analyzed climate-driven late Pleistocene-Holocene sediment cycles in this tectonically active region, which may be responsible for triggering the tectonic re-organization within the Himalayan orogenic wedge, leading to out-of-sequence thrusting, at least since early Holocene.

The Kangra Basin is bounded by the MBT and the Sub-Himalayan Jwalamukhi Thrust (JMT) in the north and south, respectively and transiently stores sediments derived from the Dhauladhar Range. The

Basin contains ~200-m-thick conglomerates reflecting two distinct aggradation phases; following aggradation, several fluvial terraces were sculpted into these fan deposits. ^{10}Be CRN surface exposure dating of these terrace levels provides an age of 53.4±3.2 ka for the highest-preserved terrace (AF1); subsequently, this surface was incised until ~15 ka, when the second fan (AF2) began to form. AF2 fan aggradation was superseded by episodic Holocene incision, creating at least four terrace levels. We find a correlation between variations in sediment transport and ∂_{18}O records from regions affected by the Indian Summer Monsoon (ISM). During strengthened ISMs sand post-LGM glacial retreat, aggradation occurred in the Kangra Basin, likely due to high sediment flux, whereas periods of a weakened ISM coupled with lower sediment supply coincided with renewed re-incision.

However, the evolution of fluvial terraces along Sub-Himalayan streams in the Kangra sector is also forced by tectonic processes. Back-tilted, folded terraces clearly document tectonic activity of the JMT. Offset of one of the terrace levels indicates a shortening rate of 5.6±0.8 to 7.5±1.0 mm.a^{-1} over the last ~10 ka. Importantly, my study reveals that late Pleistocene/Holocene out-of-sequence thrusting accommodates 40-60% of the total 14±2 mm.a^{-1} shortening partitioned throughout the Sub-Himalaya. Importantly, the JMT records shortening at a lower rate over longer timescales hints towards out-of-sequence activity within the Sub-Himalaya. Re-activation of the JMT could be related to changes in the tectonic stress field caused by large-scale sediment removal from the basin. I speculate that the deformation processes of the Sub-Himalaya behave according to the predictions of critical wedge model and assume the following: While >200m of sediment aggradation would trigger foreland-ward propagation of the deformation front, re-incision and removal of most of the stored sediments (nearly 80-85% of the optimum basin-fill) would again create a sub-critical condition of the wedge taper and trigger the retreat of the deformation front.

While tectonism is responsible for the longer-term processes of erosion associated with steepening hillslopes, sediment cycles in this environment are mainly the result of climatic forcing. My new ^{10}Be cosmogenic nuclide exposure dates and a synopsis of previous studies show the late Pleistocene to Holocene alluvial fills and fluvial terraces studied here record periodic fluctuations of sediment supply and transport capacity on timescales of 10^3 to 10^5 years. To further evaluate the potential influence of climate change on these fluctuations, I compared the timing of aggradation and incision phases recorded within remnant alluvial fans and terraces with continental climate archives such as speleothems in neighboring regions affected by monsoonal precipitation. Together with previously published OSL ages yielding the timing of aggradation, I find a correlation between variations in sediment transport with oxygen-isotope records from regions affected by the Indian Summer Monsoon (ISM). Accordingly, during periods of increased monsoon intensity (transitions from dry and cold to wet and warm periods – MIS4 to MIS3 and MIS2 to MIS1) (MIS=marine isotope stage) and post-Last Glacial Maximum glacial retreat, aggradation occurred in the Kangra Basin, likely due to high sediment flux. Conversely, periods of weakened monsoon intensity or lower sediment supply coincide with re-incision of the existing basin-fill.

Finally, my study entails part of a low-temperature thermochronology study to assess the youngest exhumation history of the Dhauladhar Range. Zircon helium (ZHe) ages and existing low-temperature data sets (ZHe, apatite fission track (AFT)) across this range, together with 3D thermokinematic modeling (PECUBE) reveals constraints on exhumation and activity of the range-bounding Main Boundary Thrust (MBT) since at least mid-Miocene time. The modeling results indicate mean slip rates on the MBT-fault ramp of ~2 – 3 mm.a^{-1} since its activation. This has lead to the growth of the >5-km-high frontal Dhauladhar Range and continuous deep-seated exhumation and erosion. The obtained results also provide interesting constraints of deformation patterns and their variation along strike. The results point towards the absence of the time-transient 'mid-crustal ramp' in the basal decollement and duplexing of the Lesser Himalayan sequence, unlike the nearby regions or even the central Nepal domain. A fraction of convergence (~10-15%) is accommodated along the deep-seated MBT-ramp, most likely merging into the MHT. This finding is crucial for a rigorous assessment of the overall level of tectonic activity in the Himalayan morphotectonic provinces as it contradicts recently-published geodetic shortening estimates. In these studies, it has been proposed that the total Himalayan shortening in the NW Himalaya is accommodated within the Sub-Himalaya whereas no tectonic activity is assigned to the MBT.

Zusammenfassung

Die sich verändernde Massenverteilung in einem Gebirge kann zu einer variierenden Sedimentablagerung führen, welche in Folge die Spannungszustände und Verwerfungsaktivitäten beeinflusst. Eine der herausforderndsten Aufgaben im Verständnis der Evolution aktiver Gebirge wie dem Himalaja, ist die Unterscheidung der verschiedenen treibenden Mechanismen wie der Variation im Sedimentfluss und der tektonischen Aktivitäten in Raum und Zeit.

Der Himalaja ist einer der bedeutendsten känozoischen Gebirgszüge, der durch die Kollision zwischen der nordwärts wandernden indischen Platte und der eurasischen Kontinentalplatte vor 55-50 Ma entstand. Die anhaltende Konvergenz der beiden tektonischen Platten wird durch Verwerfungen und Auffaltungen innerhalb des bogenförmigen Gebirges aufgenommen, aber auch durch das fortwährende laterale und vertikale Wachstum des Tibetischen Plateaus, der angegliederten Gebirgszüge und den Gebirgsregionen weiter nördlich. Das Gebirgswachstum zeigt sich durch die Entwicklung von aufeinanderfolgenden in südlicher Richtung verkippten Verwerfungssystemen. Von Norden nach Süden unterteilen die Hauptstörungen Main Central Thrust (MCT), Main Boundary Thrust (MBT) und Main Frontal Thrust (MFT) den Himalaja in verschiedene morphotektonische Bereiche. Die anwachsende Topographie interagiert mit den feuchten Monsunwinden was zu einem ausgeprägten Regen-, Verwitterung-, Erosion- und Sedimenttransportgradienten zum Vorland hin und darüber hinaus führt. In den intermontanen Tälern, der tiefgelegenen Ausläufern des Himalajas ist ein Teil dieser Sedimente eingeschlossen und vorübergehend gelagert. Das verbesserte Verständnis über die Entwicklung dieser Sedimentarchive bietet eine einmalige Möglichkeit die Auslöser der veränderlichen Sedimentproduktion, -anlieferung und -lagerung in einem sich aktiv deformierenden Gebirge über Raum und Zeit zu entschlüsseln und unterstützt dabei die Anstrengungen eine Verbindung zwischen Sedimentvolumen in intermontanen Becken und den Veränderungen des Spannungszustandes in geringfügiger Krustentiefe zu untersuchen. Die Sedimentumverteilung in Gebirgen kann, über einen Zeitraum von 10^2-10^4 Jahren, kulturelle Eigenheiten, die Infrastruktur in den intermontanen Tälern und sogar die Seismotektonik eines Gebirgsgürtels, beeinflussen. Es besteht ein verstärktes Interesse die Prozesse über die Sedimentführung und den kausalen Zusammenhang zwischen Tektonik, Klima und Topographie zu verstehen. An dieser Schnittstelle zwischen den tektonischen Prozessen und den überlagernden klimatischen und sedimentären Prozessen im Gebirgskeil setzten meine Untersuchungen an. Das Untersuchungsgebiet umfasst das intermontane Kangra-Becken im nordwestlichen Sub-Himalaja, da hier die Eigenschaften der verschiedenen morphotektonischen Gebieten des Himalajas gut ausgeprägt sind. Dieses Gebiet gehört zu einer Region, die stark durch den Monsun geprägt wird. Zahlreiche Flussterrassen bieten hervorragende Markierungen für die Beurteilung der Deformationsprozesse innerhalb des Himalajischen Gebirgskeils. Durch ihre Situation direkt vor der Dhauladhar-Kette ist die Region sowohl früher als auch heute durch ausgeprägte Erosionsgradienten und Sedimentprozessen charakterisiert, die den wiederholend wechselnden Klimabedingungen zugeordnet werden können. Angesichts dieser Bedingungen untersuchte ich in dieser tektonisch aktiven Region, klimatisch gesteuerte jungpleistozäne-holozäne Sedimentzyklen,

welche sich möglicherweise als Auslöser für die tektonische Umorganisation innerhalb himalajischen Gebirgskeils verantwortlich zeichnen und zumindest seit dem frühen Holozän zu out-of-sequence Aufschiebungen führen.

Das Kangra-Becken ist durch die MBT und den Jwalamukhi Thrust (JMT) im Sub-Himalaja nach Norden und Süden begrenzt und lagert vorübergehend aus der Dhauladhar-Kette angelieferte Sedimente. Im Becken sind ~200-m dicke Konglomerate abgelagert, welche zwei ausgeprägte Aggradationsphasen wiederspiegeln. Nachfolgend auf die Aggradationsphasen wurden mehrere Flussterrassen in die Schuttfächerablagerungen eingeschnitten. Die Datierung der Terrassenoberflächen mittels kosmogener ^{10}Beryllium Nuklide ergab für die höchste erhaltene Terrasse ein Alter von 53.4±3.2 ka (AF1). Diese Oberfläche wurde daraufhin bis ~15 ka fortwährend eingeschnitten, bis sich ein zweiter Schuttfächer (AF2) zu bilden begann. Die Aufschüttung des AF2 wurde durch episodische holozäne Einschneidungen verdrängt, wobei sich mindestens vier Terrassenebenen bildeten. Wir haben eine Korrelation zwischen dem variierenden Sedimenttransport und ∂^{18}O Aufzeichnungen aus Regionen, die vom indischen Sommermonsun (ISM) betroffen sind, gefunden. Die Aggradation fand wohl durch einen erhöhten Sedimentfluss während verstärkten Phasen des ISM und der Enteisung nach dem letzteiszeitlichen Maximum statt, wobei Perioden eines geschwächten ISM mit einem tieferen Sedimentzufluss verbunden sind und auch mit erneuten Einschneidungen zusammentreffen.

Die Evolution fluvialer Terrassen entlang von sub-himaljischen Flüssen im Kangra-Sektor wurde auch durch tektonische Prozesse erzwungen. Rückwärts gekippte und gefaltete Terrassen dokumentieren deutlich die tektonische Aktivität der JMT. Der Versatz einer der Terrassenebenen weist auf eine Verkürzungsrate von 5.6±0.8 bis 7.5±1.0 mm.a-1 über die letzten ~10 ka hin. Darüber hinaus zeigt meine Studie, dass jungpleistozäne/holozäne out-of-sequence Aufschiebungen 40-60 % der gesamten 14.2±2 mm.a-1 Verkürzung aufgeteilt über den ganzen Sub-Himalaja hinweg aufnehmen. Die Aufzeichnungen an der JMT dokumentieren niedrigere Verkürzungsraten über längere Zeiträume, was auf out-of-sequence Aktivität im Sub-Himalaja hindeutet. Die erneute Aktivierung der JMT kann mit Veränderungen im tektonischen Spannungsfeld durch großflächigen Sedimenttransport aus dem Becken in Verbindung gebracht werden. Ich spekuliere daher darauf, dass die Deformationsprozesse im Sub-Himalaja sich entsprechend der Voraussagen des Modelles der kritischen Keilform verhalten und treffe folgende Annahmen: >200 m Sedimentaggradation würde eine gegen das Vorland gerichtete Ausbreitung der Deformationsfront, eine Wiedereinschneidung und die Beseitigung der meisten gelagerten Sedimente (beinahe 80-85 % der optimalen Beckenfüllung) auslösen. Daraus folgten wiederum sub-kritische Bedingungen der kritischen Keilformtheorie und der Rückzug der Deformationsfront würde somit ausgelöst.

Während Erosionsproszesse und die damit verbundene Versteilung der Hänge über einen längeren Zeitraum der Tektonik zuzuschreiben sind, sind Sedimentzyklen in diesem Umfeld hauptsächlich das Resultat aus klimatischen Zwängen. Meine neuen Oberflächenexpositionsdaten aus kosmogenen Nukliden ^{10}Be und die Zusammenstellung bisheriger Studien jungpleistozäner bis holozäner Flussterrassen und sowie alluviale Verfüllungen zeigen periodische Fluktuationen in der Sedimentanlieferung und der Transportkapazität in einem Zeitraum von 10^3 bis 10^5 Jahren. Um den möglichen Einfluss des Klimawandels auf diese Fluktuationen zu bewerten, habe ich den in den Schuttfächern und Terrassen aufgezeichneten zeitlichen Ablauf der Aggradations- und Einschneidungsphasen mit kontinentalen Klimaarchiven wie z. B. Speläotheme (stalagmiten) aus Monsun beeinflussten Nachbarregionen verglichen. Zusammen mit bisherigen publizierten OSL Altern, welche den Zeitpunkt der Aggradation anzeigen, finde ich eine Korrelation zwischen Variationen des Sedimenttransportes durch Sauerstoff-Isotopen Aufzeichnungen aus den von ISM betroffenen Gebieten. Dementsprechend kam es im Kangra-

Becken während Zeiten der verstärkten Monsunintensität (Wechsel von trockenen, kalten und feuchten, warmen Perioden – MIS4 bis MIS3 und MIS2 bis MIS1) (MIS = marines Isotopenstadium) und der Enteisung des letzteiszeitlichen Maximums wahrscheinlich durch erhöhten Sedimentfluss zur Aggradation. Im Gegenzug stimmen schwache Perioden der Monsunintensität oder niedrigeren Sedimentlieferung mit der Wiedereinschneidung der bestehenden Becken überein.

Zum Schluss enthält meine Studie einen Teil einer Tieftemperatur-Thermochronologie Studie, welche die jüngste Exhumationsgeschichte der Dhauladhar-Kette beurteilt. Zirkon-Helium (ZHe) Alter und publizierte Tieftemperatur-Daten (ZHe, Apatit-Spaltspuren (AFT)) dieses Höhenzuges belegen zusammen mit einer 3D thermokinematischen Modellierung (PECUBE) die Einschränkungen der Exhumation und der an die Gebirgskette gebundene MBT-Aktivität mindestens seit dem mittleren Miozän. Die Resultate der Modellierung deuten auf mittlere Gleitraten auf der MBT-Überschiebungsrampe von ~2–3 mm/yr seit ihrer Aktivierung hin. Dies führte zum Wachstum der >5-km hohen Front der Dhauladhar-Kette und einer kontinuierlichen, tiefsitzenden Exhumation und Erosion. Die erzielten Ergebnisse zeigen die Einschränkungen der Deformationsmuster und ihrer Variation entlang des Streichens. Die Resultate deuten auf eine Abwesenheit einer über die zeit-veränderlichen Rampe des basalen Abscherhorizontes in der mittleren Krustentiefe und einer Duplexbildung des Niederen Himalajas hin, dies im Gegensatz zu den nahegelegenen Gebieten oder sogar zu Zentralnepal. Ein Bruchteil der Konvergenz (~10-15%) wird entlang der tiefsitzenden MBT-Rampe aufgenommen, die aller Wahrscheinlichkeit nach in die MHT übergeht. Diese Erkenntnis ist maßgeblich für eine gründliche Beurteilung der Gesamtgröße der tektonischen Aktivitäten in den morphotektonischen Provinzen des Himalajas, da sie kürzlich publizierten geodätischen Schätzungen von Verkürzungsraten widerspricht. In jenen Studien wurde vorgeschlagen, dass die gesamte Verkürzung des Gebirges im nordwestlichen Himalaja innerhalb des Sub-Himalajas aufgenommen wird, wobei der MBT keine tektonische Aktivität zugeschrieben werden wird.

Declaration of authorship

This thesis comprises three independent studies published or in review in high-impact, international peer review journals. Chapters 3 through 5 correspond to the individual studies.

Chapter 3: Climate-driven sediment aggradation and incision since the late Pleistocene in the NW Himalaya, India.

Saptarshi Dey, Rasmus C. Thiede, Taylor F. Schildgen, Hella Wittmann, Bodo Bookhagen, Dirk Scherler, Vikrant Jain, Manfred R. Strecker

Published in **Earth and Planetary Science Letters (doi:10.1016/j.epsl.2016.05.050)**

Dey, Thiede and Strecker designed the study. Dey, Thiede and Jain contributed to organizing and conducting the fieldwork and sampling. Dey prepared all the ^{10}Be TCN samples for measurement. Dey, Wittmann, Bookhagen, Schildgen and Scherler contributed to the analysis of samples and the calculation of exposure ages and paleo-erosion rates. Dey wrote the manuscript as first author, with contributions from all co-authors.

Chapter 4: Holocene internal shortening within the northwest Sub-Himalaya: Out-of-sequence faulting of the Jwalamukhi Thrust, India.

Saptarshi Dey, Rasmus C. Thiede, Taylor F. Schildgen, Hella Wittmann, Bodo Bookhagen, Dirk Scherler, Manfred R. Strecker

Revised manuscript (minor revisions) in review in **Tectonics (AGU Publications)**

Dey, Thiede and Strecker designed the study. Dey and Thiede contributed to organizing and conducting the fieldwork and sampling. Dey prepared all the ^{10}Be TCN samples for measurement. Dey, Wittmann, Bookhagen and Schildgen contributed to the analysis of ^{10}Be TCN samples and the calculation of exposure ages. Dey, Scherler and Schildgen contributed to the assessment of fault displacement. Dey performed the morphometric terrain analysis of the study area with the help from Thiede and Schildgen. Dey wrote the manuscript as first author, with contributions from all co-authors.

Chapter 5: Deep-seated exhumation along the tectonically active MBT: The Dhauladhar Range in the northwestern Himalaya, India.

Rasmus C. Thiede, Xavier Robert, Konstanze Stübner, **Saptarshi Dey**, Johannes Faruhn, Manfred R. Strecker

To be submitted to **Lithosphere (Geological Society of America Publications)**

Thiede and Strecker designed the study. Thiede, Faruhn and Dey conducted the fieldwork and sampling. Thiede, Faruhn and Robert contributed to the PECUBE thermokinematic modelling. Faruhn, Stübner and Thiede contributed to the low-temperature thermochronological dating. Dey and Faruhn contributed to the morphometric terrain analysis. Thiede, Stübner and Dey compiled the thermochronological data from the NW Himalaya. Dey and Thiede compiled the figures and the data. Thiede wrote the manuscript, with contributions from all other co-authors.

Acknowledgements

First and foremost, I would like to convey my deepest regard to Dr. Rasmus Thiede. Thank you Rasmus for guiding me through these years in Potsdam and spending time and effort for this work. It is your ideas, thoughts and encouragement that have inspired me.

I would like to thank my supervisor Prof. Dr. Manfred Strecker for continuously supporting me during my stay in Potsdam and his encouraging and inspiring words, which helped me to focus on the work. I would like to thank the DFG Graduate School GRK 1364, Research Focus Earth Sciences and Potsdam Graduate School for the financial support for this study. I am grateful to Prof. Taylor Schildgen, Prof. Bodo Bookhagen, Prof. Dirk Scherler, Dr. Daniel Melnick and Dr. Sara Savi who have immensely helped with their scientific input and comments in the submitted papers and conference contributions. A special thanks goes to Dr. Hella Wittmann who taught me the procedures of sample treatment for cosmogenic nuclide dating at GFZ Potsdam. I would like to thank the Graduate School Coordinator Dr. Henry Wichura and the departmental staffs Tanja, Martina, Enrico, Ines and Cornelia for their constant support and help. I convey my gratitude to Prof. Ed Sobel for the access to the sample preparation facility. My sincere thanks goes to Dr. Gerold Zeilinger and Dr. Wolfgang Schwanghart for teaching me a thing or two about ArcGIS and MATLAB.

I would like to thank all the GRK 1364 members for the assistance they provided to me and the wonderful time we had together in Kenya or in the Himalayas during the excursions. I am lucky to have officemates like Jürgen Mey, Patricia Eugster, Stephanie Olen, Julius Jara-Muñoz, Simon Riedl, Fabiana Castino, Veronica Torres Acosta, Goerkem Sivri, Humaad Ghani, Ghasem Heiderzadeh, Steffi Tofelde, Lars Erpel, Victoria Georgieva, Tianqui Zhang to name a few. Especially Jürgen, I will surely miss the lunchtime chats with you. A special thanks to Patricia for helping me with the German translations.

I am grateful to everyone who supported me during my fieldwork days in the Kangra valley in India. In particular, Dr. Vikrant Jain (IIT-GN) and Dr. Soumyajit Mukherjee (IITB) for helping me with the logistics, sample shipments and supporting letters. I thank Johannes Faruhn for his help during the two field seasons. I am grateful to Marcus Nennewitz for sharing the field data with me. The fieldwork was made easy by our driver-cum-local guide Chamel Singh. I would like to thank our field assistants (Prakash Chand, Jeevan Kumar, Ajit Kumar and Pratap Kumar) without whom digging all the 2.5-m-deep pits in such a 'tough terrain' would have been impossible.

I would like to thank all my friends, near and dear ones across the globe who are with me all the time. Living alone in Golm would have been hard without the company of Nirmalya Choudhury, Pawlok Dass, Dipanjan Roy, Trishikhi Roychoudhury, Shiladitya Banerjee, Nikesh Narayan, Aarthi Menon, Saswati Sarkar, Mrinal Majumdar and many more. A big cheer to the awesome school and college friends I have – Godhuli, Abhisek, Sourav, Kingshuk, Mainak, Jaydeep, Dipanjan, Utsab, Tithi, Suhrit, Ankush, Prajkta, Sonal and the list goes on and on. I thank all my well-wishers and childhood friends from the neighborhood I originally belong to. I promise to Shambhu Das and Hirak Dey that someday we will go together to visit Ladakh and enjoy the tranquility of the magnificent Himalaya.

It is time to thank my family. My Maa-Baba and my in-laws, you have always been supportive of me whatever I did, so, a fair share of my achievements if any, must be yours. My tryst with Geology would not have been possible without my elder brother's advice to go for a Bachelors' degree in this subject.

Titir, thank you for everything. If you ask me 'after all this time?', my answer will be 'always'.

Chapter 1: Introduction

1.1. Motivation

The growth of mountain belts corresponds to a balance between tectonic uplift, climatically forced erosion and denudation of the range, which produces large quantities of sediment that will be ultimately transported out of the orogen (Grujic et al., 2006; Reiners and Brandon, 2006; Thiede et al., 2005; Montgomery and Brandon, 2002; Willett, 1999; Molnar and England, 1990) the vertical component of ongoing collision of two tectonic plates (Gansser, 1964), denudation processes involve weathering and erosion of rocks and transport of eroded mass mainly aided by fluvial or glacial processes (Leopold et al., 2012; Lupker et al., 2012; Koppes and Montgomery, 2009; Von Blankenburg, 2005; Peizhen et al., 2001). Protracted tectonic uplift changes atmospheric circulation (Benn and Owen, 1998 and references therein; Raymo and Ruddiman, 1992), which results in a strong redistribution of precipitation (Bookhagen and Burbank, 2006); in monsoonal climates this may be manifested by high-magnitude and low-frequency hydrometeorological events. Furthermore, temperature variations, often combined with changes in precipitation, result in changes of the glacial equilibrium altitude, causing major glacial advances or retreats (Anderson and Mackintosh, 2006; Owen et al., 2002). As the fluvial and glacial systems are highly dependent on climatic fluctuations (Bookhagen et al., 2006a; Finkel et al., 2003; Jain and Tandon, 2003; Macklin et al., 2002; Owen et al., 2002; Benn and Owen, 1998) the overall orogenic evolution is sensitively balanced between tectonic and climatic changes, and can develop a strong feedback between each other (Allen et al., 2013). For instance, tectonic uplift enforces the growth of a new orographic barrier and causes localized enhanced precipitation leading to focused erosion and sediment delivery to fluvial networks on the windward flank of the orographic front and thus shields precipitation from more internal range and regions, resulting in sediment-filled, high-elevation basins over geologic timescales (Sobel et al, 2003). In the windward sectors, however, the mass of sediments is carried via the fluvial network out of the range, causing significant unloading (Bookhagen et al., 2005) and denudation of the mountain range (Thiede and Ehlers, 2013). The denudation is again balanced by continued rock exhumation or uplift (Thiede et al., 2004; Beaumont et al., 2001). Hence, tectonic and climatic influences impacting a mountain belt are often dynamically coupled and may determine the characteristics of the overall growth of the orogen (Whipple, 2009; Clift et al., 2008; Stolar et al., 2006; Thiede et al., 2005). Debate has been going on the individual impact of these two forcing factors on the growth of the mountain belts and if at all, their influence can be spatially and temporally constrained across a growing mountain belt.

The Himalaya constitutes the most important active collisional Cenozoic mountain belt; the range is an integral part of the Indo-Eurasian collisional zone, as a result the most extensive continent-continent collision (Nabelek et al., 2009; Searle et al., 1997; Garzanti et al., 1987; Le Fort, 1981). The Himalaya hosts the highest mountain peaks on Earth and is affected by some of the most erosive drainage networks, which efficiently feed large quantities of sediments to the Indo-Gangetic-foreland basin and the Indus and Bengal submarine fan systems in the adjacent marine basins (Metivier et al., 1999; Einsele et al., 1996). A study by Lupker et al., (2012) estimated ~610±230 $\mathrm{Mt.a^{-1}}$ sediment flux from the Himalayan orogen.

However, both the foreland basin and submarine fan have been challenging locations to study, particularly with respect to spatial and temporal variations in erosion over time scales of 10^3-10^4 years. Large-scale changes in sea-level, sediment recycling, variable source-to-sink transport times and sediment input from the Indian peninsular sources pose a challenge for a proper evaluation of the sediment flux history using marine archives (Clift et al., 2001). In addition, inhomogeneous distribution of sediments, erosion and redistribution of sediments from transient storage, the lack of well-exposed sections (with the exception of few boreholes and trenches) (Gibling et al., 2005; Sinha et al., 2005), and above all, extensive anthropogenic activity make the study of foreland sediment archives a daunting task. However, within the mountain belt there are intermontane sedimentary basins that allow for a closer, direct inspection of exposed sedimentary fills in the context of tectonic and climatic forcing factors. These fills constitute alluvial-fan deposits that are ubiquitous along the mountain fronts. These terrestrial sediment archives are excellent locations to study the dynamics of the late Quaternary fill and re-incision history, sediment-fill architecture, provenance and the causal mechanisms behind cycles of sediment storage and excavation and renewed transport. But the preservation potential of these archives, is generally low due to rapid erosion and extensive anthropogenic land-use, leading to the disturbance of geomorphic surfaces.

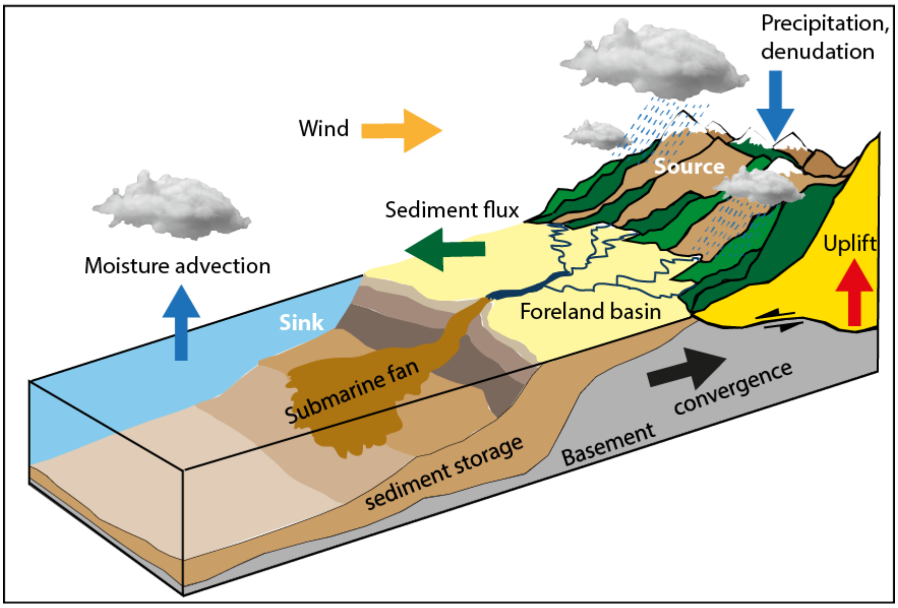

Figure 1.1*: The evolution of a mountain belt is influenced by dynamic coupling of tectonic and climatic forcing. Rock uplift results from the convergence of tectonic plates and the uplifted topography acts as an orographic barrier, which focuses precipitation on one flank of the mountain belt. Focused precipitation leads to efficient denudation and transport of sediments to the foreland or marine basins (modified after C. France-Lanord).*

Approximately 20 mm.a^{-1} of a total of 40 to 50 mm.a^{-1} convergence between the Indian and Eurasian plates is accommodated within the Himalaya (Avouac and Tapponnier, 1993; Lyon-Caen and Molnar, 1985), where orogen-perpendicular convergence rates vary from 13.3±1.7 mm.a^{-1} in the west to 21.2±2.0 mm.a^{-1} in the east (Stevens and Avouac, 2015; Ader et al., 2012); the remainder is accommodated farther north in the Tibetan Plateau and the broken foreland, including the Tien Shan and Qilian Shan. The vertical and lateral growth of the Himalaya has been accommodated by several major south-verging thrust systems. From north to south these include the Main Central Thrust (MCT), the Main Boundary Thrust (MBT), and the Main Frontal Thrust (MFT) (DeCelles et al., 2001; Gansser, 1964). All of these north-dipping structures sole into a basal décollement, the Main Himalayan Thrust (MHT) (Nabelek et al., 2009; Ni and Barazangi, 1984). These thrust systems also bound the regional morphotectonic sectors of the orogen: the Higher Himalaya in the hanging wall of the MCT, the Lesser Himalaya between the MCT and the MBT, and the Sub-Himalaya between the MBT and the southernmost MFT (Gansser, 1964).

Present-day geodetic measurements, as well as balanced and retro-deformed cross sections across many transects of the Himalayan orogen suggest that the majority of Himalayan shortening is now accommodated within the Sub-Himalaya (Hirschmiller et al., 2014). Lave and Avouac (2000) proposed that the MFT, as a principal Sub-Himalayan thrust, accommodates ~20±1 mm.a^{-1} shortening in the Central Nepal sector during the Holocene. This Holocene shortening rate agrees well with modelling results of the GPS-data compilations that amount to 20±3 mm.a^{-1} (Stevens and Avouac, 2015; Bettinelli et al., 2006). However, the shortening history within the northwestern Himalaya differs significantly from the Central Himalaya. Continued convergence of the Indo-Eurasian plate has propelled foreland-ward migration of the deformation front and has created several sub-parallel fold-and-thrust belt, thus forming the over 100-km-wide Sub-Himalaya of the northwestern Himalaya (Powers et al., 1998). Seismic reflection profiles and balanced cross-sections suggest that all of these Sub-Himalayan thrusts are rooted in the MHT décollement (Mukhopadhyay and Mishra, 1999; Powers et al., 1998; Raiverman, 1994). Importantly, the convergence accommodated within the Sub-Himalaya is partitioned among these structures and is not only concentrated on the MFT (Thakur et al., 2014; Powers et al., 2009). Shortening across the Sub-Himalayan thrusts has resulted in the formation of intermontane piggy-back basins, which transiently store the foreland-bound sediments.

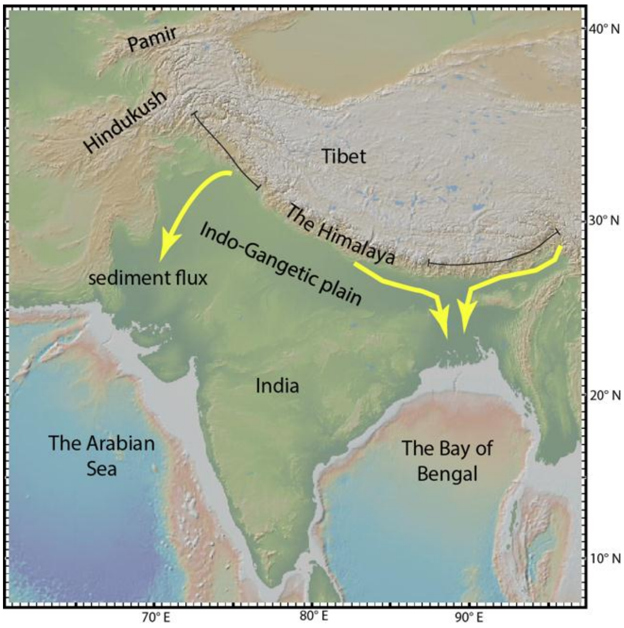

Figure 1.2: *Overview of the Himalayan orogeny and adjacent regions formed at the southern margin of the Tibetan plateau due to the Indo-Eurasian collision. Sediments eroded from the orogen are transported to the foreland basin and are ultimately funneled to the Arabian Sea or the Bay of Bengal.*

While the Sub-Himalayan tectonic processes create the accommodation space for sediment storage, the ultimate fate of sediment production, transport and transient storage in the Himalayan orogenic wedge prior the continued transport to the sink, superposed climate climate cycles may play a decisive role.

Previous studies have suggested that both tectonics and climate play an important synergistic role in sediment transport, storage and basin connectivity, but most likely these processes operate on very different timescales. Accordingly, the tectonic effects on sediment flux are generally recognized over Myr timescales, whereas climate-induced changes in sediment flux are rather short-lived (1-10 kyr) and more frequent. More specifically, ongoing continental plate collision, associated crustal shortening, and uplift within the orogen provide a long-term mechanism for sustained erosional sediment flux through time (Clift et al., 2008; DeCelles et al., 2001), but superposed climate change or the effects of climatic variability may strongly modulate this process system on much shorter timescales (e.g., Dutta et al., 2012; Bookhagen et al., 2006; Pratt-Sitaula et al, 2004). Indeed, periodic climate change can lead to short-term and potentially far reaching variations in erosion and sediment delivery to intermontane basins and the foreland (Olen et al., 2015; Bookhagen et al., 2005). In the Himalaya, 1-10 kyr variations in the strength of the Indian Summer Monsoon (ISM) and 50-100 kyr glacial- interglacial cycles, have been shown to fundamentally influence river discharge and sediment flux (Scherler et al., 2015; Wulf et al., 2010; Bookhagen et al., 2005; Gibling et al., 2005; Goodbred and Kuehl, 2003; Owen et al., 2002; Singh et al., 2001). However, complicated stratigraphic relationships, a poor preservation potential, and difficulties in obtaining unambiguous age constraints have been persistent challenges when attempting to link climate change with landscape and sedimentary-flux response (Densmore et al., 2015; Scherler et al., 2015). Sediments eroded from the high sectors of the mountains are transported by rivers into the intermontane valleys or foreland sectors, where the slope and consequently stream power are reduced; as a result, the excess sediment load is deposited in form of alluvial fans (Gupta, 1997). Along the strike of the Himalaya such alluvial fans are currently formed or older segments are preserved virtually everywhere. Locally, such as in the Kangra Basin of the northwest Himalaya, these transiently-stored valley fills are ~200-m-thick vestiges of former conglomeratic fills. Incision of these deposits by the drainage network has created several levels of fluvial terraces at successively lower elevations above the main-stem river.

Fluvial terraces are regarded as one of the most widely-used geomorphic markers that help assess climate and tectonic forcing of landscape evolution. Terraces not only provide information about paleo-drainage network conditions (Bull, 2008), but they can also be efficiently used as strain markers (e.g., Thakur et al., 2014; Lave and Avouac, 2000). Terraces in general can be classified as aggradational (fill) or degradational (strath) in origin. In case of fill terraces, if it were possible to temporally constrain the formation of the terraces and / or associated alluvial-fan tops, we would be able to unravel the chronology of the evolution of the corresponding drainage network. At the same time, a well dated and correlated terrace sequence may furnish the opportunity to test the synchronicity of sediment cycles (aggradation and fluvial re-incision) with respect to climatic fluctuations that may be correlatable with existing paleoclimate data (i.e. oxygen-isotope data from speleothems). On the other hand, rock uplift along existing structures at depth or at surface can be deduced from dated strath and abandoned fill-terrace surfaces. Hence, obtaining temporal constraints on such terrace levels is necessary to perform a rigorous analysis of tectonic and climatic forcing of landscapes and provides an excellent opportunity to evaluate deformation styles, rates and histories.

Apart from the tectonic and climatic impact on the sediment cycle and sedimentary loading stresses and their possible feedback mechanisms triggering or subduing tectonic activity and thus impacting the tectonic reorganization of fold-and-thrust belts, there is another less-understood problem regarding the long-time averaged shortening or exhumation rate on the MBT hanging wall. Along strike of the Himalayan orogen, the hanging wall of the MBT creates a sharp topographic contrast with the low-lying Sub-Himalaya and forms the first orographic barrier. Available low-temperature thermochronological data show exceptionally young mineral cooling ages and suggest ongoing deep-seated exhumation on the MBT hanging wall (Deeken et al., 2011). Although recent studies have proposed that total Himalayan shortening is now being accommodated solely by the Sub-Himalaya, field observations and thermochronological studies by Deeken et al., (2011) and Thiede et al., (2009) suggest that in some segments in the NW Himalaya the MBT must have been continuously active. Hence, more detailed field observations and additional age control are essential to understand the activity of MBT on Myr timescales and to explain the lateral variation in growth of the Himalayan range front.

1.2. Active deformation in the Himalaya in light of the critical taper model

Previous studies of orogenic processes have used the critical wedge taper model (Dahlen, 1988; Davis et al., 1983) to explain the deformation processes of wedge-shaped mountain belts. This model has also been applied to the Himalayan frontal fold-and-thrust belt (Singh et al., 2012). The applicability of the critical taper model for the entire Himalaya is controversially debated and is certainly an oversimplification. Nonetheless, the model provides reliable predictions for the first-order structural framework to explain the tectonic evolution and particularly the spatiotemporal characteristics of brittle deformation of the orogenic front of the Himalaya, as this region satisfies the mechanical criteria for the evolution of a critical Coulomb wedge (Hirschmiller et al., 2014; Singh et al., 2012; Mukul et al., 2010; Hilley and Strecker, 2004; Mugnier et al., 2004). In analogue and numerical models of critically tapered wedges, changes in sedimentary load have been shown to influence the location of faulting (Davis et al., 1983). Accordingly, sediment aggradation within intermontane valleys or near the front of a wedge can potentially increase taper and thus induce foreland-ward propagation of deformation to maintain critical taper (Hilley and Strecker, 2004; Willett and Beaumont, 1994; Dahlen, 1988). Conversely, removal of stored sediments in intermontane basins lower the frontal taper, rendering it sub-critical, and hence causing the retreat of the deformation front and out-of-sequence thrusting, until the wedge re-establishes its critical taper (Dahlen, 1990). The applicability of these concepts to real-world examples and field validation has often been hampered by limited outcrop conditions and poor geochronological constraints.

The critical wedge taper model is often used to describe tectonic reorganization in orogens and accretionary prisms in the marine realm (Fig. 1.3). In these models, the geometry of a propagating wedge taper (θ) is defined by the sum of the topographic slope (α) and the dip of a basal décollement (β). Only at a certain θ, described as the critical taper (θ_c), the wedge propagates foreland-ward. If, $\theta > \theta c$, then the taper is supercritical and the wedge readjusts by forward propagation of the deformation front (lowering of β). On the other hand, if $\theta < \theta c$, the taper is subcritical and the wedge readjusts by retreat of the deformation front to the interior of the wedge (increase of β). For a wedge under critical taper conditions, increase in the accretionary flux or addition of material to the wedge from outside the accretionary prism, disturbs steady-state conditions by increasing α and hence, as a consequence, β reduces. Once, the erosional flux from the prism outbalances the accretionary flux (large-scale removal of material from the wedge), the taper will be subcritical and prompts the deformation front to retreat.

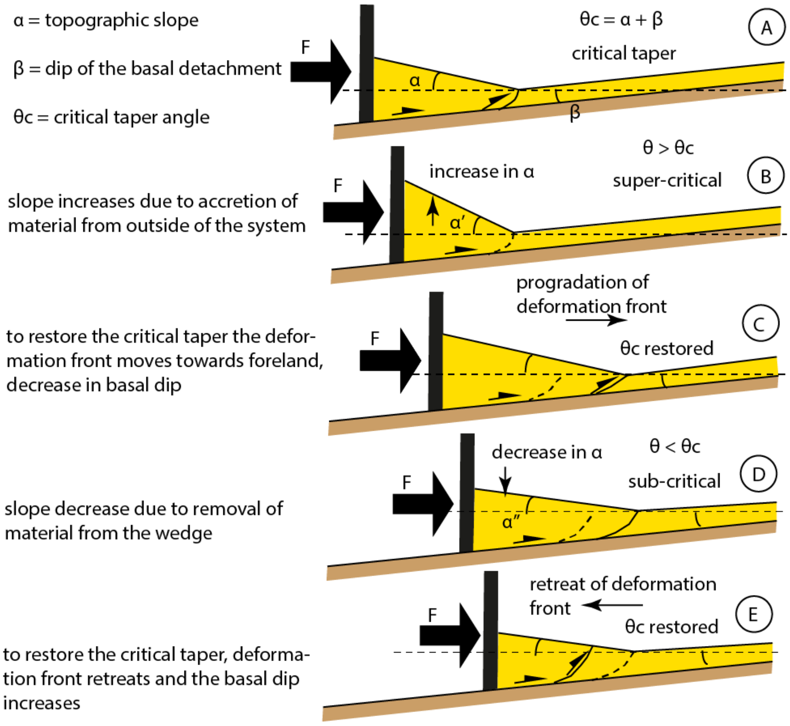

Figure 1.3: Critical taper model explaining the link between sediment routing, sediment storage and tectonic reorganization in an active orogen (after Dahlen, 1990; Davis et al., 1983).

1.3. Why the Kangra re-entrant is an ideal location for a tectono-climatic study of intermontane foreland fold-and-thrust basins?

The Kangra region of the northwest Himalaya constitutes the largest re-entrant and width of the Sub-Himalayan wedge, which exposes an 80 to 100-km-wide fold-and-thrust belt at the southernmost parts of the orogenic flank. Several sub-parallel thrust systems, including the the MFT or southernmost deformation front, show evidence of ongoing shortening in this region (Thakur et al., 2014; Malik et al., 2008; Powers et al., 1998). Tectonic uplift along the Sub-Himalayan structures creates accommodation space for the foreland-bound sediments sourced from the Lesser and Higher Himalayas. These intermontane piggy-back basins (locally termed as ‘duns) have frequently stored late Pleistocene-Holocene sediments delivered from the higher compartments of the Himalayan orogen (Srivastava et al., 2009; Sah and Srivastava, 1992). In the northwest corner of the re-entrant, on the hanging wall of the NW-SE striking Jwalamukhi Thrust (JMT), the Kangra Basin is one such piggy-back basins in the fold belt; it has an area of ~700 km^2. A limited number of previous studies (e.g., Thakur et al., 2014; Srivastava et al., 2009; Powers et al., 1998; Sah and Srivastava, 1992) have shown that the Kangra Basin and the adjacent Palampur Fan store sediments derived from the southern flank of the Dhauladhar Range. Satellite imagery and digital elevation models from the reveal well-preserved alluvial fans and several extensive fluvial terrace remnants. Srivastava et al., (2009) reported that sediment aggradation in the basin started prior to ~78±17 ka and was subsequently punctuated by fluvial re-incision phases. Therefore, the Kangra Basin is an excellent location to study the mechanisms of sedimentary cycles over the last 100 ka. In addition, the source area of the stored sediments are very localized and encompass the southern flank of the Dhauladhar Range; hence, the signal-to-noise ratio for any prospective tectonic or climatic impact is rather high.

Moreover, the distance between the source and the temporary sink is low (<80 km), thus lag times of any tectono-climatic impact and its feedback signals in the sediment archive are minimal.

The Kangra Basin is located on the hanging wall of the active Jwalamukhi Thrust (Thakur et al., 2014; Powers et al., 1998) and previously it has been proposed that the post-depositional tectonic activity on this fault has occurred at a rate of 3.5– 4.2 mm.a^{-1} over the last 30 ka. But the deformation rate was obtained using the dated straths, and hence, can be further refined and re-evaluated using more precise age determination of the timing of abandonment of the fluvial terraces. The Kangra Basin hosts tectonically offset terraces with disturbed paleo-longitudinal river profiles that are ideal to test these relationships. Apart from these two independent research opportunities to decipher the dynamics of an orogenic wedge in light of climatic and tectonic forcing, the Kangra Basin provides us with the possibility to investigate and deconvolve any link between these two issues.

1.4. Research questions

Decade-long debates have been going on concerning the tectono-climatic coupling and its effects on the evolution of the Himalayan mountain front, the sediment-delivery system of the range, and related seismotectonic scenarios (now cite some key references). Against the background of these questions and our lacuna in understanding coupled tectonic and climate-driven processes in a field scenario I have identified several key research questions, which have guided and motivated me to conduct the work presented in this thesis:

(a) Can sediment cycles near the Himalayan mountain front be correlated with fluctuations in climatic forcing or are they solely dependent upon sediment load? How well can fluvial terraces and remnant alluvial fans be temporally constrained? How compare paleo-erosion rates to present-day basinwide erosion rates?

(b) How does tectonic activity control the evolution of the intermontane basins, such as the Kangra Basin? How can dated fluvial terraces be employed to help determine fault activity of a principal fault in the Sub-Himalaya (i.e., the Jwalamukhi Thrust)? Does Holocene shortening on the Jwalamukhi Thrust imply out-of-sequence thrusting? Does enhanced renewed activity on the Jwalamukhi Thrust result from large-scale sediment removal from the Kangra Basin ?

(c) Is the MBT active in the Kangra re-entrant ? What is the probable shortening rate (averaged over several million years) accommodated by the MBT?

To answer these fundamental questions of orogenic evolution in the Sub-Himalaya, I had to first obtain age control for the alluvial fill and the terraces in the Kangra Basin as well as the exhumed rocks in the MBT hanging wall. The terrace surfaces were thus dated with terrestrial cosmogenic nuclide-based surface exposure dating (^{10}Be), whereas, the the history of the MBT hanging-wall bedrock was assessed using low-temperature thermochronology (Zircon-Helium and Apatite Fission Track dating). In addition, I carried out extensive field mapping and performed morphometric terrain analyses using GIS tools. The low-temperature thermochronology of the MBT hanging-wall rocks and PECUBE modelling of the Dhauladhar Range are a part of the work by Rasmus C. Thiede and Johannes Faruhn of Potsdam University. I assisted during fieldwork, morphometric terrain analysis and manuscript writing. All sample preparation including target packing for cosmogenic nuclide dating, exposure-age and erosion-rate calculations, and all morphometric analyses were solely my contribution.

1.5. Surface-exposure dating using *in-situ* terrestrial cosmogenic nuclides

The production of cosmogenic nuclides affords one of the most reliable and ubiquitously applicable dating method on Earth's surface, which has been widely used to date various geological phenomena ranging from glacier fluctuations, lava flows, meteorite impacts, fault scarps, geomorphic surfaces, and landslides (see Dunai, 2010 for a review). Cosmogenic nuclides are produced due to interactions of high-energy cosmic rays with nucleons (Dunai, 2010; Lal, 1991). High-energy protons and alpha particles originated from the galaxy infiltrate Earth's atmosphere and interact with atoms to produce secondary cosmic particles. Among these secondary particles, neutrons and muons are capable to break down atoms at the Earth's surface once they reach it, thus producing *in-situ* /terrestrial cosmogenic nuclides (TCN) (Masarik and Beer, 1999). The typical reactions for this process are – 1) primary spallation reactions; 2) thermal neutron capture; 3) negative muon capture; and 4) fast muon reaction (Dunai, 2010). Some of the resulting isotopes of these reactions are stable (^{3}He, ^{21}Ne) while some are radioactive and thus unstable (^{10}Be, ^{26}Al, ^{14}C, ^{36}Cl). Among these cosmogenic nuclides, Beryllium-10 (^{10}Be) is one of the most used isotopes for different types of dating methods and erosion-rate determinations. ^{10}Be is formed due to bombardment of neutrons onto the stable oxygen isotope (^{16}O) and has a half-life (λ) of 1.39 Ma (Chmeleff et al., 2010; Korschinek et al., 2010).

$$^{16}\mathrm{O} + {}^{1}\mathrm{n} = {}^{10}\mathrm{Be} + {}^{3}\mathrm{He} + \alpha \quad (1)$$

Production of TCNs vary with depth and the type of reactions taking place. While spallation is dominant in the upper few meters of the Earth's surface, at greater depths, muonic interactions play the most important role (Granger and Riebe, 2007). As my main goal is to use TCNs for surface-exposure dating of geomorphic surfaces, I will henceforth discuss only spallation in this context. In general, production rates of TCNs decrease exponentially with depth below the surface.

$$Pz = P0e^{-\frac{z\rho}{\Lambda}} \quad (2)$$

where Pz (atoms.g^{-1}.a^{-1}) is the production rate at depth z (cm), $P0$ (atoms.g^{-1}.a^{-1}) is the surface production rate, ρ is the density of the material (g.cm^{-3}), and Λ is the attenuation length (160±5 g.cm^{-2} for neutron spallation) (Dunne et al., 1999). The surface-production rates vary with atmospheric pressure, geographic location, altitude above mean sea level and time (Lal, 1991). For comparison and scaling of the production-rate estimates, the production rates are normalized to sea-level, high-latitude (SLHL) production rates (Borchers et al., 2016).

The total TCN concentration measured in the laboratory is the cumulative TCN concentration accumulated during rock exhumation, transport and post-depositional time (Anderson et al., 1996). Therefore, dating any deposit with TCNs requires knowledge of cosmogenic inheritance (concentration accumulated prior to deposition at the sample point, with the assumption that the deposition happened in a very short time span). For aggradational surfaces, TCN depth profiles have been used as a novel approach to estimate cosmogenic inheritance, the variation of TCN concentration with depth, and an assessment of erosional or anthropogenic impact on the dated surface (Repka et al., 1997).

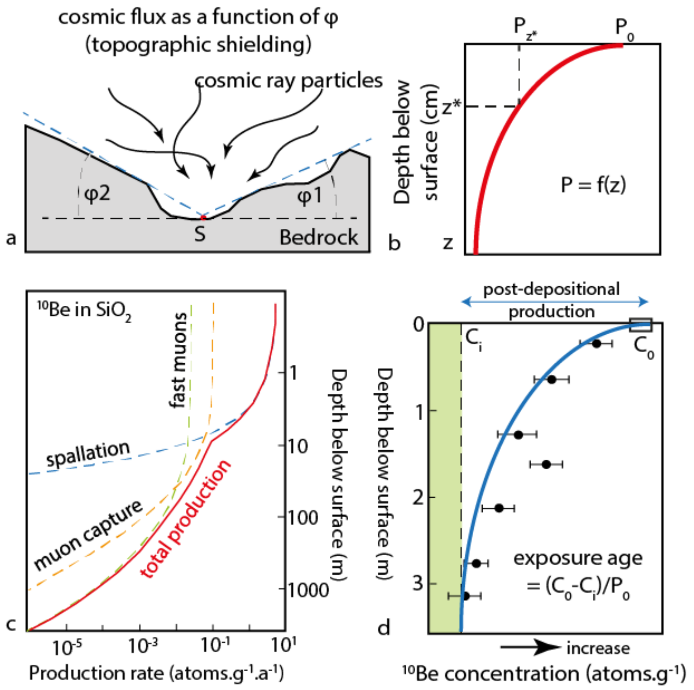

***Figure 1.4**: Fundamental characteristics of in-situ cosmogenic nuclides. (a) Cosmic ray flux at any point S is inversely proportional to topographic shielding (φ). (b) Production of TCN decreases exponentially with depth; (c) different types of reactions producing ^{10}Be within quartz at different depth (Granger and Riebe, 2007); (d) ^{10}Be depth-profile model accounting for cosmogenic inheritance and probable exposure age.*

The CRN concentration decreases exponentially with depth according to the following relationship-

$$Cz = Pz.t + Ci + Cie^{-\lambda t} \quad (3)$$

where *Cz* (atoms. g^{-1}) is the measured concentration at any depth *z* after an exposure time *t* and *Ci* is the nuclide inheritance (atoms. g^{-1}). If the time t is negligible compared to the half-life, then radioactive decay ($Cie^{-\lambda t}$) can be ignored. Therefore, from the depth profiles, the exposure age of the aggradational surface can be deduced with the following equation-

$$\text{Exposure age of the surface, } t = \frac{C0-Ci}{P0} \quad (4)$$

Another important factor concerning TCN exposure-age calculation is the surface-production rate scaling scheme and the sea-level, high-latitude (SLHL) reference production rate. I have used 4.01 atoms.g^{-1}.a^{-1} as a reference SLHL production rate for ^{10}Be (Borchers et al., 2016) for age calculation and a time-dependent spallogenic production model after Lal (1991) and Stone (2000). Depth-profile simulations after Hidy et al. (2010) were done using the time-independent spallogenic production model after Lal (1991) and Stone (2000). Monte-Carlo simulations with the depth-profile samples allow one to obtain the mean exposure age with up to 2σ uncertainty (Hidy et al., 2010). Model surface concentrations (using the best fit line) and inheritance (with uncertainty) can be obtained from each depth profile. The difference between the model surface concentration and inheritance provides the post-depositional ^{10}Be accumulation, which can be used in the freely available age-calculator programs, such as the CRONUScalc program (http://web1.ittc.ku.edu:8888/2.0/) (Marrero et al., 2016). This allows transformation of the time-independent (St) ages to time-dependent or (Lm) ages (after Balco et al., 2008). Using higher SLHL production rates, such as 4.5 or more (after Balco et al., 2008), would result in a younging of the exposure ages by 15 to 20%. Sample preparation methods and calculation of AMS (Acceleration Mass Spectrometer)-derived sample concentrations are described in Chapter 3 and Chapter 4 of this thesis.

Chapter 2: The Himalaya

2.1. Tectonic and geologic overview

Major crustal faults mark the different morphotectonic domains of the Himalayan orogen, viz. a) Indus-Tsangpo Suture Zone (ITSZ); b) Tethyan Himalaya (TH); c) Higher Himalaya (HH) or the Himalayan crystalline core; d) Lesser Himalaya (LH); and e) Sub-Himalaya (SH). Among these domains, the northernmost ITSZ forms the geological boundary between rocks related to the Indian plate to the south and the Eurasian plate to the north. This boundary contains ophiolites and associated rocks of the Neo-Tethys Ocean. The Tethyan Himalaya is situated between the Southern Tibetan Fault System and the Great Counter Thrust. The Tethyan Himalaya consists of late Precambrian to lower Paleozoic sedimentary and metasedimentary rocks (Steck et al., 1993; Burchfiel et al., 1992; Gansser, 1964) and a thick Permian to Eocene continental-margin sequences (e.g., Steck, 2003 and ref. therein; Brookfield, 1993). These sediments were affected by very low-grade metamorphic conditions as a consequence of thin-skinned tectonics forming the Tethyan fold-and-thrust belt and the Eo-Himalayan stages of shortening (e.g., Wiesmayr and Grasemann, 2002; Ratschbacher et al., 1994). The age of deformation generally decreases from north to south, from the late Eocene to the early Oligocene. However, these two domains are not as significant for this study compared to the Higher to Sub-Himalayan domains.

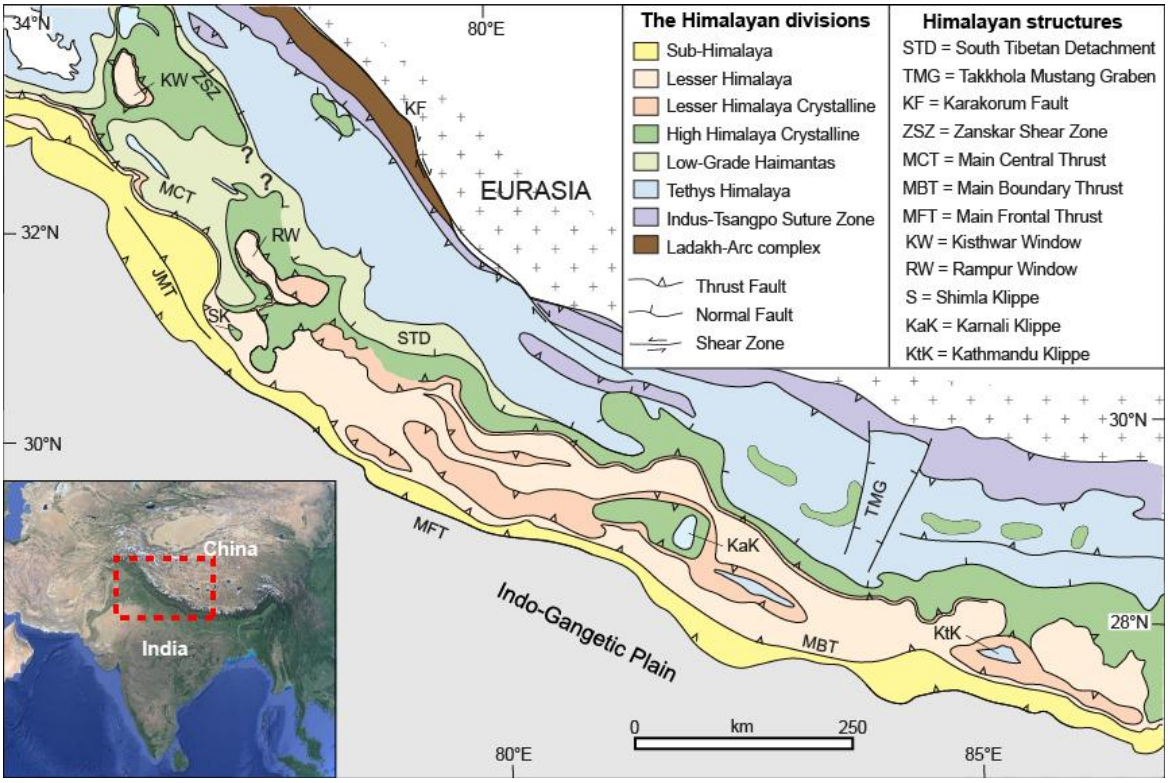

Figure 2.1*: Overview of the morphotectonic structures of the northwestern and central Himalayan orogen. Major faults from the north to the south: STDS (Southern Tibetan Detachment), the MCT (Main Central Thrust), the MBT (Main Boundary Thrust) and the MFT (Main Frontal Thrust) with geologic divisions, such as the Indus-Tsangpo Suture zone, Tethyan Himalaya, Higher Himalaya, Lesser Himalaya and Sub-Himalaya are shown (modified after DiPietro and Pogue, 2004).*

The hanging wall of the MCT hosts moderate to high-grade metasediments, meta-igneous rocks and igneous intrusives; these rock units are commonly referred to as the Himalayan crystalline core series (HHCS) (Srivastava and Mitra, 1984; Valdiya, 1980). The HHCS contains north-dipping amphibolite-migmatitic ortho- and paragneisses (Thiede et al., 2004; Carosi et al., 1999). In most of the Himalayan sections, the MCT transitions into a shallow-dipping thrust towards the foreland, which separates the HHCS with low- to medium-grade metamorphics of the Lesser Himalaya. The HHCS gneisses are considered to be metamorphic equivalents of the Upper Proterozoic to Cambrian sediments of the Tethyan Himalaya. The HHCS units are intruded by Cambro-Ordovician granitic plutons. The Lesser Himalayan sequence is bounded by the MCT on top and the MBT at its base. The Lesser Himalayan Complex (LHC) consists of Precambrian clastic sediments and low- to medium-grade (amphibolite) metamorphic rocks. The MBT separates the LHC from the Himalayan foreland-basin sediments in its footwall. In most of the outcrops, the MBT is defined as a steeply north-dipping, cataclasized deformation zone. Based on indirect evidence related to an abrupt change in the sedimentary sequence within the Sub-Himalaya, Meigs et al., (1995) have suggested, that the onset of MBT activity might have been as early as 11-9 Ma and continued up to 5 Ma or thereafter.

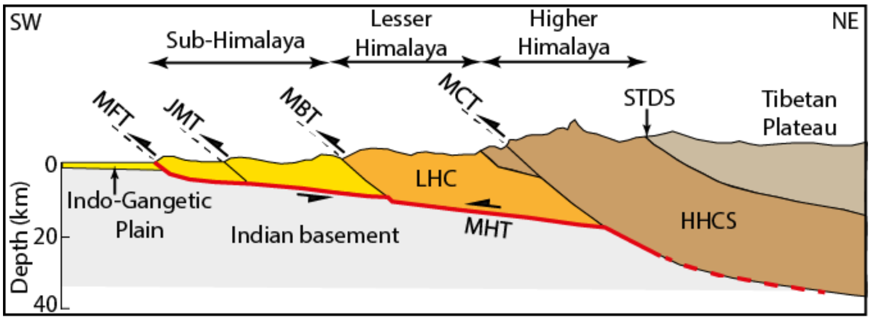

Figure 2.2*: Generalized cross section of the NW Himalaya, showing major thrust systems and morphotectonic domains (modified after Vannay and Grasemann, 2001; Dezes, 1999).*

In the footwall of the MBT lies the Sub-Himalayan fold-and-thrust belt, which has incorporated the foreland-basin sediments into the Himalayan orogenic wedge. Several sub-parallel thrusts branching out from the MHT accommodate ongoing shortening within the Sub-Himalaya (Thakur et al., 2014). The MFT is the southernmost thrust of this domain and defines the margin of the orogenic wedge. The Sub-Himalaya hosts both the Cretaceous-Paleocene flysch deposits of the Singtali Formation and the Subathu Group and the subsequently deposited molasse sediments. At the base of the molasse sequence is the Eocene to Lower Miocene Dharamsala Group (greenish grey siltstone, sandstone, claystone), followed by the sedimentary Siwalik Group of rocks. The Middle Miocene Lower Siwalik sediments consist of siltstone and claystone, the Upper Miocene Middle Siwalik strata consist of sandstone with minor claystone and occasional pebble horizons, whereas the Pliocene Upper Siwaliks host boulder conglomerates with occasional intercalated sand lenses. As mentioned above, ongoing crustal shortening within the Sub-

Himalayan domain has created several intermontane piggy-back basins. These basins trap a fraction of the foreland-bound sediments derived from the higher sector of the orogen. These unconsolidated alluvial fills and partly glacio-fluvial deposits near the mountain front are referred to as the Neogal Formation of the NW Himalaya (Thakur, 1992; Karunakaran and Ranga Rao, 1976). In the footwall of the MFT the undeformed foreland-basin sediments are partly exposed, forming the Indo-Gangetic Plains.

2.2. Climate in the Himalaya

Understanding the changes in climate over time is important as they result from first-order changes in atmospheric circulation patterns, moisture transport toward the continent, which ultimately affects precipitation and surface processes. Upon impinging on a topographic barrier focused orographic precipitation leads to runoff and triggers hillslope processes and sediment transport out of the orogen. In case of the Indian sub-continent, the Indian summer monsoon circulation is the most eminent climatic phenomenon which corresponds to nearly 70-80% of the total annual precipitation in just four months (June-September) (Wulf et al., 2010). The winter westerlies cause the rest of the precipitation in the Himalayan orogen, causing rainfall or snow and nourishing glaciers. Next to sustained tectonic deformation removal of mass from the mountain front and the orogen interiors has long been debated as a major trigger of orogenic growth (Thiede et al., 2005); hence the manifestations of climatic impact on the evolution of the Himalayan orogen are of major interest.

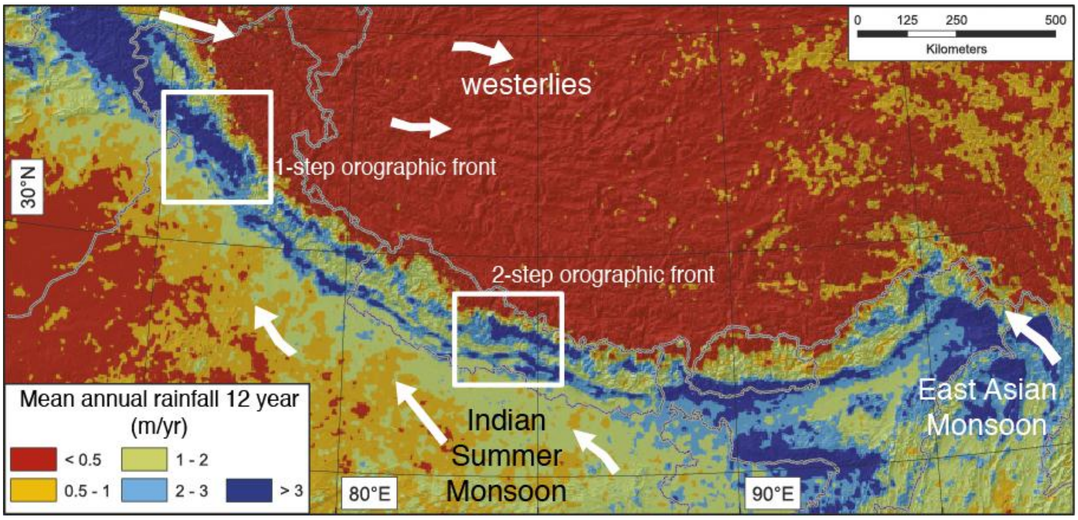

Figure 2.3: 12-year average TRMM rainfall distribution data (Bookhagen and Burbank, 2006, 2010), showing rainfall distribution across the Himalaya. Depending on the character of the orographic front(s), there are one or two high-precipitation belts within the orogeny. Due to the orographic effect rainfall in Tibet is very low.

The Himalayan mountain range fundamentally affects continent-wide atmospheric circulation. First, it has mechanical effects on atmospheric circulation trajectories, particularly in winter when it splits the surface westerly winds into northern and southern branches and prevents the southward flow of cold continental air towards the Indian Subcontinent (Benn and Owen, 1998). Second, heating of the Tibetan Plateau, continental Asia and the Indian Subcontinent in summer raises air temperatures above the zonal mean for the free atmosphere at the same height, thus enhancing the pressure gradient that attracts moisture-bearing air masses from the Bay of Bengal, which ultimately drives the Indian Summer Monsoon and westward moisture transport along the mountain front.

More specifically, the Indian Summer Monsoon provides large amounts of water to the existing drainage systems of the Himalaya that drive erosion and sediment removal from the orogen. Climate in the Himalaya is mainly dominated by the southwest Indian Summer Monsoon (ISM). Each year, during the months of June-September, the ISM delivers 80% of the total annual rainfall, which exceeds >4m in some locations along the mountain front (Bookhagen and Burbank, 2010) (Fig. 2.3). During early summer, heating in the interior of the Indian subcontinent and the Tibetan plateau creates a low-pressure zone, which drags the moist air from the Arabian Sea and the Bay of Bengal northwestward. The uplifted Himalayan arc acts as an orographic barrier to the monsoonal winds and causes maximum precipitation on the stoss side. However, the pattern of the rainfall distribution is variable along-strike – (a) precipitation-gradient from E to NW (e.g., Bookhagen and Burbank 2006). Furthermore (b) specific topographic characteristics result in a highly variable precipitation pattern. In the northwest Himalaya and Bhutan, the orographic barrier constitutes a single step on the MBT-MCT zone, whereas in Central Himalayan sector (~1000 km) there exists a two-step orographic barrier; one at the mountain front near the MBT, and the other one in the orogen interior, corresponding with the physiographic transition (PT) zone in the Central Nepal sector (Wobus et al., 2005; Olen et al., 2015).

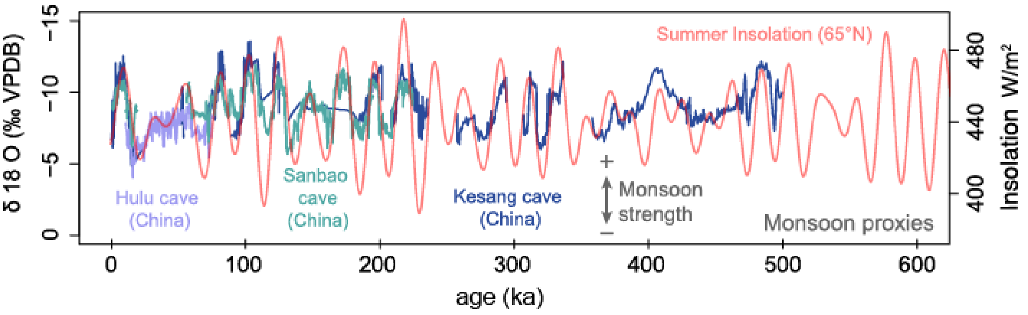

Figure 2.4: *Climate proxies showing fluctuations in monsoonal strength over time (in kyr). Oxygen-isotope ratio from cave stalagmites (Wang et al., 2001, 2008; Cheng et al., 2012). Combined with northern hemisphere summer-insolation data (e.g., Berger and Loutre, 1991) these proxies show overall co-varying trends in climatic variability (modified after Blöthe et al., 2014).*

Fluctuations in atmospheric circulation patterns in the Himalayan realm on different timescales are related to global climate oscillations and cause far-reaching changes in monsoonal strength. The intensity of the ISM and summer insolation (Berger and Loutre, 1991) co-vary over time (Figure 2.4). Accordingly, phases of weaker summer insolation are characterized by colder, dry periods dominated by the westerlies and correspond to periods of strong glaciation (Scherler et al., 2011; Owen et al., 2008, 2002). Consequently, during such phases the ISM-intensity is weak. Conversely, with stronger insolation, the hot and humid conditions of the ISM are strengthened. Glacial-interglacial cycles manifested by corresponding deposits in the terrestrial realm typically average over ~100 kyr and can be further divided into stadial and interstadial conditions as reported from Marine Isotope Stages (MIS) (Lisiecki and Raymo, 2005). With respect to the Himalaya the marine isotope stages correspond to alternating wet and dry phases. Continental cave-speleothem records (i.e., Dutt et al., 2015; Cheng et al., 2012; Wang et al., 2008; Fleitmann et al., 2003; Wang et al., 2001) and marine sediment-core records (Ali et al., 2014; Marzin et al., 2013) mirror the fluctuations in strength of ISM or Asian Summer Monsoon. In light of these recurring changes in moisture availability and consequently changes in erosion and stream power makes the Himalayan intermontane basins a premier location to test possible climate-driven forcing in sediment flux at regional scales.

Previous studies over the last decades have reported several Pleistocene-Holocene valley fills from different domains of the Himalaya. Some of the noted studies by Scherler et al., (2015), Dutta et al., (2012), Srivastava et al., (2008, 2009), Bookhagen et al., (2006), Pratt-Sitaula et al., (2004) and Sinha et al., (2010) have proposed that climatic fluctuations trigger sediment aggradation or incision in Himalayan valleys. However, the lack of temporal constraints and dateable material has put a hold on the overall understanding and opportunities to furnish unambiguous evidence for a mechanistic linkage between the sediment cycle and climatic forcing. The Kangra re-entrant within the Sub-Himalaya, however, provides a fortuitous setting as ~200-m-thick valley fills are still preserved together with easily recognizable fluvial terraces that were subsequently carved into these deposits. The lithology of the terrace-building material (quartzites and granites) is well suited for ^{10}Be-based surface-exposure dating, which allows comparing exposure ages from the terrace surfaces with existing climate proxy data.

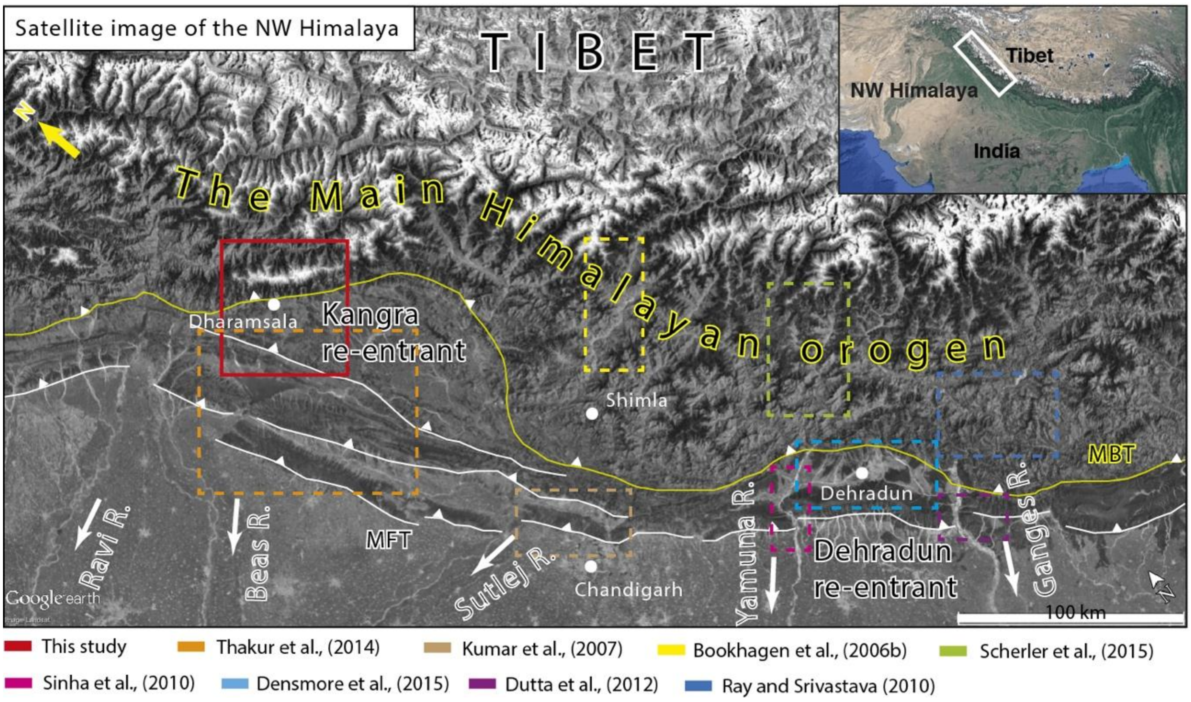

Figure 2.5*: An overview Landsat image of the Northwestern Himalaya (inset: The Himalayan arc between India in the south and Tibetan Plateau in the north) showing major drainage systems that carry sediment out of the orogen. Notably, the Kangra re-entrant exposes the maximum extent of Sub-Himalayan fold-and-thrust belt which facilitates transient storage of foreland-bound sediments. The multi-colored rectangles indicate locations of some important studies on transient sediment archives, which have been previously-published.*

The study area is situated ~700-1000 m above sea level and on the stoss side of the northwest Himalayan orographic front, the Dhauladhar Range, and is part of a region with pronounced topographic, rainfall and surface-process gradients. The precipitation in the basin and the source area is mainly governed by the Indian Summer Monsoon which cause ~70-80% of the annual precipitation in this area. The rest of the annual precipitation is part of the winter westerlies, resulting in snowfall in the Dhauladhar Range and sparse rainfall in the basin. However, the southern flank of the range is devoid of any significant glacier at the present day, and no major glacial advances have been reported in the region during the Pleistocene. Hence, fluctuations in the strength of the Indian Summer Monsoon and thus rainfall variability are considered to be the key climatic parameters that repeatedly impacted the surface-process regime in this part of the Himalaya.

Chapter 3: Climate-driven sediment aggradation and incision since late Pleistocene in the NW Himalaya, India

Key points

- Late Pleistocene and Holocene sediment cycles are driven by climatic change and sediment flux.
- Predominantly Higher Himalayan erosion in late Pleistocene to early Holocene times.
- Fluvial incision coincides with lower or decreasing intensity of the Indian Summer Monsoon.

Abstract

Deciphering the response of sediment routing systems to climatic forcing is fundamental for understanding the impacts of climate change on landscape evolution. In the Kangra Basin (northwest Sub-Himalaya, India), upper Pleistocene to Holocene alluvial fills and fluvial terraces record periodic fluctuations of sediment supply and transport capacity on timescales of 10^3 to 10^5 years. To evaluate the potential influence of climate change on these fluctuations, we compare the timing of aggradation and incision phases recorded within remnant alluvial fans and terraces with climate archives.

New surface-exposure dating of six terrace levels with *in-situ* cosmogenic nuclide ^{10}Be indicates the onset of incision phases. Two terrace surfaces from the highest level (T1) sculpted into the oldest preserved alluvial fan (AF1) date back to 53.4±3.2 ka and 43.0±2.7 ka (1σ). T2 surfaces sculpted into the remnants of AF1 have exposure ages of 18.6±1.2 ka and 15.3±0.9 ka, while terraces sculpted into the upper Pleistocene-Holocene fan (AF2) provide ages of 9.3±0.4 ka (T3), 7.1±0.4 ka (T4), 5.2±0.4 ka (T5) and 3.6±0.2 ka (T6). Together with previously published OSL ages yielding the timing of aggradation, we find a correlation between variations in sediment transport with oxygen-isotope records from regions affected by the Indian Summer Monsoon. During periods of increased monsoon intensity and post-Last Glacial Maximum glacial retreat, aggradation occurred in the Kangra Basin, likely due to high sediment flux, whereas periods of weakened monsoon intensity or lower sediment supply coincide with incision.

3.1. Introduction

Climate and tectonics play an important role in the evolution of the Himalaya (Bookhagen et al., 2006; Hirschmiller et al., 2014; Kumar et al., 2007; Thiede et al., 2004). Ongoing collision between continental plates, crustal shortening, and uplift within the orogen provide a long-term source of erosional sediment flux through time (Clift et al., 2008; DeCelles et al., 2001). Nonetheless, periodic climate changes can lead to short-term and potentially important variations in erosion and sediment transport (Bookhagen et al., 2005; Olen et al., 2015; Pratt-Sitaula et al., 2004). In the Himalaya, climatic changes on different timescales, such as 1-10 kyr variations in strength of the Indian Summer Monsoon (ISM) and 50-100 kyr glacial- interglacial cycles, have been shown to influence river discharge and sediment flux (Bookhagen et al., 2005; Dutta et al., 2012; Gibling et al., 2005; Owen et al., 2002; Scherler et al., 2015; Singh et al., 2001; Sinha et al., 2010). However, complicated stratigraphic relationships and difficulties in obtaining unambiguous age constraints have been persistent challenges when attempting to link climate change with landscape response (Densmore et al., 2015; Scherler et al., 2015).

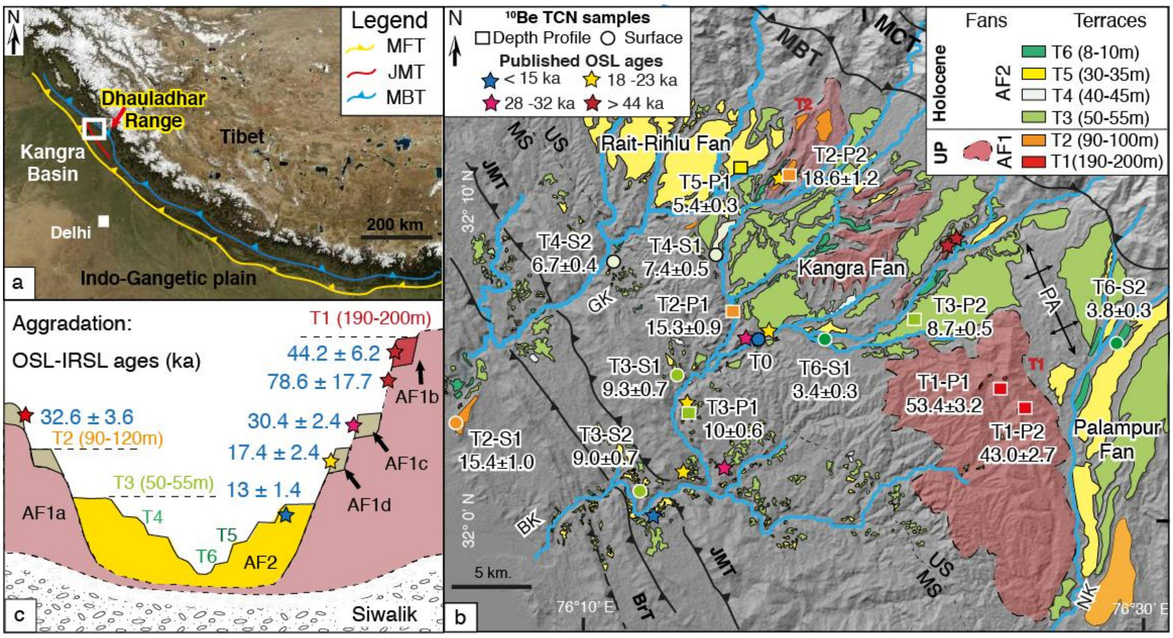

Figure 3.1: (a) Overview satellite image of the Himalayan orogen with two first order fault systems, the Main Boundary (MBT) and Main Frontal Thrust System (MFT), bounding the Sub-Himalaya. Our study area, the Kangra Basin (white rectangle shows the extent of b) is located at the foothills of the Dhauladhar Range in the NW Himalaya within the Kangra re-entrant and is bordered by the Jwalamukhi Thrust (JMT) to the south. (b) Shaded-relief map of the study area showing six levels of fluvial terraces (T1-T6) and remnant alluvial fills (AF1 -AF2) on the hanging wall of the JMT. The sample locations for in-situ ^{10}Be analysis (square - depth profile, circle - surface-only) are labeled with their surface exposure ages and 1σ uncertainty (in ka). Locations of optically stimulated luminescence (OSL) samples (Srivastava et al., 2009; Thakur et al., 2014) *are shown with stars. (c) Schematic section of Kangra Basin alluvial fill showing two major episodes of aggradation (AF1 and AF2, derived from OSL ages from previous studies) succeeded by fluvial incision causing abandonment of six terrace levels. The AF1 aggradation phase can be subdivided into four minor aggradation events, namely AF1a, AF1b, AF1c and AF1d according to their depositional age. Abbreviations: AF-Alluvial fill, MBT- Main Boundary Thrust, MFT- Main Frontal Thrust, US- Upper Siwalik, MS- Middle Siwalik, BrT- Barsar Thrust, PA- Paror Anticline, TCN- terrestrial cosmogenic radionuclide, BK- Baner Khad, GK- Gaj Khad, NK- Neogal Khad, UP- Upper Pleistocene.*

Speleothem oxygen-isotope records from India and China (Dutt et al., 2015; Fleitmann et al., 2003; Wang et al., 2001) record climate fluctuations on 10^3 year and shorter timescales related to changes in the Indian Summer Monsoon (ISM) intensity that are superimposed on 10^4 year trends associated with glacial-interglacial cycles. In this context weak monsoon periods are associated with reduced rainfall in the higher sectors of the Himalaya, whereas strong monsoon periods correlate with an increase in rainfall (Bookhagen et al., 2005; Wang et al., 2008). These variations have strongly impacted aggradation-incision cycles in large river networks such as the Sutlej Valley of the NW Himalaya, where early Holocene aggradation during an intensified ISM was followed by incision during low-intensity phases (Bookhagen et al., 2005; 2006).

To evaluate how climate variation and the balance between discharge and sediment flux affect sediment cycles of the Himalaya over late Pleistocene to Holocene timescales, we studied fluvial terraces preserved along three tributaries of the Beas River within the Kangra intermontane Basin in the NW Sub-Himalaya, Himachal Pradesh, India. We recognize two major sedimentary cycles since 80 ka: one possibly spanning the last glacial period and the second one mostly during the Holocene. Incision of the tributaries into upper Pleistocene-lower Holocene alluvium and underlying Tertiary sedimentary units was marked by different terrace levels, which we dated using concentrations of the cosmogenic nuclide ^{10}Be. We also measured the clast composition of the sedimentary fills and calculated paleo-erosion rates from different sedimentary units to test for changes in sediment sourcing and erosional efficiency through time.

3.2. Geologic setting

The Cenozoic Himalayan orogeny results from the collision between the Indian and the Eurasian plates (Gansser, 1964; Yin and Harrison, 2000). Crustal shortening associated with the southward migration of the Himalayan deformation front has led to the formation of several major south-verging thrust systems, including the Main Central Thrust (MCT), the Main Boundary Thrust (MBT) and the Main Frontal Thrust (MFT). These structures divide the Himalayan orogen into different morphotectonic domains including the Higher Himalaya (on the hanging wall of the MCT), the Lesser Himalaya (between the MCT and MBT), and the Sub-Himalaya (between the MBT and MFT).

The Kangra re-entrant is located in the NW Himalayan foothills of Himachal Pradesh (Fig. 3.1a; supplementary Fig. S 3.1). The Sub-Himalayan Kangra Basin (750-1000 m asl) lies in the northwest corner of the re-entrant and is bounded to the north by the MBT. Its hanging wall contains the Dhauladhar Range, with peaks exposing the High Himalayan crystalline rocks and granites, exceeding elevations of 5500 m. The Kangra Basin is bounded to the south by the Jwalamukhi Thrust (JMT), which forms a ramp with out-of-sequence activity (Fig.3.1b) (Thakur et al.. 2014; Powers et al., 1998; Srivastava et al., 2009). The deformed Tertiary sediments of the Kangra Basin mainly belong to the Dharamsala and the Neogene Siwalik Groups.

During the Quaternary, the Kangra Basin has witnessed several phases of sediment aggradation in the form of alluvial fans (Sah and Srivastava, 1991; Srivastava et al., 2009). IRSL ages from Srivastava et al., (2009) suggest loess deposition between 78-44 ka, which is overlain by fluvial deposits. Thakur et al., (2014) dated the alluvium above the Siwalik strath surfaces in the Kangra re-entrant, and their OSL ages suggest three aggradation periods at 32-28 ka, 23-18 ka and 14-10 ka. The incised fan deposits predominantly consist of clast-supported stream-flow and debris-flow sediments with occasional intercalations of fluvially reworked landslide deposits. The clasts mainly comprise granites and quartzites, with minor amounts of schist and partly reworked Siwalik sediments. Morphologically, the fans in the Kangra Basin can be subdivided into three segments - the western Rait-Rihlu fan and Kangra fan are separated by the Chambi-Gaj Fault (CGF); the Kangra fan and the eastern Palampur fan are separated by the Paror anticline (Fig. 3.1b). The catchments of these fans are all located along the southern flank of the Dhauladhar range and have source areas of <100 km^2. Rivers in the Kangra region have incised the thick alluvial-fan sediments and the Siwalik units, creating a series of well-defined terraces (Fig. 3.1b, 3.1c).

Our study region can be sub-divided into two principal parts. In the northern part, the Kangra alluvial fan forms the fill of the Kangra Basin, which consists mainly of a thick section of fluvial-alluvial sediments intercalated with debris-flow deposits (Dey et al., 2016- see chapter 4; Srivastava et al., 2009; Thakur et al., 2014). The southern part comprises tilted, uplifted, and eroded Siwalik sediments topped by strath terraces that in turn are covered by a thin layer of upper Pleistocene alluvium in the hanging wall of the Jwalamukhi Thrust (JMT).

Presently, the Kangra Basin is drained by two major tributaries of the Beas River, these are the Baner Khad and Gaj Khad (Khad = river). There are very few small glaciated valleys in the crest regions of the southern flank of the Dhauladhar Range at present, but Srivastava et al. (2009) proposed that during glacial times, valley glaciers were extensive and reached areas close to the MBT. The present-day climate of the study area is humid-temperate, with pronounced monsoonal rainfall from July to September (Bookhagen and Burbank, 2010). The area is densely vegetated, with subtropical forests on the hillslopes, and the terraces have been intensely cultivated, probably for several hundred years.

3.3. Methods

3.3.1. Terrace mapping

We delineated fluvial terraces within the Baner Khad and Gaj Khad watersheds both in the field and with the help of DEM-based GIS techniques and satellite imagery from Google Earth^{TM} (Fig. 3.1b). We calculated a slope map from the DEM (Cartosat 1, 30-m resolution digital elevation data, available at http://bhuvan.nrsc.gov.in/data/download/index.php) and identified pixels with slope values of 0 to 3 degrees as terraces. We determined each terrace's height above the nearby stream from combined longitudinal stream and terrace profiles extracted from the DEM using TopoToolbox (Schwanghart and Scherler, 2014). In the field, we validated our digitally-based map and verified locations, extents, and elevations of mapped terraces using hand-held GPS measurements that were plotted against geo-referenced DEM data.

3.3.2. in-situ Cosmogenic nuclide (^{10}Be)-based dating

We determined surface-exposure ages of the preserved terraces using concentrations of the *in-situ* cosmogenic radionuclide Beryllium-10 (^{10}Be) from amalgamated pebble samples collected from depth profiles and terrace surfaces. Terrace surfaces are generally covered by a sparse vegetation cover and most of them are cultivated and may thus be slightly affected by soil erosion. For depth profiles, we excavated a 2.2 to 2.5-m-deep pit for every location and collected samples at roughly 30-cm-depth intervals, including the surface sample, which represents the top 5-10 cm of the profile. We sampled >20-30 granite and quartzite pebbles (2 to 3 cm diameter) per horizon. For the surface-only samples, we sampled clasts of similar size from the entire surface (apart from the edges) and from up to 10 cm depth. Our sample locations and results are listed in Table 3.1. Results from the depth profile T2-P1 and the terrace surfaces T3 to T6 were previously reported by Dey et al., 2016 (in revision) (see Chapter 4).

Samples were processed at the University of Potsdam, GFZ Potsdam, and the University of California Santa Barbara. Samples were crushed and ground to 250 – 500 µm size, then magnetically separated and etched with HCl and multiple iterations of 1% HF before further chemical processing. After a final leach in aqua regia, each sample was dissolved in concentrated HF. Subsequently, 150 µg of ^{9}Be carrier was added to each sample. The sample matrix was removed by column chemistry. Ultimately, pure

$Be(OH)_2$ precipitate was obtained and oxidized to BeO. 100µg of Nb powder was admixed to each sample. The targets were pressed and packed for accelerator mass-spectrometer (AMS) measurements at Lawrence Livermore National laboratory (relative to 07KNSTD3110 as standard) and the University of Cologne (KN01-6-2 and KN01-5-3 as standards) (Dewald et al., 2013). An average process blank $^{10}Be/^{9}Be$ blank ratio of $2.2*10^{-16}$ (Cologne AMS) and $2*10^{-16}$ (Lawrence Livermore AMS) was subtracted from the measured sample ratios.

All exposure ages and erosion rates reported in this study are based on the time-dependent production rate scaling scheme by Lal (1991) as updated by Stone (2000), provided in the CRONUScalc web calculator (http://web1.ittc.ku.edu:8888/2.0/), and using the SLHL calibration dataset after Borchers et al., 2016. Topographic shielding of production rates is based on Dunne et al. (1999) and was calculated using either field measurements with a geological compass and the CRONUS-Earth online calculator (for exposure ages), or the DEM (for erosion rates). To determine surface-exposure ages corrected for nuclide inheritance and surface erosion from the depth profiles, we performed Monte Carlo simulations (1,000,000 iterations) using the simulator provided in Hidy et al. (2010). The simulation was run assuming a reference SLHL total ^{10}Be production rate of 4.01 $atoms.g^{-1}.a^{-1}$ (Borchers et al., 2016), density of 1.9–2.1 $g.cm^{-3}$, an attenuation length of 160 ± 5 $g.cm^{-2}$ for neutron spallation (Dunne et al., 1999), an erosion rate of 0 to 0.2 $cm.ka^{-1}$, and a total erosion threshold of 0 to 20 cm. Using a higher erosion threshold results in older ages, but we saw minimal direct evidence of erosion on the very flat terraces; also, the tight clustering of our ages from individual terraces argues for minimal erosion, and ultimately, our exposure ages should be younger than published OSL and IRSL ages reported from the underlying alluvium. Exposure ages from the depth profiles were first obtained with the Monte Carlo simulator based on the time-independent surface production scaling scheme by Lal (1991) and Stone (2000). These resulting ages were then recalculated for time-dependent production rates using the CRONUS-Earth calculator version 2.2 (Table 3.1).

For locations in which we only collected surface samples, we assume that the surface samples represent a mixture of 0-10 cm depth beneath the surface due to bioturbation and anthropogenic overprint of the terrace surface; hence, we applied a shielding factor equivalent to 5 cm depth on the surface production rate to calculate the ages. For the surface-only samples, the ^{10}Be concentration accumulated since exposure was determined by subtracting the ^{10}Be inheritance derived from depth profiles of the same terrace level from the measured concentration of the sample. In the case of T1 and T2, where we have two depth-profiles for each level, we assumed that the lower inheritance value is the actual inheritance for that terrace level. For terrace level T3, we used the average of the two inheritances from pits with terrace id T3-P1 and T3-P2. For T4, the inheritance of T3 was used, and for T6, the inheritance from T5 (from terrace id T5-P1) was used.

Exposure-age results in Table 3.1 denote the mean model-derived age of the specific sample with 2σ error (calculated using standard error propagation). The weighted mean age of a specific terrace level has been calculated from the individual sample ages using the following equation:

$$\text{Weighted mean age} = \sum_{i=1}^{n} x_i / n \pm \sqrt{\frac{\sum \sigma_i^2}{n^2}} \qquad (1)$$

where x_i is the mean age of an individual sample, n is the number of samples for a given terrace level, and σ_i is the error on the individual sample age.

3.3.3. Calculation of erosion rates

We determined catchment-average paleo-erosion rates at the time of sediment deposition from the exposure ages and inheritance values that we obtained from the depth-profile simulations and compared them the with modern day basinwide erosion rate obtained from one river sand sample (T0) (see Table 3.1). We acknowledge that our depth-profile ages indicate the onset of terrace incision, but as we have no other means to date the deposition, we assume the time between deposition and incision is relatively short compared to changes in erosion rates. Catchment-average production rates at the time of deposition were calculated based on upstream source areas. Paleo-erosion rates were calculated using the numerical functions of the CRONUS-Earth online calculator version 2.2 (Balco et al., 2008), as explained in Scherler et al (2014). Non-uniform distribution of quartz throughout the catchment may add uncertainty to our final estimates, but we suspect that the effect is relatively small compared to other uncertainties in the method.

3.4. Results

3.4.1. Sediment aggradation: Alluvial fan (AF) sequences

The Pleistocene-Holocene sedimentary fill of the Kangra Basin represents at least two different stages of two alluvial-fan fills, which we name AF1 and AF2 in stratigraphic order (Fig. 3.1c) (see Supplementary Fig. S3.3 for field photographs). The coarser fraction of the fills constitutes well-rounded, poorly-sorted, clast-supported, polished pebbles and boulders of fluvial and alluvial origin, with occasional layers of sub-angular, matrix-supported and unsorted boulders that record the input of debris flows. In addition, there are isolated outcrops of highly angular, crushed granite clasts that are underlain by heavily cataclasized fragments, which we interpret as landslide deposits.

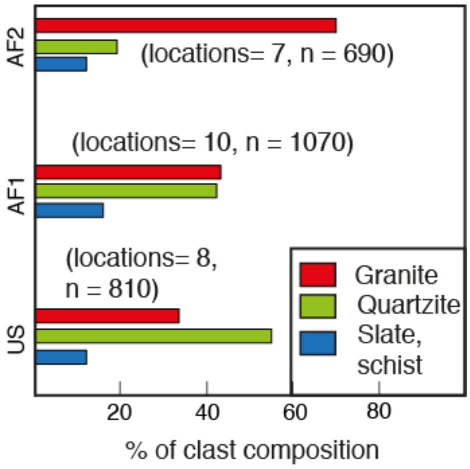

Figure 3.2: Clast counts (n= total number of clasts) from various sedimentary units throughout the basin showing changes in the clast compositions among the Upper Siwaliks (US), AF1 and AF2.

The oldest alluvial fan (AF1) is preserved south of the Paror Anticline (Fig. 3.1b) and it overlies the tilted Upper Siwalik units in the south. Based on field observations, we mapped the toe of this fan as extending down nearly to the exposed contact of the Upper Siwalik and Middle Siwalik units, north of the elevated hills in the hanging wall of the Jwalamukhi Thrust. The AF1 deposit is thicker than 200 m, but only a few surface remnants are preserved (1 to 2-km^2 surfaces at 1100-1150 m asl), which marks the minimum elevation of the AF1 fan surface (Fig 3.1b). A few more alluvial-fan remnants form small hillocks in the center of the Kangra Basin, east of the Chambi-Gaj Fault and south of the town of Dharamsala. The top surfaces of these fills lie 110 to 120 m above the riverbed. Although the core of these fills might represent the AF1deposits, OSL and IRSL ages (Srivastava et al., 2009; Thakur et al., 2014) suggest two more minor phases of aggradation post-dating the older AF1 deposition. Nonetheless, these younger deposits are lithologically indistinguishable from the older AF1 material (Fig. 3.2 and 3.4). Therefore, we assume that during later aggradation phases, the alluvium was sourced both from the Dhauladhar Range and from AF1 sediments. The younger fan deposit, AF2, is less weathered and better preserved, with the top surface at 50-60 m above the modern riverbed throughout the basin.

Clast counts reveal a systematic change in the composition of the AF1 deposits compared to the AF2 deposits (Fig. 3.2). The AF1 conglomerates are rich in quartzite (~45%), granite (~45%), and schist (~10%), whereas AF2 alluvium is rich in granitic clasts (~70%) with a minor fraction of quartzites (~20%), schists, and reworked Siwalik rocks (~10%). The matrix content in AF1 is higher and lighter in color than that in AF2, and the AF1 units have many more weathered granite clasts compared to AF2. The clast counts from older AF1 units and the two minor units that cap AF1 remnants do not show substantial variations in clast composition, and we did not find any field evidence to clearly distinguish them as different fan bodies. Hence, we consider the various units comprising the AF1 morphological remnants to represent the deposits of different sub-phases during AF1 aggradation.

Table 3.1: Surface exposure ages from different terrace levels

Terrace id	Latitude (°)	Longitude (°)	Elevation (m)	Inheritance-corrected surface ^{10}Be conc. (10^3 atoms.g^{-1}) $_a$	Mean Surface exposure age with external uncertainty (Lm age) (ka) $_{b,\,c}$	Paleo-erosion rate (mm.a^{-1})
T1-P1	32.06805	76.39855	1125	453.00±15.21	53.9±3.2	0.16±0.01
T1-P2	32.05917	76.42637	1120	356.52±16.75	43.0±2.7	0.74±0.1
T2-P1	32.10649	76.26223	750	96.26±6.52	15.6±1.2	0.7±0.1
T2-P2	32.18404	76.29688	1015	143.60±6.40	18.7±1.3	1.4±0.1
T2-S1	32.05736	76.09731	535	76.22±3.85	16.9±1.3	
T3-P1	32.05772	76.2265	625	56.61±4.51	10.1±0.9	5.1±0.9
T3-P2	32.098254	76.343855	750	55.63±5.22	9.0±0.9	4.9±0.7
T3-S1	32.077326	76.228838	650	52.76±3.43	9.2±0.7	
T3-S2	32.012256	76.212955	530	43.86±2.68	8.8±0.7	
T4-S1	32.1171	76.2603	715	37.57±1.91	6.3±0.4	
T4-S2	32.1349	76.1897	632	40.12±1.97	7.0±0.4	
T5-P1	32.182947	76.276197	785	35.90±3.03	5.7±0.5	3.3±0.4
T6-S1	32.092425	76.332009	690	15.04±1.43	2.8±0.3	
T6-S2	32.0878	76.49418	1082	25.13±1.57	3.3±0.2	
T0 (sand)	32.09134	76.25471	603			1.4±0.1

Tx-Px - depth-profile sample, Tx-Sx- 'surface-only' sample

a. Inheritance-corrected sample concentrations from Table 3.1

b,c . Surface-exposure ages calculated using Cronus-web calculator (Marrero et al., 2016) and SLHL reference production rate from Borchers et al., (2016), using (time-dependent Lal and Stone production model- Lm ages).

Table 3.1*: Surface exposure ages using in-situ ^{10}Be from different terrace levels in the Kangra Basin and paleo-erosion rates obtained from modelled cosmogenic inheritance from the TCN depth profiles. Exposure age from*

the depth profiles are time-independent and have been recalculated to time-dependent Lm age scaling (1) using the extrapolated concentrations (inheritance-corrected) at surface from the best-fit line in each profile (see Table 3.2 for detail description of the sample concentrations and calculation).

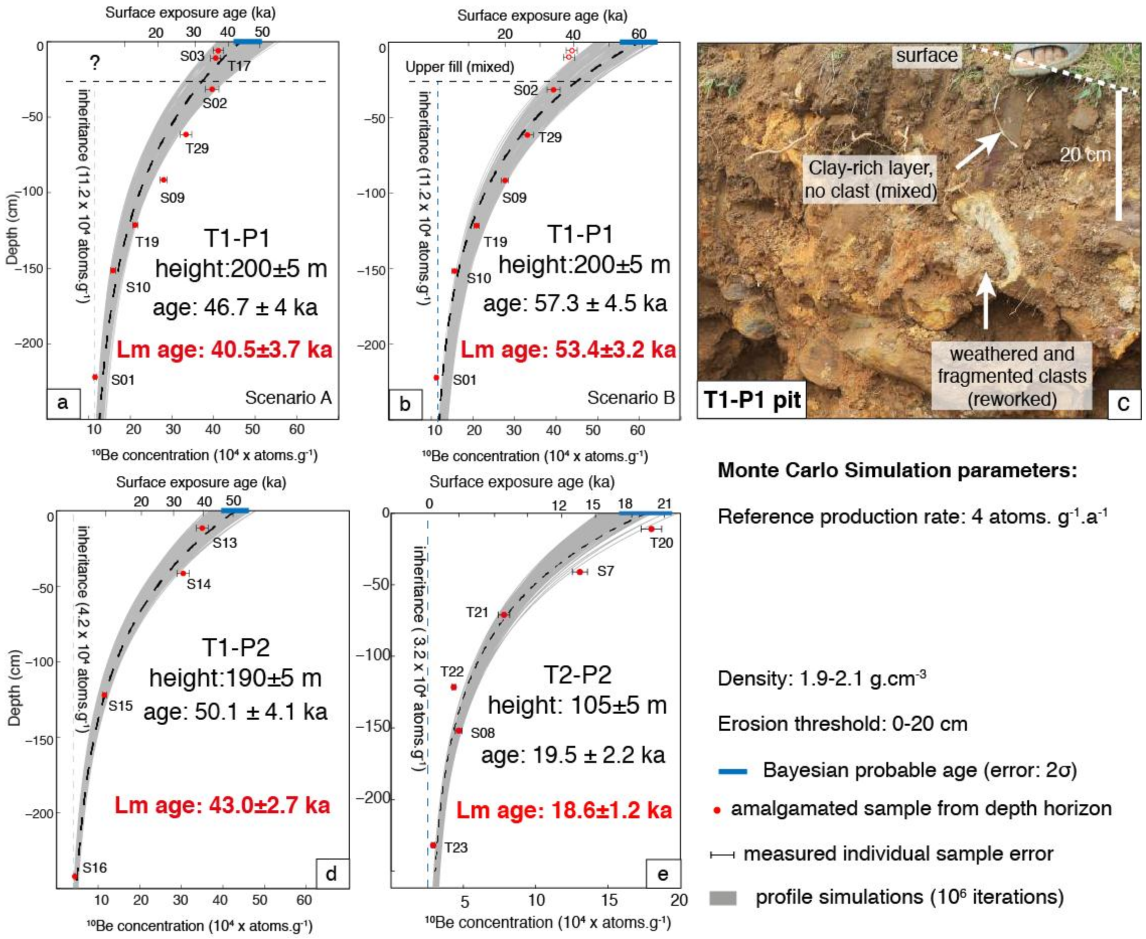

Figure 3.3*: Simulations of TCN depth-profiles from T1 and T2 terrace levels after Hidy et al., (2010) and using a time-independent Lal (1991) and Stone (2000) production model. Exposure ages (time-dependent "Lm" age) were re-calculated using the Borchers et al., (2016) calibration dataset in the CRONUScalc online calculator (Marrero et al., 2016); these ages are used in further discussion (see Table 3.1 for details). (a) and (b) show the exposure age results from the same pit, but they have been treated differently. (a) Scenario A, which including all sample data from the pit, provides an exposure ("Lm'') age of 40.5±3.7 ka. This scenario assumes that all the samples from the pit belong to the same fill, but the individual sample plots show significant scatter from the best-fit line (black dashed line). (b) Scenario B, which was run only with the samples below 30 cm depth (neglecting the top two near-surface samples), yields an exposure age of 53.4±3.2 ka for pit T1-P1. (c) Field photograph of the pit T1-P1 showing a ~30 cm thick mixed soil layer on top of the crushed and weathered conglomeratic fill horizons, indicating mixing of the upper layer, and suggesting that scenario B may better represent the actual exposure age of the surface. (d) Pit T1-P2 yields an age of 43.0±2.7 ka. (e) depth-profile simulation for level T2 (pit T2-P2), yielding an age of 18.6±1.2 ka.*

Table 3.2: Details of sample ^{10}Be concentrations with depth and surface production rate

Terrace id	Sample names	depth or depth interval (cm)	^{10}Be (atoms.g^{-1})	^{10}Be uncertainty (atoms.g^{-1})	Surface Production rate (atoms.g^{-1}.a^{-1})	Topo-graphic shielding	Inheritance from depth profiles (10^{3}atoms.g^{-1}) [b]	Modelled surface conc. (10^{3} atoms.g^{-1}) [c]	Inheritance-corrected surface conc. (10^{3} atoms.g^{-1}) [d]
T1-P1	S03	5	411133	15211	8.14	0.98	104.10±5.20	557.10±16.05	453.00±15.21
	T17	10	405000	13100					
	S2	30	396643	13446					
	T29	60	334000	10800					
	S9	90	279897	10188					
	T19	120	212000	7070					
	S10	150	158340	5368					
	S1	220	115407	5159					
T1-P2	S13	5	350166	14532	8.11	0.99	38.04±3.50	402.56±15.51	356.52±16.75
	S14	30	304377	10166					
	S15	120	115155	4572					
	S16	240	43714	1937					
T2-P1	T36$_a$	0-5	112494	3118	6.16	0.99	8.50±0.50	104.76±6.50	96.26±6.52
	T03	10	92184	3070					
	T35$_a$	30	68778	2011					
	S21	60	44591	2256					
	T30$_a$	90	29742	990					
	T02	120	23518	1050					
	T01	200-205	21064	1490					
	T32$_a$	250	32396	818					
T2-P2	T20	0	180000	6270	7.25	0.99	28.70±0.40	172.28±6.30	143.60±6.40
	S7	30	130555	5718					
	T21	60	78100	2780					
	T22	120	43300	1710					
	S8	150	46819	2500					
	T23	230	29100	1090					
T2-S1	T07	0-10	82725	3776	5.87	0.97	8.50±0.50	84.72±3.78	76.22±3.85
T3-P1	T27	5	57496	2153	5.59	0.99	5.20±0.30	61.81±4.50	56.61±4.51
	T06	30	50184	1864					
	T26	60-65	26537	1091					
	T05	90	24527	1176					
	T04	115-120	49890	1720					

Table 3.2: Details of sample ^{10}Be concentrations with depth and surface production rate

Terrace id	Sample names	depth or depth interval (cm)	^{10}Be (atoms.g^{-1})	^{10}Be uncertainty (atoms.g^{-1})	Surface Production rate (atoms.g^{-1}.a^{-1})	Topo-graphic shielding	Inheritance from depth profiles (10^{3}atoms.g^{-1}) [b]	Modelled surface conc. (10^{3} atoms.g^{-1}) [c]	Inheritance-corrected surface conc. (10^{3} atoms.g^{-1}) [d]
T3-P1	T31[a]	130-135	41478	1564					
	T28	210-215	12708	702					
	T34[a]	250-255	6332	554					
T3-P2	T11	15	49264	2050	6.09	0.98	5.30±0.40	60.93±5.20	55.63±5.22
	S17	30	36595	1746					
	T14	60	35174	1536					
	S18	90	25973	1462					
	S19	150	11960	762					
	S20	230	6597	544					
T5-P1	T12	10-15	32673	1637	6.27	0.98	6.00±0.40	41.90±3.01	35.90±3.03
	S4	30	26105	1989					
	S5	50	24224	1909					
	T13	75-80	20931	1167					
	S6	150	7118	626					
T3-S1	S11	0-10	54576	3409	5.58	0.97	5.30±0.40	58.06±3.41	52.76±3.43
T3-S2	S22	0-10	46213	2649	5.13	0.98	5.30±0.40	49.16±2.65	43.86±2.68
T4-S1	T09	0-10	40296	1872	5.93	0.98	5.30±0.40	42.87±1.87	37.57±1.91
T4-S2	T08	0-10	42693	1925	5.51	0.96	5.30±0.40	45.42±1.93	40.12±1.97
T6-S1	S12	0-10	19774	1366	5.81	0.98	6.00±0.40	21.04±1.37	15.04±1.43
T6-S2	T10	0-10	29269	1515	7.71	0.97	6.00±0.40	31.13±1.52	25.13±1.57

[a] - Samples processed in UC Santa Barbara and measured in Lawrence Livermore National Laboratory, USA. AMS standard: 07KNSTD3110 (2.85 x 10^{-12}) . Process blank ^{10}Be/^{9}Be: 2.0 x 10^{-16}. Rest of the samples are processed in GFZ Potsdam and measured in CologneAMS, Germany. AMS standard: KN01-6-2 (5.35 x 10^{-13}) and KN01-5-3 (6.32 x 10^{-12}). Process blank ^{10}Be/^{9}Be: 2.2 x 10^{-16}.

[b] - inheritance obtained from 10Be depth profiles (Hidy et al., 2010). For level T3 and T4, average of the two inheritance values (from T3-P1 and T3-P2) is used as model inheritance. For T5 and T6, the inheritance from T5-P1 is used.

[c] - Model surface concentration means either depth-corrected concentration from surface-only samples or Monte-Carlo simulation-derived surface concentration for depth profile samples.

[d] - Inheritance corrected ^{10}Be concentration = model surface concentration - inheritance.
Density: 1.9 - 2.1 g.cm^{-3}.

***Table 3.2**: Details of the ^{10}Be samples with measured concentrations, external uncertainties, surface production rates and inheritance-corrected surface concentrations.*

3.4.2. Surface-exposure ages of fluvial terraces

We identified six terrace levels within the basin and named these T1 through T6, in order of decreasing elevation above the thalweg. We attribute the highest flat terrace remnants associated with well-rounded fluvial boulders (relicts of the AF1 fill) to terrace level T1. This terrace is nearly 200 m above the nearest riverbed, but it provides only a minimum estimate for the height of the Pleistocene fill over the erosional paleo-topography in the Siwaliks. Below T1, terrace level T2 is also sculpted into the AF1 alluvium (with 10s of meters of younger alluvium on top). Heights of T2 vary from 110 to 120 m above the riverbed near the mountain front and 90-100 m above the thalweg near the southern extremity of the basin (Fig. 3.1c) (see Supplementary Figure S3.2 for a regional terrace map). Incision into the alluvium of AF2 generated levels T3 (50 to 55 m high), T4 (40 to 45 m high), T5 (30-35 m high) and T6 (8-10 m high) (Fig. 3.1b, 3.1c). While T3 is the best-preserved terrace level in the Baner Khad watershed, T5 is best preserved in the Gaj Khad watershed.

We sampled two depth profiles for ^{10}Be analysis from the flat AF1 surface remnants within terrace level T1 (T1-P1 and T1-P2, Fig. 3.1b). Near the site of T1-P1, we observed what are probably two different fill units. The thickness of the more pristine, upper fill unit varied from 0.3 – 1.2 m (supplementary figure Fig. S 3.3c). However, at location T1-P1, the more pristine fill was absent, and the top 30 cm of the profile was filled by dark grey-colored clay with very few clasts, indicating mixing of the upper layer probably due to agriculture (see Fig. 3.3c). Alternatively, it could reflect some aeolian input, although we observe no evidence of aeolian input on the other top surfaces we studied. At depths greater than 30 cm, the matrix and granitic clasts show extensive weathering. There is also some irregularity in the expected pattern of exponentially decreasing ^{10}Be concentrations with depth, with the three uppermost samples exhibiting overall similar concentrations (Fig. 3.3a), which is a pattern we expect to find in a layer that has been mixed following deposition (e.g., Perg et al., 2001). Hence, for T1-P1, we explored two scenarios for our Monte Carlo simulations. Scenario A was performed considering that the entire sampled pit represents a single fill unit, whereas scenario B was performed with only the samples deeper than 30 cm. Scenario B provides a surface exposure age (time dependent production model) of 53.4±3.2 ka (Table 3.1) (Fig. 3.3b) and gives a much better fit to all the samples below 30 cm. Scenario A results in a younger exposure age of 40.5±2.7 ka for the depth profile (Fig. 3.3a), with a larger misfit between the observed and simulated ^{10}Be concentrations. Our second depth profile of terrace level T1 is T1-P2, which hosts much more pristine granite and quartzite clasts throughout its 2.5 m depth and yields a surface exposure age of 43.0±2.7 ka (Fig. 3.3c).

From terrace level T2, depth profile T2-P1 yields an exposure age of 16.3±1.0 ka (15.3±0.9 ka from the surface-only sample) and depth profile T2-P2 yields an age of 19.5±2.2 ka (18.6±1.2 ka from the surface-only sample, respectively (Fig. 3.3e, Table 3.1, Appendix A). From terrace level T2, the surface only sample (T2-S1) yields an exposure age of 16.9±1.3 ka (Table 3.1). Details of sample results including ^{10}Be concentrations, topographic shielding, and surface production rates are listed in Table 3.2.

The remaining, lower terrace levels yield Holocene exposure ages. Cosmogenic depth-profile data are reported in our previous study (Dey et al., 2016 in revision- see Chapter 4) for terrace T3 (2 profiles) and T5 (1 profile) (Fig. 4.6, next chapter). Together with two surface-only samples, we calculated a weighted mean exposure age of 9.3±0.4 ka for terrace level T3 (n=4) (Table 3.1). Weighted mean ages from terrace levels T4, T5 and T6 are 6.7±0.4 ka, 5.7±0.5, and 3.1±0.3 ka, respectively (see next chapter for details) (Table 3.1). These results are compiled on the terrace map in Fig. 3.1b.

3.4.3. Paleo-erosion rates

From ~50 to 15 ka, erosion rates recorded within fan AF1 are as low as 0.15 – 0.7 mm.a^{-1}, after which they rapidly increased to 3 to 5 mm.a^{-1} within fan AF2 (Fig. 3.4). The modern erosion rates obtained from a river-sand sample taken from the Baner Khad at the southern extremity of the Kangra Basin (see sample location in Fig. 3.3, Fig. 3.1b) are 1.3±0.2 mm.a^{-1} (Sample ID T0, Table 3.1).

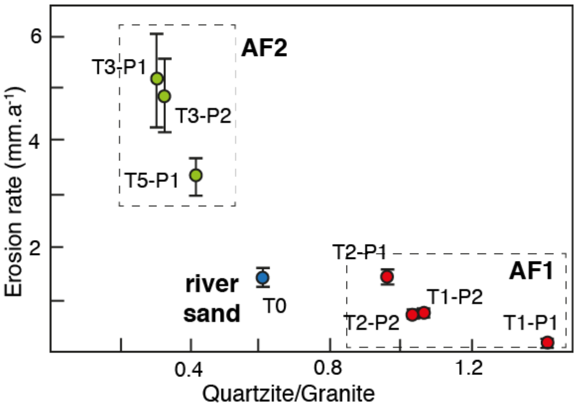

Figure 3.4*: Paleo-erosion rate vs. Quartzite/Granite ratio (from conglomeratic clasts), indicating significant changes in erosion rate and sediment source with time. Erosion rate is inversely proportional to the nuclide inheritance of the deposit. AF2, despite having a higher percentage of granite coming from the Higher Himalaya exposed along the crest of Dhauladhar range with a high ^{10}Be surface production rate (production rates increase with elevation), shows much higher erosion rates compared to AF1, suggesting enhanced erosion and sediment delivery from the Higher Himalaya during upper Pleistocene-early Holocene times. Note that if erosion rates were to stay equal and only the source area changed, we would expect the granite to yield higher ^{10}Be concentrations and hence lower erosion rates.*

3.5. Discussion

3.5.1. Climate forcing of sediment cycle

Climatic changes related to both ISM oscillations and glacial-interglacial cycles are documented in speleothem oxygen-isotope (δ^{18}O) records from Dongge cave, China (Dykoski et al., 2005), the Shillong Plateau of NE India (Dutt et al., 2015), and the Hulu and Sanbao caves, southeast China (Wang et al., 2008) (Fig. 3.5). The isotope trends match well with one another, supporting continent-wide, synchronous trends at 10^3-10^4-year timescales. δ^{18}O records are typically assumed to be inversely proportional to rainfall in the Himalaya, as intensified monsoon circulation and associated convection leads to depletion of the lighter isotope, resulting in lower δ^{18}O values; hence, higher δ^{18}O values during the MIS4 to MIS1 timeframe correlate with the weaker monsoon phases characterized by less precipitation (Wang et al., 2008). Variability in monsoonal strength has been suggested to influence sediment flux in the Himalaya (Bookhagen et al. 2005; Wulf et al., 2010). In the following sections, we will discuss these climate trends and their potential links to sediment cycles in our study area. Such links have been proposed for other areas, but have not been rigorously tested with detailed chronologic data.

3.5.1.1. AF1 aggradation and T1 incision (>60 to <19 ka)

AF1 alluvial-fan remnants represent the oldest preserved upper Pleistocene fill in the Kangra Basin. Only a few OSL and IRSL ages help to constrain the timing of AF1 sediment aggradation (Srivastava et al., 2009; Thakur et al., 2014). IRSL ages of intercalated loess/paleosol levels located in the upper third of the basin fills in the Kangra area (Srivastava et al., 2009) suggest that AF1 aggradation probably started prior to 78.7±17.7 ka. Our exposure ages of terrace remnants yielding ages between 53±3 (depth profile T1-P1) and 43±3 ka (depth profile T1-P2) support these earlier inferences that basinwide net aggradation had ended by ~53 ka.

The difference in our exposure ages for terrace level T1, combined with the different sediment layers exposed in the T1-P1 and T1-P2 pits (see supplementary figure A3) and IRSL-dated loess deposits (Srivastava et al., 2009), suggest at least one minor aggradation phase between ~53 and 43 ka. Our field observations indicate agricultural impact in the top 30 cm of the T1-P1 profile, and the absence of clasts up to that depth horizon indicates mixing of sediments. Therefore, we argue that scenario B provides an accurate assessment of the exposure age (53.4±3.2 ka, Fig. 3.3b), as it excludes the samples from the upper 30 cm of the depth profile. The presence of a ~1.5-m-thick alluvial layer with pristine granite and quartzite clasts on top of the heavily-weathered older alluvial fill near pit T1-P1 and >2.5m of a similar younger fill exposed within pit T1-P2 suggest a second aggradation phase following the ~53±3 ka incision event. Pit T1-P2, which has an exposure age of 43±2.7 ka, indicates a maximum age for the onset of the incision event that followed this minor aggradation phase. If our interpretation of two separate fill units is correct, then pit T1-P1 exposes the older, weathered aggradational unit. We relate this weathered unit to the 'AF1a' aggradation and we consider that the T1-P1 exposure age marks the onset of 'T1a' incision. The less weathered unit exposed in pit T1-P2 could be related to a younger aggradational phase or a lateral shift of a braided fluvial network between~53±3 ka and ~43±3 ka. We refer to the later, short aggradation phase as 'AF1b', which was terminated by the 'T1b' incision phase, which started at 43±2.7 ka (exposure age of T1-P2).

T1a incision, which marks the onset of incision into the oldest-preserved basin fill, commences after the transition from the drier MIS4 to the wetter MIS3 (Fig. 3.5). Stronger monsoon phases with more precipitation would lead to a higher transport capacity and higher incision potential, leading to incision of the AF1a fill. However, incision could be counteracted by an increased sediment flux from the hillslopes. We are unsure of the sediment flux at that time, however, the low basin-wide denudation rates (see section 4.3) suggest that near the end of AF1a aggradation, the sediment flux could have decreased, thus resulting in incision during a time of overall wetter conditions. In addition, it may be hypothesized that during such a humid phase vegetation cover in higher and drier areas eventually stabilized the landscape and counteracted the removal of hillslope material, thus leading to incision of the main stem.

The less-weathered, 'fresh' sediments of the AF1b fill suggest an absence of reworked material and instead a source from the high-elevation sectors of the Dhauladhar Range. Between 55 and 42 ka, stable-isotope trends suggest an overall slight decrease in monsoon intensity with a few short-term excursions toward higher precipitation (Fig. 3.5). Although the minor aggradation event (AF1b) could be associated with one of these short-term events, the available data is insufficiently precise to resolve any clear link. Nonetheless, the alternations between incision and aggradation during MIS3 with no substantial net aggradation or net incision (Fig. 3.5) is likely associated with these short-term variations in monsoon intensity.

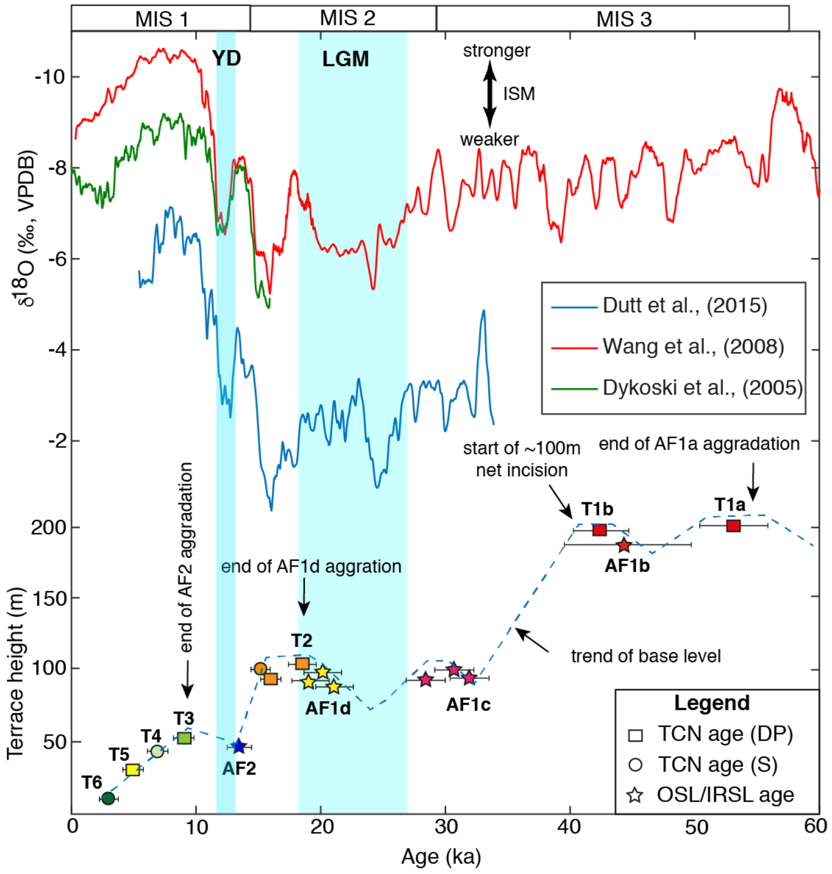

***Figure 3.5**: Terrestrial cave speleothem records from NE India (Dutt et al., 2015), Hulu and Sanbao caves in SE China (Wang et al., 2008) and Dongge cave in China (Dykoski et al., 2005) presented together with OSL-IRSL ages (stars, Srivastava et al., 2009; Thakur et al., 2014), TCN surface-exposure ages from T1 and T2 terrace level (this study), and mean exposure ages from terrace level T3 to T6 (Dey et al., 2016, see Chapter 4) in the Kangra Basin. The periods of aggradation or onset of incision are inferred from the OSL-IRSL ages of the fill, ^{10}Be exposure ages of terraces, and stratigraphic relationships of the deposits. Periods of increasing monsoon intensity are broadly coeval with aggradation, whereas incision of the sedimentary fill happened during periods of decreasing intensity. Overall, net incision has occurred when the ISM has been relatively strong. Terraces are plotted against their surface height and are color-coded using same colors as in Fig. 3.1b, and OSL ages are marked using the same symbology as in Fig. 3.1b. Trends of the base level (reflecting aggradation or incision) broadly follow the change of the ISM intensity.*

3.5.1.2. Pre-- and post-LGM sediment cycle: Renewed aggradation and incision (T2)

Following the formation of T1b (~43 ka), significant sediment removal (including ~80-100 m of river incision) occurred throughout the Kangra Basin until the end of the LGM (Fig. 3.5). However, this substantial net incision was interrupted by two short-lived aggradation events from ~32-28 ka (AF1c) and ~22-18 ka (AF1d), as indicated by previously published OSL data and their stratigraphic relationships (Thakur et al., 2014, Fig. 3.3.1c, Fig. 3.5). Because fill AF1d sits at a lower elevation than AF1c (Thakur et al., 2014), incision of >25 m must have occurred in between the two minor aggradation phases (Fig. 3.5). Interestingly, significant LGM aggradation has been observed primarily in large drainage basins draining the High Himalaya, but has not been recognized along the foothills of the Dhauladhar range, which might be related to the limited glacial cover along its steep southern flanks.

The first (Af1c) aggradation phase started at the beginning of the LGM during a brief period of increased monsoon intensity (Fig. 3.5), indicating that an increased sediment flux was more important than an increased fluvial transport capacity for the fluvial response. The end of that phase has no terrace record preserved. Between AF1c and AF1d aggradation, $\delta^{18}O$ data from NE India (Dutt et al., 2015) show a few variations between low and high intensities of the ISM within an overall weakening trend. Incision during a time of decreased precipitation must result from a decreased sediment flux.

The second (AF1d) aggradation episode was during the latter half of the LGM. This aggradation was possibly related to the growth of Himalayan glaciers and lowering of the periglacial frost-cracking and solifluction zone, causing an increased sediment flux, together with a lower fluvial transport capacity associated with the relatively weak ISM (e.g., Scherler et al., 2015). A pulse of greatly increased sediment flux might have occurred when glaciers rapidly retreated (Dortch et al., 2013; Eugster et al., 2016), and large quantities of sediment stored as moraines in the Higher or Lesser Himalayan valleys were delivered to the fluvial network (resulting in AF1d aggradation), as previous studies recognized (Densmore et al., 2015; Dortch et al., 2013). However, the AF1d aggradation in the Kangra Basin is not volumetrically extensive.

Our ^{10}Be-exposure ages illustrate that the AF1d aggradation phase was followed shortly by incision of the alluvial deposits: our two depth profiles (T2-P1 and T2-P2) in level T2 provide exposure ages of 15.3±0.9 ka and 18.6±1.2 ka. One additional surface sample (T2-S1), located in much more distal part of the Kangra Basin, yielded an age of 15.4±1.0 ka (Fig. 3.1b, Fig. 3.5). These terrace ages correspond to a very weakened ISM towards the end of the LGM (18-15 ka) (Fig. 3.5). During this period (the end of MIS2), the fluvial transport capacity may have been low (if glacial melt water is insignificant), in which case incision can only be explained if the sediment flux was even lower. Another interpretation for this T2 incision phase is that post-LGM glacial retreat had supplied high discharge due to glacial melt water even during the relatively weak monsoon, while the sediment supply was reduced as hillslope erosion, periglacial activity, and mobilization of transiently-stored sediment were minimal.

3.5.1.3. Late Pleistocene/ early Holocene aggradation of AF2 and Holocene terraces

The Indian Summer Monsoon strengthened rapidly after ~15ka, with a short interruption during the Younger Drayas (14-12 ka). It stayed relatively strong until ~6 ka (Dutt et al., 2015; Dykoski et al., 2005) (Figs. 3.5, 3.6). The climate signal (Fig. 3.6) shows that the ISM had significant weaker periods within this overall strong monsoon phase.

There is widespread evidence that the ~15 to 10 ka period correlates with rapid sediment aggradation in the Lesser Himalaya and High Himalayan domains along the Sutlej valley (Bookhagen et al., 2006) and the Dehradun intermontane basin (Densmore et al., 2015). Within the Kangra Basin, Thakur et al. (2014) suggested an aggradation phase from 15 to 11 ka (during increasing ISM strength) based on OSL ages. These regionally correlative events suggest that despite increased precipitation and rising sediment transport capacity, an increased sediment flux to the rivers led to deposition in areas where the rivers encountered low-slope areas, such as, widened valley sections, intermontane basins ,or the foreland (Clift et al., 2012; Gibling et al., 2005). We suggest that transiently-stored material in the form of moraines, fill terraces, and hillslope regolith was mobilized during the strengthened monsoon phase at the transition from MIS2 to MIS1. A sharp increase in the ISM intensity could have also increased the frequency of landslides and debris flows which is observed within the AF2 fill (see supplementary figure S3.3e, S3.3f, S3.3g). This hypothesis is supported by our clast counts, as we observed an increasing amount of unusually large granitic blocks (often >1m in diameter) in the younger alluvium compared to older units (Fig. 3.2); these granitic blocks are derived from the Higher Himalayan granites, presently exposed near the snowy crests of Dhauladhar Range to the north of MCT.

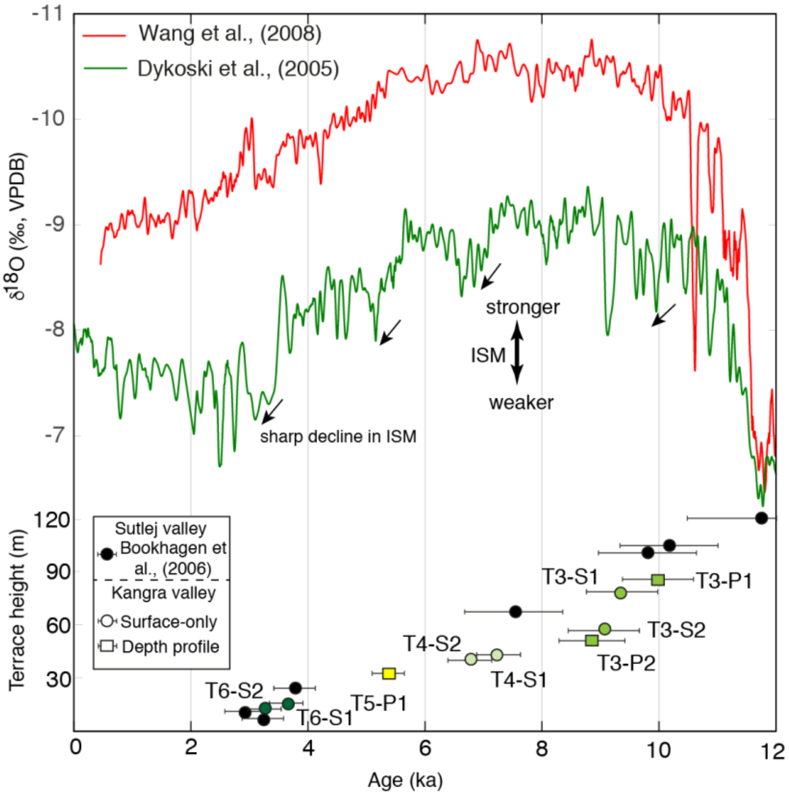

Figure 3.6: *Holocene terrace exposure ages from Kangra Basin (multi-colored squares with error bar showing 1-sigma uncertainties from propagated errors) and from the Sutlej valley (Bookhagen et al., 2006). Terrace exposure ages from the Sutlej valley are recalculated using the same reference production rate and production model as of this study. Oxygen-isotope record from the Dongge cave (Dykoski et al., 2005) and Sanbao cave (Wang et al., 2008) in China shows a steady or increasing monsoon in the early Holocene (~7-8 ka) and a gradual decrease in the monsoon intensity thereafter. Phases of sharp decline in ISM signal are approximately coinciding with the terrace ages. Terrace ages from the Kangra and Sutlej valleys are synchronous within uncertainty.*

The T3 terrace level marks the cessation of AF2 aggradation at ~9.3 ka, while the ISM was still very strong. Since ~ 8-6 ka, however, the ISM subsequently started to weaken again (Dykoski et al., 2005). Our exposure ages of terrace levels T4 through T6, marking the onset of repeated incision phases, illustrate a broad correlation with weakened monsoon phases in Holocene, and they correlate well with exposure ages of terraces in the Sutlej valley (Bookhagen et al., 2006). Incision during this period of decreasing transport capacity requires a decline in the sediment flux. This could have happened due to a decrease in hillslope erosion rates, potentially linked to the removal of easily eroded sediments from the source area during the early MIS1 strong monsoon. Together, the data furnishes support for fluvial aggradation during periods of high or increasing ISM intensity when the sediment flux was high, and incision during periods of low or decreasing ISM intensity, or mostly when the sediment flux was relatively low (Appendix 1; Fig. S3.5).

3.5.2. Impact of tectonic uplift on fluvial incision over Holocene

Activity along the Jwalamukhi Thrust (JMT) has been documented by Dey et al., (2016) (see Chapter 4) based on terrace offsets across the trace of the structure. That work proposed a shortening rate of ~5.6 to 7.5 mm.a^{-1} over the JMT since at least ~10 ka. Slip along the JMT plane has caused differential uplift on the hanging wall, with variations in uplift rate due to a change in the dip angle of the fault plane over the ramp-flat transition. Fill terraces within the Kangra Basin that overlie the flat segment should show a ~1.5 mm.a^{-1} uplift rate associated with tectonic uplift, whereas strath and cut-and-fill terraces on the ramp shows a ~4.5 mm.a^{-1} uplift rate (Dey et al., 2016 –Chapter 4). At steady state, the surface uplift must be balanced by fluvial incision. Hence, we can predict that nearly 15 m of the total incision after the formation of T3 (~9.5 ka) is related to tectonic uplift. However, because post-T3 incision over the flat is 55-60 m, we conclude that a majority of the incision is governed by changes in the balance between sediment flux and fluvial transport capacity within the system, which in turn is governed by climate change.

3.5.3. Changes in paleo-erosion rates with time

In ideal cases, changes in cosmogenic inheritance values reflect changes in the erosion rate of the source area. Alternatively, they may reflect (1) changes in the source of eroding sediment (e.g., higher production rates occur at higher elevation, leading to higher inheritance and lower inferred erosion rates), (2) the transport time of sediment to the sample site, with longer transport times leading to higher nuclide inheritance, or (3) reworking of previously deposited sediments (Anderson et al., 1996).

From fill AF1, the paleo-erosion rate obtained from the inheritance calculated for pit T1-P1 is low (0.1 mm.a^{-1}) compared to the other pit, T1-P2 (0.7 mm.a^{-1}). Similarly, the inheritance from pits T2-P1 and T2-P2 yield erosion rates of and 1.4±0.1 mm.a^{-1} and 0.7±0.1 mm.a^{-1} respectively (Fig. 3.4). From the younger fan unit AF2, much lower inheritance values from profiles T3-P1 and T3-P2 yield paleo-erosion rates of 5.2±0.9 and 4.9±0.7 mm.a^{-1}, while the inheritance from pit T5-P1 yields a rate of 3.3±0.4 mm.a^{-1} (Fig. 3.4).

These differences in paleo-erosion rates may be partly explained by changes in the source area of the sediment and sediment transport histories. T1-P1 hosts strongly weathered and occasionally fragmented granitic and partially-weathered quartzitic clasts, which may indicate reworking of older, more weathered sedimentary deposits, whereas T1-P2 hosts less-weathered and non-fragmented clasts. Pit T2-P2, which yielded a paleo-erosion rate of 0.7±0.1 mm.a^{-1}, hosts weathered clasts, compared to much fresher clasts in T2-P1, which yielded a paleo-erosion rate of 1.4±0.1 mm.a^{-1}. We hypothesize that the faster rates derived from T2-P2 and T2-P2 represents the real paleo-erosion rates, while the slower rates associated with T2-P1 and T1-P1 is a result of the incorporation of an increased amount of older, reworked clasts that contained a higher nuclide inheritance prior to deposition in the fill unit. Although it may be a coincidence, long-term exhumation rates (over ~2-4 Ma) derived from thermochronology data reveal exhumation rates of 1 to 1.5 mm.a^{-1} (Deeken et al., 2011).

In comparison with the AF1 deposits, the upper Pleistocene-Holocene (14- 10 ka) AF2 deposits are less-weathered. Our clast-counts indicate that a significant portion of the AF2 material is derived from Ordovician granites, which are only found in the highly-elevated crest region of the Dhauladhar range (supplementary Fig. S3.4). Despite the high production rates in that area, the profiles show very low inheritance, which corresponds to paleo-erosion rates of 3 to 5 mm.a^{-1}. These results provide strong evidence that during the early Holocene, rapid, deep-seated erosion occurred in the crestal area of the Dhauladhar range, most likely linked to increased erosional processes, such as landslides or debris flow associated with a strengthened monsoon. The sediment transport to the Kangra Basin was fast, with minimal incorporation of older sediment. In line with this interpretation, present day erosion rates are reported to be 2.7±0.3 mm.a^{-1}(Vance et al., 2003) in the Higher Himalayan sector of the northwestern Himalaya, whereas we report a rate of 1.3±0.2 mm.a^{-1} from the Kangra Basin.

3.5.4. The influence of climate change on fluvial dynamics

Our data suggest that climate fluctuations act as a main trigger behind changes in fluvial dynamics of the Kangra Basin without any resolvable lag time. As suggested by Scherler et al. (2015), aggradation in can be explained with the help of hillslope-driven and/or discharge-driven models (supplementary Fig. S 3.5). Increased rainfall may lead to both an increase in hillslope sediment flux due to the higher erosive potential as well as an increase in the fluvial transport capacity due to higher discharge. Because we see a broad correspondence between fluvial aggradation and high or increasing ISM intensity (higher rainfall), our results suggest that sediment cycles of the Himalaya are mostly controlled by changes in hillslope sediment flux. This phenomenon has been observed in other mountainous locations as well, including NW Argentina (e.g., Schildgen et al., 2016), the Pamir (Strecker et al., 2003), the Tien Shan (Huang et al., 2014) and the Apennines (Wegmann and Pazzaglia, 2009); in each case, aggradation appears to have occurred during periods of increasing precipitation, and incision during periods of decreasing precipitation.

3.6. Conclusion

Combining our new surface-exposure data with previously published OSL ages, we infer that pronounced aggradation pulses as well as incision events in the Kangra Basin largely correlate with climatic trends on varying timescales. On 10^4-yr timescales, net aggradation occurred during the first half of the last glacial cycle (~100 to ~60 ka) and net incision occurred during the second half (since ~50 ka). On shorter timescales of 10^3-10^4 years, aggradation occurred during relatively small time windows when the ISM intensity became stronger or weaker, or when the sediment flux was especially high. In contrast, incision into the aggraded material (marked by terrace formation) occurred during periods of weaker or decreasing intensity of the monsoon and when the sediment supply was low. Our constraints on the timing of fluvial incision in the Kangra Basin reveals that it was coeval with incision from the Sutlej valley, suggesting apparently synchronous sediment transport cycles affected by climate change.

Acknowledgements

This study was funded by DFG-GRK 1364 (Deutsche Forschungsgemeinschaft grants to M. Strecker (STR 373/19-2) and R. Thiede (1371/5-1) and DAAD-DST (PPP-India # 57035520) to R. C. Thiede and V. Jain. T. Schildgen is supported by DFG Emmy-Noether grant SCHI 1241/1-1. We thank S. Mukherjee, M. Nennewitz and J. Faruhn for their help with fieldwork and logistics. We thank J. Mey for discussion and suggestions for improving the manuscript. We also thank S. Binnie and S. Heinze from the

University of Cologne for AMS support. We thank D. Burbank and two anonymous reviewers for their constructive and encouraging reviews and A. Yin for editorial handling of this manuscript.

Chapter 4: Holocene internal shortening within the northwest Sub-Himalaya: Out-of-sequence faulting of the Jwalamukhi Thrust, India

Key points

- Out-of-sequence faulting within the Sub-Himalaya orogenic wedge along the Jwalamukhi Thrust since the late Pleistocene.
- Surface-exposure dating of river terraces using ^{10}Be suggests 5.6±0.8 to 7.5±1.0 mm.a-1 shortening along the Jwalamukhi Thrust since ~10 ka.
- Jwalamukhi Thrust accommodates ~40-60% of the total Himalayan shortening within the Kangra re-entrant of the NW Sub-Himalaya since ~10 ka.

Abstract

The southernmost thrust of the Himalayan orogenic wedge that separates the foreland from the orogen, the Main Frontal Thrust (MFT), is thought to accommodate most of the ongoing crustal shortening in the Sub-Himalaya. Steepened longitudinal river-profile segments, terrace offsets, and back-tilted fluvial terraces within the Kangra re-entrant of the NW Sub-Himalaya suggest Holocene activity of the Jwalamukhi Thrust (JMT) and other thrust faults that may be associated with strain partitioning along the toe of the Himalayan wedge.

To assess the shortening accommodated by the JMT, we combine morphometric terrain analyses with in-situ ^{10}Be-based surface exposure dating of the deformed terraces. Incision into upper Pleistocene sediments within the Kangra Basin created two late Pleistocene terrace levels (T1 and T2). Subsequent early Holocene aggradation shortly before ~10 ka was followed by episodic re-incision, which created four cut-and-fill terrace levels, the oldest of which (T3) was formed at 10.1±0.9 ka. A vertical offset of 44±5 m of terrace T3 across the JMT indicates a shortening rate of 5.6±0.8 to 7.5±1.0 mm.a^{-1} over the last ~10 ka. This result suggests that thrusting along the JMT accommodates nearly 40-60% of the total Sub-Himalayan shortening in the Kangra re-entrant over the Holocene. We speculate that this out-of-sequence shortening may have been triggered or at least enhanced by late Pleistocene and Holocene erosion of sediments from the Kangra Basin.

4.1. Introduction

The Himalaya is a tectonically active mountain belt resulting from ongoing collision between the northward-moving, underthrusting Indian plate and the Eurasian plate (Gansser, 1964). The vertical and lateral growth of the Himalaya has been accommodated by several major south-verging thrust systems. From north to south these include the Main Central Thrust (MCT), the Main Boundary Thrust (MBT), and the Main Frontal Thrust (MFT) (Gansser, 1964; DeCelles et al., 2001). All of these north-dipping structures are rooted in the basal décollement, the Main Himalayan Thrust (MHT) (Ni and Barazangi, 1984; Nabelek et al., 2009). These thrust systems also define the regional morphotectonic sectors of the orogen: the Higher Himalaya in the hanging wall of the MCT, the Lesser Himalaya between the MCT and the MBT, and the Sub-Himalaya between the MBT and the southernmost MFT (Gansser, 1964). Although these thrust systems have propagated southward in an overall in-sequence pattern, some out-of-sequence deformation has been reported. Wobus et al. (2005) proposed active out-of-sequence thrusting along the region known as the physiographic transition, south of the MCT in central Nepal. Out-of-sequence faults have also been reported by Mukul et al. (2007) in the Darjeeling Sub-Himalaya, by Thakur et al. (2007) between the MBT and the MFT near Dehradun, and by Powers et al. (1998) in the Kangra re-entrant of the NW Himalaya.

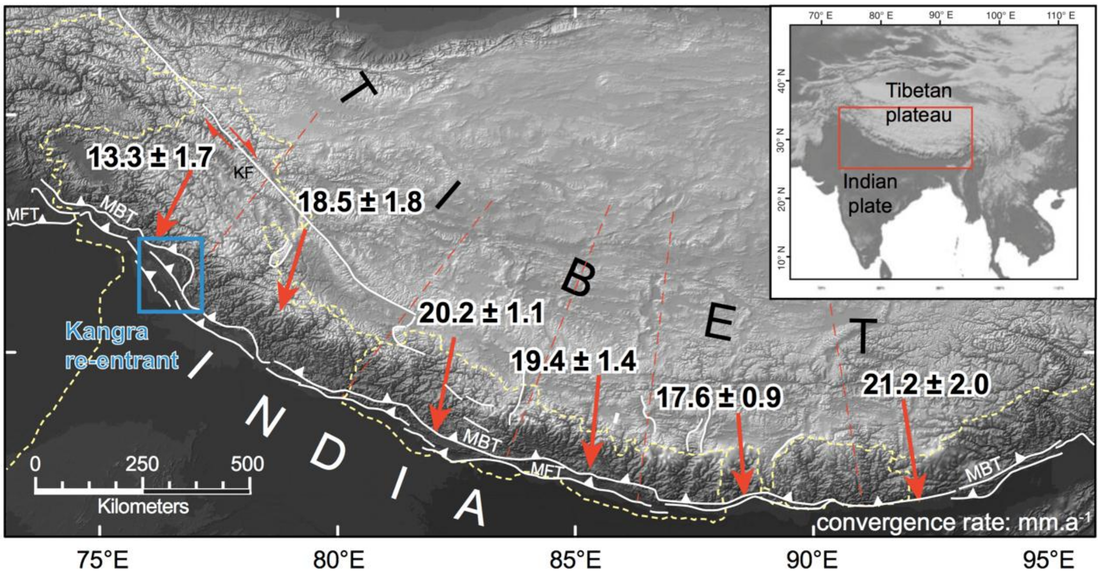

Figure 4.1: *The Himalayan orogen bordering the southern margin of the Tibetan Plateau (inset). Orogen-perpendicular convergence rate (in mm.a^{-1}) of the Indian and the Eurasian plate accommodated within the Himalaya (Stevens and Avouac, 2015). Our study area, the Kangra re-entrant in the NW Himalaya, highlighted by blue rectangle, has the least amount of present-day convergence.*

The 40 to 50 mm.a^{-1} convergence between the Indian and Eurasian plates is partially accommodated within the Himalaya (Lyon-Caen and Molnar, 1985; Avouac and Tapponnier, 1993), where orogen-perpendicular convergence rates vary from 13.3±1.7 mm.a^{-1} in the west to 21.2±2.0 mm.a^{-1} in the east (Ader et al., 2012; Stevens and Avouac, 2015) (Fig. 4.1), and the remainder is distributed farther north. Shortening across the Himalaya is currently accommodated mostly in the Sub-Himalaya, where southward-directed thrusting has resulted in the in-sequence development of an extensive fold-and-thrust belt involving the Neogene Siwalik and Quaternary foreland strata (Powers et al., 1998; Wesnousky et al., 1999; Thakur et al., 2007). An orogen-wide compilation of shortening estimates across the Sub-Himalaya based on balanced and retro-deformed cross sections reveals shortening rates of 3.2±0.7 to 9.7±1.4 mm.a^{-1} since the Middle-Upper Siwalik boundary (Pliocene) (Hirschmiller et al., 2014). Faulting within the Sub-Himalaya has been mainly accommodated by the Main Frontal Thrust (MFT) since the mid-Pleistocene

(Raivermann et al., 1994; Powers et al., 1998; Wesnousky et al., 1999). For example, studies in Central Nepal revealed that the majority of the convergence is accommodated across the MFT, where Holocene shortening rates of ~20±1 mm.a^{-1} have been obtained from deformed fluvial terraces (Lavé and Avouac, 2000), in good agreement with 20±3 mm.a^{-1} of shortening from geodetic measurements (Jouanne et al., 2004; Bettinelli et al., 2006; Stevens and Avouac, 2015). Within the Kangra and Dehradun region of the NW Himalaya, Powers et al. (1998) proposed a total long-term shortening rate of 14±2 mm.a^{-1} and 11±5 mm.a^{-1} respectively across the Sub-Himalaya for the Quaternary (1.9-1.6 Ma). In the same region, Wesnousky et al. (1999) proposed a minimum shortening rate of 11.9±3.1 mm.a^{-1} on the MFT since the Holocene. In the Kangra re-entrant, where the GPS-derived slip rate of the MHT has been estimated at 14±1 mm.a^{-1} (Banerjee and Burgmann, 2002; Kundu et al., 2014), it has been proposed that the bulk of long-term shortening of 8.5±1.6 mm.a^{-1} since 2.7±0.3 Ma (Hirschmiller et al., 2014) has been accommodated along the MFT-system (Thakur et al., 2014).

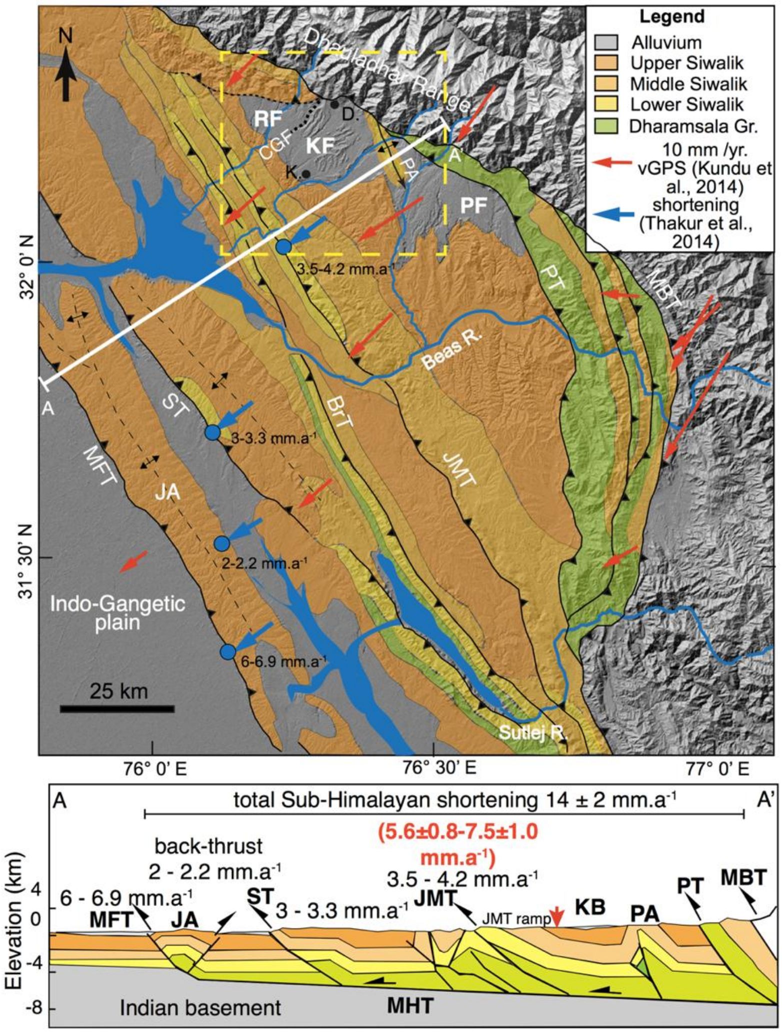

Figure 4.2: Geological map of the Kangra re-entrant in NW Sub-Himalaya, showing the major tectonic structures, lithology and drainages, as well as Pleistocene sediments (after Steck et al., (2003); Thakur et al., (2014)). The inset shows the location of Kangra re-entrant as a red rectangle. The yellow rectangle denotes our study area in and around Kangra Basin (Fig.3 and 5). GPS- motion vectors in the re-entrant are plotted after Kundu et al., (2014) and shortening rates (blue arrows) are plotted after Thakur et al., (2014). A generalized cross-section of the whole Sub-Himalaya along AA' showing the geometry of different structures (modified after

Powers et al., (1998); Thakur et al., (2014)). Shortening rates derived from this study on the Jwalamukhi Thrust (JMT) is shown in bold-red text. Abbreviations: MBT – main Boundary Thrust, PT- Palampur Thrust, BrT – Barsar back-Thrust, ST – Soan Thrust, MFT – Main Frontal Thrust, JA – Janauri Anticline, PA – Paror Anticline, SMA – Surain-Manohargarh Anticline, MHT – Main Himalayan Thrust, CGF – Chambi-Gaj Fault, RF – Rait-Rihlu Fan, KF- Kangra Fan, PF- Palampur Fan.

Recently, Thakur et al. (2014) proposed that crustal shortening in the Kangra re-entrant (Fig. 4.2) is not restricted to the MFT, but rather comprises out-of-sequence thrusting partitioned among several sub-parallel thrusts in the Sub-Himalaya since late Pleistocene time. These thrusts include the Palampur Thrust (PT), the Jwalamukhi Thrust (JMT), the Barsar back-thrust (BrT), the Soan Thrust (ST) and other structures (e.g., the Janauri Anticline (JA) on the hanging wall of MFT and its related back-thrust) that have grown towards the foreland (Fig. 4.1). Thakur et al. (2014) estimated a total shortening rate of 14±2 $mm.a^{-1}$ across various structures in the Sub-Himalaya over the last ~30-40 ka (see Fig. 4.2) based on uplifted strath terraces with OSL-dates of the alluvial cover. Because OSL ages based on samples collected in these deposits determine the onset of sediment aggradation rather than the timing of terrace abandonment (the latter of which provides the age of the deformed geomorphic marker), the deformation estimates from Thakur et al. (2014) are averaged over longer timescales and hence may underestimate true deformation rates.

In the northwest corner of the Kangra re-entrant, the Kangra intermontane basin (Fig. 4.2) stores more than 200 m of late Pleistocene alluvium, which forms a cover on top of tilted Sub-Himalayan strata in the hanging wall of the Jwalamukhi Thrust. This alluvium represents the vestiges of former extensive basin fills that were subsequently re-incised (Sah and Srivastava, 1991; Srivastava et al., 2009; Thakur et al., 2014; Dey et al., 2016), pointing to a potential feedback between sedimentation-erosion cycles and out-of-sequence faulting. Indeed, sediment removal and an accompanying reduction in lithostatic stress can potentially re-activate structures within an intermontane basin, leading to out-of-sequence deformation (Burbank and Raynolds, 1988; Pavlis et al., 1997; Hilley & Strecker, 2005; Pingel et al., 2013). On timescales of 10^4 to 10^6 years, this feedback may be identified and quantified using a combination of sediment archives and landforms, including partially preserved valley fills, alluvial fans, and fluvial terrace systems (Gibling et al., 2005; Kumar et al., 2007). In this study, we have employed river profile analysis, structural analysis, and CRN exposure dating of geomorphic markers (fluvial terraces) in the Kangra re-entrant in order to (1) constrain Holocene fluvial incision and terrace formation and (2) to more precisely evaluate the activity of the JMT within the Sub-Himalaya using a fault-bent fold model.

4.2. Morphometric setting and stratigraphy of the Kangra Basin

The sinuosity of the MBT and the range front results in segmentation of the range into structural re-entrants and salients (Fig. 4.2). In general, structural re-entrants occur where the southward propagation of the deformation front has been less pronounced with respect to neighboring segments. The Kangra re-entrant, the largest one, is located in the foothills of Himachal Pradesh, NW India. The Kangra Basin lies in the NW corner of this re-entrant, bounded by the MFT to the south and a pronounced topographic front to the north. This topographic front is the hanging wall of the MBT and constitutes the Dhauladhar Range. Elevations of the range decrease systematically until it is truncated by the Ravi River in the west and the Beas River in the east. The sinusoidal nature of the MBT causes the termination of the Kangra re-entrant against the Nahan salient on the eastern flank of Beas River (Fig. 4.2).

The Kangra re-entrant comprises a nearly 80-km-wide section of the Sub-Himalayan fold and thrust belt (Fig. 4.2). The Kangra Basin and nearby regions expose deformed sediments dating back to the middle Miocene (~16 Ma) (Rao et al., 1993; Brozovic and Burbank, 2000) (Fig. 4.3). Low-temperature thermochronology indicates that exhumation of the Dhauladhar Range has been ongoing since at least 6-7 Ma (Deeken et al., 2011), thus providing a temporally and spatially well-constrained source for the exposed sediments. These former foreland-basin sediments belong to the Siwalik Group, which includes middle Miocene claystone-siltstone (Lower Siwaliks), late Miocene sandstone and silty claystone (Middle Siwaliks), and late Miocene-Pliocene boulder conglomerates (Upper Siwaliks) (Rao et al., 1993; Brozovic and Burbank, 2000). The Siwaliks are underlain by the early Miocene Dharamsala Group, which is also deformed due to faulting along the JMT and the Palampur Thrust (PT).

An alluvial basin-fill unit of Pleistocene age (Srivastava et al., 2009; Thakur et al., 2014) unconformably overlies all of these strata. The fill constitutes thick, coalesced alluvial-fan deposits comprised of stream-flow and debris-flow sedimentary units within the northern sector of the Kangra Basin, but only a thin veneer covering strath terraces within the southern sector in the hanging wall of the JMT. Limited chronological information based on IRSL (infra-red stimulated luminescence) dating of the alluvium suggests that the Kangra Basin started to aggrade prior to 78±18 ka (Srivastava et al., 2009), and thus a majority of the sedimentary fill accumulated during the last glacial period (~110 to 20 ka) (Dey et al., 2016; Thakur et al., 2014). Subsequent to the basin filling, regional erosion ensued, and fluvial terraces were sculpted into the previously deposited sediments, resulting in re-established fluvial connectivity with the foreland (Srivastava et al., 2009).

4.3. Materials and methods

In this study, we focus on the Rait-Rihlu and Kangra sectors of the Kangra Basin, which are separated by the Chambi-Gaj transfer fault, and drained by the Gaj Khad and the Baner Khad (the local term for river is “Khad”), respectively (Fig. 4.3). To characterize the geomorphic features of the area and quantify parameters potentially indicative of neotectonic deformation, we used on-site field mapping, satellite-derived digital elevation model (DEM) analysis, and cosmogenic–nuclide surface-exposure dating of fluvial terraces. For our geomorphic analyses, we used Cartosat-1, 1 arc-second elevation data (http://bhuvan.nrsc.gov.in/data/download/index.php), which we re-sampled to 30 m resolution. All DEM-related analyses were performed using ArcGIS and/or MATLAB.

4.3.1. Terrace mapping and profile analysis

We delineated fluvial terraces within the Baner Khad and Gaj Khad watersheds both in the field and with the help of DEM analysis to determine their regional extent. We used two different approaches to identify terraces from the DEM. First, to map the spatial extent of different terrace levels, we calculated a slope map from the DEM and identified pixels with slope values of <4 degrees as terraces. In addition, to map the location and heights of the terraces along longitudinal stream profiles, we used functions from the TopoToolbox 2.0 (Schwanghart and Scherler, 2014) to extract longitudinal river profiles and hillslope gradients within a 1-km-wide swath on either side of the thalweg. Thus, a terrace preserved along the river plots as a cluster of near-zero hillslope values above the stream profile on a linear plot of elevation versus stream length.

In the field, we validated our DEM-based mapping, and verified locations, extents, and elevations of pre-mapped terraces using hand-held GPS measurements. To constrain absolute terrace heights, we averaged multiple elevation measurements from the GPS and the DEM. The average of the GPS elevation data from each terrace was used to define the mean terrace elevation, whereas the range of elevation values defines the uncertainty. In addition to the terrace profiles, we extracted the maximum, mean, and minimum elevations within a 2-km-wide swath along the major river channels from the DEM.

Following our mapping of different terrace levels, we determined the volume of sediment that has been removed since deposition of the first alluvial fan deposits in the Kangra Basin. The volume was calculated using the ArcGIS 10.1 3D analysis toolbox and by creating a virtual TIN (triangular irregular network) with the same mean slope as the top of the older fill. The intersection of that virtual TIN surface with the DEM basin boundary yielded a cut-fill volume estimate, the accuracy of which depends on the resolution and process iterations while creating the TIN. The cut-and-fill volume represents the net sediment removed from the basin since the time of maximum basin fill (~50 ka) (Dey et al., 2016).

4.3.2. Stream profiles

Global observations across a broad spectrum of tectonic and climatic regimes have revealed a power-law scaling between the local river gradient and upstream contributing area:

$$S = k_s A^{-\theta} \quad (1)$$

where S is the stream gradient (m/m), k_s is the steepness index ($m^{2\theta}$), A is the upstream drainage area (m^2), and θ is the concavity index (Flint, 1974; Whipple and Tucker, 1999). Normalized steepness-index values (k_{sn}) are steepness indices calculated using a reference concavity value (θ_{ref}), which is useful when comparing steepness-index values from different river systems (Wobus et al., 2006). Following an increase in rock uplift rate, a stream will tend to readjust in a way that will enable faster incision, which typically includes a steepening of its bed and a reduction of its width (assuming constant runoff). As a consequence, the channel gradient will increase first in the downstream reaches of the higher uplift zone and migrate upward. The upstream end of this steepened section is marked by a 'knickpoint' on the river long-profile that separates adjusted, steeper (high k_{sn}) reaches from unadjusted, "relict" (lower k_{sn}) reaches (Whipple and Tucker, 1999). Tectonically generated knickpoints migrate upstream with time (Whipple and Tucker, 1999; Snyder et al., 2000), until, at topographic steady-state, areas of higher rock uplift will be characterized by higher k_{sn} values. In the case of a thrust fault, where spatially variable rock uplift rates result from the increasing dip angle of the thrust plane from the gentle-sloping flat to the steeper ramp, we expect quasistatic knickpoints that separate zones of higher and lower uplift (higher and lower k_{sn} values) (Wobus et al., 2006).

Because river incision through more resistant rocks requires greater stream power compared to less resistant rocks, knickpoints may also be observed near the contact between harder and weaker units, with higher k_{sn} values in areas underlain by harder units (Miller, 1991; Duvall et al., 2004). These knickpoints are generally anchored to the lithologic contacts (Duvall et al., 2004), which helps distinguishing them from transient (tectonically generated) knickpoints and potentially also from quasistatic knickpoints separating zones of differing uplift rates. We extracted stream profiles from the 30-m-resolution Cartosat-1 data using the MATLAB-supported stream profiler tool (www.geomorphtools.org) following the procedure of Wobus et al. (2006). We performed automated k_{sn}

extraction using a critical area of 10^6 m^2 to assign channel heads, a smoothing window of 500 m, and a θ_{ref} value of 0.45.

4.3.3. Valley- floor width to valley-height ratio

The valley-floor width to valley-height ratio is used as a proxy for rock uplift or incision (Bull, 2007). We calculated valley-floor width to valley-height ratios ($Vfw{:}Vh$) using the equation:

$$Vfw{:}Vh = 2Vfw \,/\, ((E_{ld} - E_{sc}) + (E_{rd} - E_{sc})) \qquad (2)$$

where Vfw is the valley-floor width, Vh is the valley height, E_{ld} is the elevation of the river-left valley divide, E_{rd} is the elevation of river-right valley divide, and E_{sc} is the elevation of the thalweg (all in the same length scale) (Bull, 2007). A higher valley-floor width to valley-height ratio is typically associated with lower incision or uplift rates, whereas rapid uplift causes enhanced vertical incision, leading to a V- or I-shaped channel geometry and a lower $Vfw{:}Vh$ ratio (Pinter and Keller, 1995; Bull, 2007). We determined the $Vfw{:}Vh$ ratios of the axial rivers, measured at 400-m intervals along the thalweg. For this measurement, we used the Globalmapper tool on 30-m-resolution Cartosat-1 data.

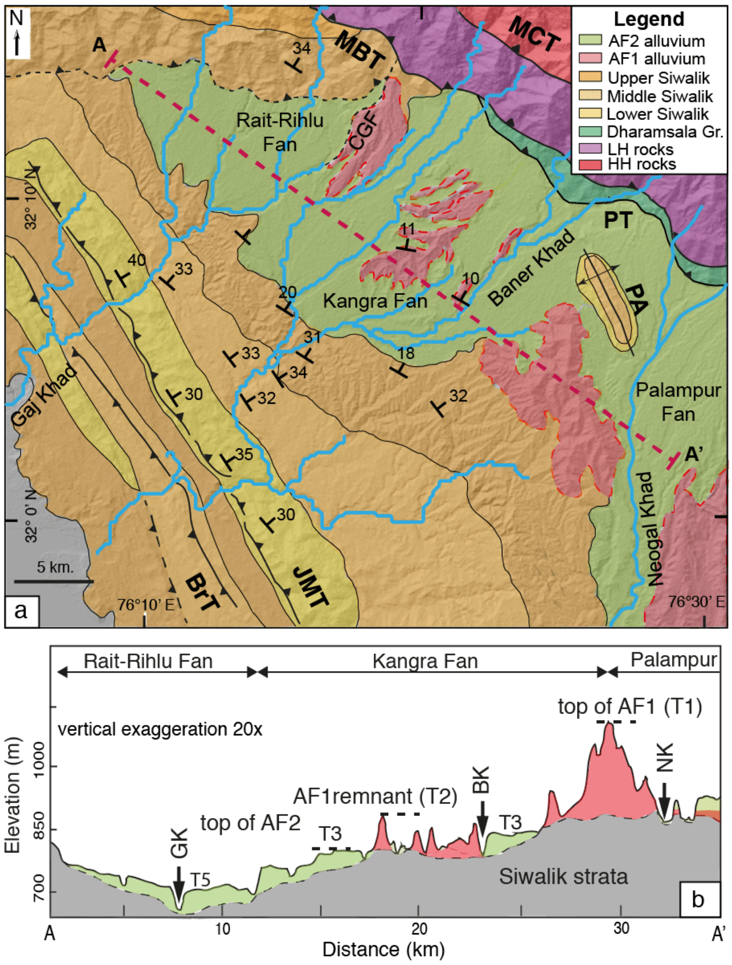

***Figure 4.3**: (a) Geological map of the study area around Kangra Basin showing major tectonic boundaries and lithology along with the structural measurements and alluvial fan sequences. Different sectors of the basin and*

the two alluvial fan remnants (AF1 and AF2) are shown. The line AA' represents transect used for the inset. (b) Schematic cross-section of Kangra Basin, drawn parallel to the mountain front showing the two fan remnants and modern drainage. A and A' are aligned in west to east direction. Abbreviations: LH- Lesser Himalaya, HH-Higher Himalaya.

Table 4.1: Details of sample ^{10}Be concentrations with depth and surface production rate

Terrace id	Sample names	depth or depth interval (cm)	^{10}Be (atoms.g^{-1})	^{10}Be uncertainty (atoms.g^{-1})	Surface Production rate (atoms.g^{-1}.a^{-1})	Topographic shielding	Inheritance from depth profiles (10^{3}atoms.g^{-1}) [b]	Modelled surface conc. (10^3 atoms.g^{-1}) [c]	Inheritance-corrected surface conc. (10^3 atoms.g^{-1}) [d]
T2-P1	T36[a]	0-5	112494	3118	6.16	0.99	8.50±0.50	104.76±6.50	96.26±6.52
	T03	10	92184	3070					
	T35[a]	30	68778	2011					
	S21	60	44591	2256					
	T30[a]	90	29742	990					
	T02	120	23518	1050					
	T01	200-205	21064	1490					
	T32[a]	250	32396	818					
T3-P1	T27	5	57496	2153	5.59	0.99	5.20±0.30	61.81±4.50	56.61±4.51
	T06	30	50184	1864					
	T26	60-65	26537	1091					
	T05	90	24527	1176					
	T04	115-120	49890	1720					
	T31[a]	130-135	41478	1564					
	T28	210-215	12708	702					
	T34[a]	250-255	6332	554					
T3-P2	T11	15	49264	2050	6.09	0.98	5.30±0.40	60.93±5.20	55.63±5.22
	S17	30	36595	1746					
	T14	60	35174	1536					
	S18	90	25973	1462					
	S19	150	11960	762					
	S20	230	6597	544					
T3-S1	S11	0-10	54576	3409	5.58	0.97	5.30±0.40	58.06±3.41	52.76±3.43
T3-S2	S22	0-10	46213	2649	5.13	0.98	5.30±0.40	49.16±2.65	43.86±2.68
T4-S1	T09	0-10	40296	1872	5.93	0.98	5.30±0.40	42.87±1.87	37.57±1.91
T4-S2	T08	0-10	42693	1925	5.51	0.96	5.30±0.40	45.42±1.93	40.12±1.97
T5-P1	T12	10-15	32673	1637	6.27	0.98	6.00±0.40	41.90±3.01	35.90±3.03
	S4	30	26105	1989					
	S5	50	24224	1909					
	T13	75-80	20931	1167					
	S6	150	7118	626					
T6-S1	S12	0-10	19774	1366	5.81	0.98	6.00±0.40	21.04±1.37	15.04±1.43
T6-S2	T10	0-10	29269	1515	7.71	0.97	6.00±0.40	31.13±1.52	25.13±1.57

[a] - Samples processed in UC Santa Barbara and measured in Lawrence Livermore National Laboratory, USA. AMS standard: 07KNSTD3110 (2.85 x 10^{-12}) . Process blank ^{10}Be/^{9}Be: 2.0 x 10^{-16}. Rest of the samples are processed in GFZ Potsdam and measured in CologneAMS, Germany. AMS standard: KN01-6-2 (5.35 x 10^{-13}) and KN01-5-3 (6.32 x 10^{-12}). Process blank ^{10}Be/^{9}Be: 2.2 x 10^{-16}.

[b] - inheritance obtained from 10Be depth profiles [hidy et al., 2010]. For level T3 and T4, average of the two inheritance values (from T3-P1 and T3-P2) is used as model inheritance. For T5 and T6, the inheritance from T5-P1 is used.

[c] - Model surface concentration means either depth-corrected concentration from surface-only samples or Monte-Carlo simulation-derived surface concentration for depth profile samples.

[d] - Inheritance corrected ^{10}Be concentration = model surface concentration - inheritance.

Density: 1.9 - 2.1 g.cm^{-3}.

***Table 4.1**: Sample details with ^{10}Be concentrations and measured uncertainties.*

4.3.4. Surface- exposure dating using in-situ ^{10}Be

We determined surface-exposure ages of the preserved terraces using concentrations of the in-situ cosmogenic radionuclide Beryllium-10 (^{10}Be) from amalgamated pebble samples collected from depth profiles and terrace surfaces, following approaches applied in numerous settings (e.g., Repka et al., 1997; Brocard et al., 2009; Schaller et al., 2009; Schildgen et al., 2012). A description of the general approach can be found in the Supplementary Material. For depth profiles, we excavated a 2.2 to 2.5-m-deep pit in every location and collected samples at roughly 30-cm-depth intervals, including the surface sample, which represents the top 0-10 cm of the profile. We sampled >20-30 granite and quartzite pebbles (2-3 cm diameter) per depth interval. For the surface-only samples, we sampled clasts of similar size from all over the surface (apart from the terrace edges) and from up to 10 cm depth. The absence of gullies on the terrace surfaces and any remnants of thicker soils suggests that if surface erosion has occurred, it has likely been minimal. However, some of the flat terrace surfaces have been used for agriculture for many decades, implying that at least some of our samples will have been affected by erosion and/or mixing of the soil.

Samples were processed at the University of Potsdam, the GFZ Potsdam, and the University of California, Santa Barbara. Samples were crushed and ground to 250 – 500 µm grain size, then magnetically separated and etched with HCl and multiple iterations of 1% HF before further chemical processing. After a final leach in aqua regia, each sample was dissolved in concentrated HF. Subsequently, 150 µg of ^{9}Be carrier was added to each sample. The sample matrix was removed by column chemistry. Ultimately, pure $Be(OH)_2$ precipitate was obtained and oxidized to BeO. 100 µg of Nb powder was admixed with each sample. The targets were pressed and packed for accelerator mass-spectrometer (AMS) measurements at Lawrence Livermore National laboratory (relative to 07KNSTD3110 as standard) and the University of Cologne (KN01-6-2 and KN01-5-3 as standards) (Dewald et al., 2013). Process blanks with a ^{10}Be/^{9}Be ratio of 2.2×10^{-16} (for samples measured at the Cologne AMS) and 2.0×10^{-16} (for samples measured at the Lawrence Livermore AMS), respectively, were subtracted from the measured sample ratios.

All exposure ages reported in this study are based on the time-dependent production rate scaling scheme by Lal (1991) as updated by Stone (2000), provided in the CRONUScalc web calculator version 2.0 (http://web1.ittc.ku.edu:8888/2.0/; Marrero et al., (2016)). Topographic shielding of production rates is based on Dunne et al. (1999) and was calculated based on field measurements with a geological compass and the tool provided by Hidy et al. (2010). To determine surface-exposure ages corrected for nuclide inheritance and surface erosion from the depth profiles, we performed Monte Carlo simulations (1,000,000 iterations) using the simulator provided in Hidy et al. (2010). The nuclide inheritance of each sample determined from depth profiles is assumed to be similar, if the pit represents a single fill. The simulation was done assuming a reference sea-level high latitude (SLHL) total ^{10}Be production rate of 4.01 atoms.g^{-1}.a^{-1} (Borchers et al., 2016), a density of 1.9 to 2.1 g.cm^{-3}, an attenuation length of 160±5 g.cm^{-2} for neutron spallation (Dunne et al., 1999), an erosion rate of 0 to 0.2 cm.ka^{-1}, and a total erosion threshold of 0 to 20 cm. Using a higher erosion threshold results in older ages, but as mentioned above, we saw minimal direct evidence of erosion on the very flat terraces. Also, the tight clustering of our ages from individual terraces argues for minimal erosion. Exposure ages from the depth profiles were first obtained with the Monte Carlo simulator based on the time-independent surface production scaling scheme by Lal (1991) and Stone (2000). The resulting ages were then recalculated for time-dependent production rates using the CRONUScalc web calculator version 2.0.

For locations in which we only collected surface samples, we assume that the samples represent a mixture of 0-10 cm depth from the surface due to bioturbation and anthropogenic overprint of the terrace surface; hence, we applied a shielding factor equivalent to 5 cm depth on the surface production rate to calculate the ages. For the surface-only samples, the ^{10}Be concentration that accumulated since exposure was determined by subtracting the inheritance derived from depth-profiles (from depth profiles of the same terrace level) from the measured concentration of the surface sample. (Table 4.2). For terrace level T3, we used the average of the two inheritance values (from pits T3-P1 and T3-P2) as the model inheritance. For T4, the inheritance of T3 was used, and for T6, the inheritance from T5 (T5-P1) was used. These inheritance-corrected concentrations were used to determine the "Lm" ages with the CRONUScalc web calculator.

4.3.5. Constraining deformation across the Jwalamukhi Thrust (JMT)

We used the recorded offset in the heights of terrace level T3 along Baner Khad across the JMT to constrain the fault displacement since the time of terrace formation. To calculate this offset, we determined terrace heights along a profile line perpendicular to the JMT. We performed two independent estimates of the terrace offset. In the first approach, we used the hillslope-angle plot using the 30-m-resolution DEM (vertical accuracy defined by the relative mean standard error, RMSE, of 3.6 to 4.4 m) along the Baner Khad, where the lower envelope of the hillslope angles <4° was used to identify terrace pixels and a best-fit line through the terraces was then extrapolated to a vertical plane that passes through the JMT. For this analysis, we chose terraces alongside the stream segments that flow perpendicular to the strike of the fault. In a second approach, we used multiple point-averaged elevation data from hand-held GPS measurements in the field to identify the terrace level and quantify its height in multiple locations. We fit linear trends through our GPS measurements from the T3 terrace level on both sides of the fault, and projected those trends onto a N50°E azimuth profile line (perpendicular to the strike of JMT). The difference between the DEM elevations and the multiple point-averaged, GPS-derived ground-control points is ±3 m on average.

In both cases, the elevation difference of the extrapolated terrace level on the vertical plane passing through the JMT denotes the terrace offset (*dz*). To determine the terrace offset and estimate its error, the following equation was used:

$$\mathrm{dz} = (\mathrm{a}-\mathrm{b}) \pm \sqrt{da^2 + db^2} \qquad (3)$$

where *a* is the intercept of the best-fit line on the hanging wall with the fault plane, *b* is the intercept of the best-fit line on the footwall with the fault plane, *da* is the uncertainty in the fit on the hanging wall, and *db* is the uncertainty in the fit on the footwall. Subsequently, based on an assumed fault-bend fold geometry, which has been widely proposed in studies of Sub-Himalayan deformation (Lavé and Avouac, 2000; Mugnier et al., 2004; Mukhopadhyay and Mishra, 1999), we converted the vertical component of the total slip across the JMT into fault displacement and crustal shortening rates.

4.4. Field observations and results

4.4.1. Sediment architecture

Within the Pleistocene alluvial fill of the Kangra Basin (Sah & Srivastava, 1991; Srivastava et al., 2009) at least two generations of alluvial fans have been recognized, which reflect at least two sediment aggradation phases. We name these alluvial fills AF1 and AF2 according to their stratigraphic order (Fig. 4.3). The coarser fraction of the fills constitutes primarily well-rounded, poorly sorted, clast-supported, polished pebbles and boulders of alluvial origin (Fig. 4.4b, 4.4d, 4.4e), although occasional layers of sub-angular, matrix-supported, unsorted boulders record the input of debris-flows. In addition, there are isolated layers of highly angular granite clasts that are underlain by heavily cataclasized fragments, which we interpret as landslide deposits (e.g., Shreve, 1968).

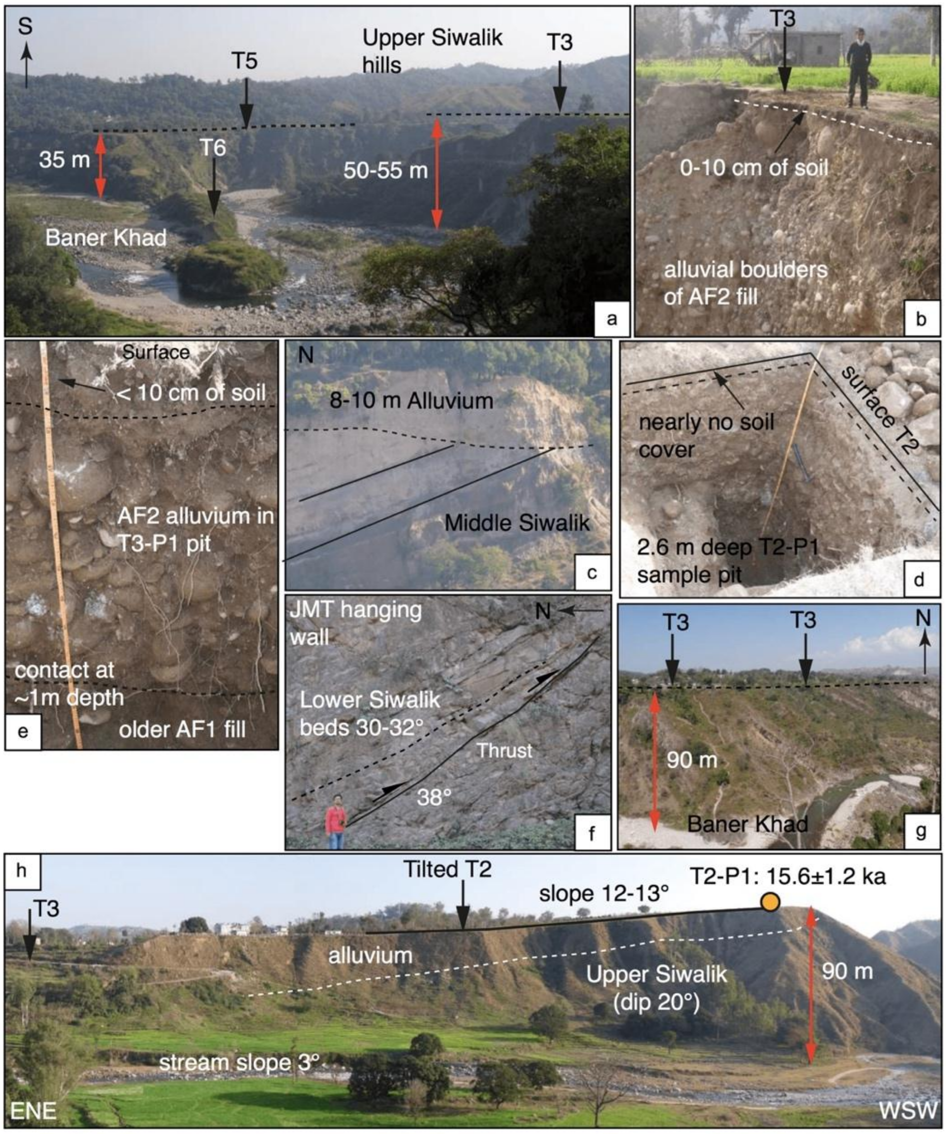

Figure 4. 4: Field photos from the Kangra re-entrant. (a) Different terrace levels sculpted into the AF2-alluvium covering tilted Upper Siwaliks, south of Kangra town along Baner Khad. (b) View of the stratigraphy of alluvial fill within Kangra Basin and T3-surface from the top. Note that most terrace tops are only covered by a thin soil layer (with few well rounded quartz clast ø~2-3 cm) of ~10 cm. (c) Angular unconformity between northeasterly tilted (30°-35°) Middle Siwalik beds and overlying alluvium. (d) T2-P1 pit for cosmogenic radio nuclide (CRN) depth-profile sampling. (e) T3-P1 pit for CRN depth-profile sample pit, again showing very thin soil layer on top, followed by nearly 1 m thick AF2 conglomeratic layer and more strongly weathered AF1 conglomerates

below. (f) Brittle fault zones (dip 38°) in the vicinity of the JMT and the bedding planes (dip 30-32°) of Lower Siwalik units, near the bridge on Baner Khad, near Ranital. (g) Thin alluvial fill (1-2 m) with T3 terrace surface above strath terrace and over the tilted Middle Siwalik beds (hanging wall of JMT). (h) View of north-northeasterly back-tilted terrace T2, to the west of Kangra town, seen from neighboring T3 surface. Slope of the surface and slope of the stream are 12-13° NE and 3°SW respectively. Altogether 15°-16° back tilt of the terrace top-surface occurred since formation. CRN depth-profile T2-P1 (see Fig. 4.6a) has been sampled at the top of this terrace – see orange dot for approximate location.

The older alluvial fan (AF1) has a thickness of up to > 200 m, but is only represented by a few surface remnants in the eastern sector of the Baner Khad watershed, south of the Paror anticline (Fig. 4.3). These remnants can be observed as small hillocks in the center of the Kangra Basin and east of the Chambi-Gaj Fault, south of the town of Dharamsala (Fig. 4.3). The tops of these AF1 remnants at the center of the basin, where the fill thickness is 120 to 140 m, are occasionally flat and have been considered as the highest preserved surface relicts (Dey et al., 2016). The AF1 alluvial fill is late Pleistocene in age, ranging from 78±18 to 17±2 ka based on IRSL data (Srivastava et al., 2009), whereas the highest preserved surfaces have cosmogenic ^{10}Be-based exposure ages of 59±5 ka to 46±6 ka (Dey et al., 2016). The younger fan deposit, AF2, is better preserved and is extensively exposed throughout the basin, with the top of the fill located 55 to 60 m above the river bed. Based on our DEM analyses, we estimate that only 10 to 15% of the original late Pleistocene alluvial fill remains within the basin. The contact between the fill units and the underlying Siwalik strata is mostly a pronounced angular unconformity (Fig. 4.4c). The thick AF1 conglomerates point towards damming or severed drainage conditions in the hanging wall of the JMT; alternatively, they might reflect a fluvial system that was overwhelmed by a massive influx of sediments prior to ~78 ka (Srivastava et al., 2009).

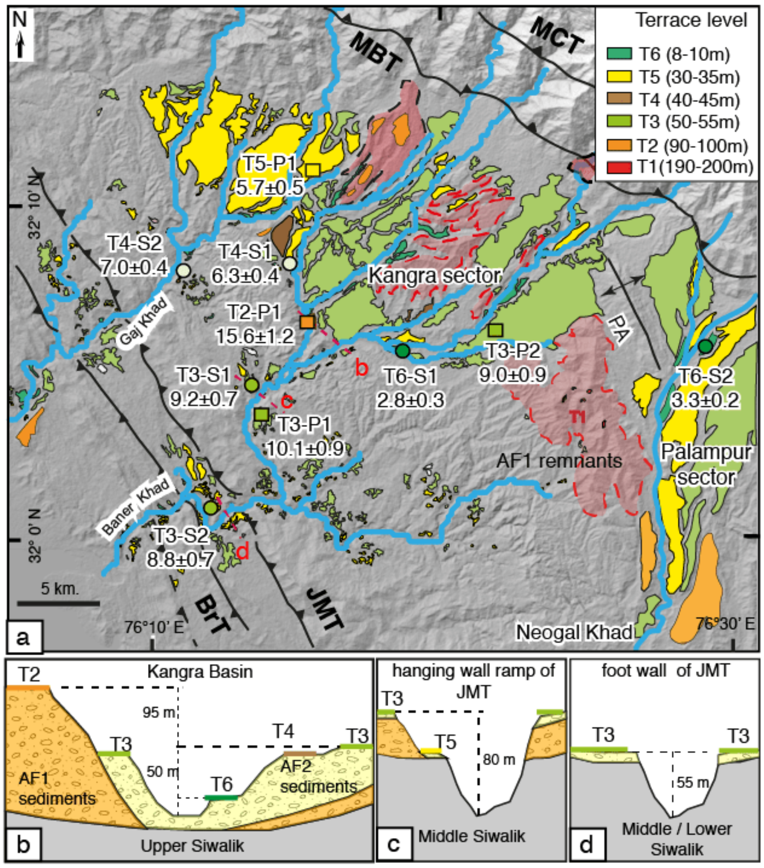

Figure 4.5*: (a) Map of fluvial terraces in Kangra region with cosmogenic radio nuclide (CRN) sampling sites and respective exposure ages. Three cross-sections (a, b and c) are drawn to show how the terrace heights and terrace types vary along the river channel. (a) Within the basin, the terraces are thick fill terraces, whereas in (b) and (c), due to rock uplift in vicinity of the JMT-ramp, the rivers are incising into bedrock (here Siwalik units) forming strath terraces with thin alluvial veneers (Fig. 4.4g) and deeply incised narrow canyons.*

4.4.2. Fluvial terraces

4.4.2.1. Fluvial terrace levels

Fluvial terraces in the northwest corner of the Kangra re-entrant comprise fill (Fig. 4.4a, Fig. 4.4b), strath, and cut-and-fill terraces (Fig. 4.4c, Fig. 4.4g). We observed only fill terraces within the Kangra Basin, where the streams are mostly still incising the Pleistocene alluvium. In contrast, south of the basin, we observed both strath and cut-and-fill terraces. The cut-and-fill terraces comprise 5 to 20 m of alluvium atop a strath terrace carved into tilted Siwalik units over the ramp of the JMT (Fig. 4.2, inset), whereas strath terraces comprise a veneer of less than 1 m of conglomeratic fill over a bedrock strath (Fig. 4.4g). These observations are consistent with the terrace descriptions by Thakur et al. (2014). As described in Dey et al. (2016), we identified at least six terrace levels within the basin and named these T1 through T6, in order of decreasing elevation above the thalweg (Fig. 4.5a). We attribute the highest flat terrace levels associated with well-rounded fluvial boulders (relicts of the AF1 fill) to the T1 terrace level. T1 is nearly 200 m above the nearest riverbed. Below T1, terrace level T2 is sculpted into the AF1 fan remnants. The height of T2 varies from 90 to 110 m above the present day thalweg (Fig. 4.5b). Incision following the AF2 aggradation generated levels T3 (45 to 55 m above the thalweg), T4 (35 to 40 m), T5 (30 to 35 m) and T6 (10 m) (Fig. 4.5b). These different terrace levels reveal important information concerning variations in climate and sediment flux in the region (Dey et al., 2016), but for this contribution, we solely focus on the best-preserved terrace level (T3) as a strain marker that helps us evaluate the degree of Holocene tectonic activity in the Kangra re-entrant. The heights of terrace level T3 above the modern thalweg vary along the course of the Baner Khad. Near the center of the basin, the height of T3 above the thalweg ranges between 42 and 50 m, then gradually increases to ~100 m near the JMT, and after crossing JMT, the height drops again to 50-55 m (Fig. 4.5b, Fig. 4.5c, Fig. 4.5d). Furthermore, a terrace remnant related to level T2 is preserved at the southern extremity of the basin and is back-tilted by 12 to 13° towards the NE. The clasts within the fill are oriented sub-parallel to the surface, showing an angular unconformity with the underlying Siwalik units, which dip more steeply (20 to 22°) to the NE (Fig. 4.4h).

4.4.2.2. Terrace-exposure ages and published OSL ages

In-situ ^{10}Be surface exposure ages of the sampled terraces (Fig. 4.5a) are in agreement with our field observations, revealing successively younger ages with decreasing height above the thalweg. Details of sample locations, depths beneath the terrace surface, ^{10}Be concentrations, surface production rates, topographic shielding factors, and model-derived surface concentrations are listed in Table 4.1; terrace exposure ages and their locations are in Table 4.2. Surface-exposure ages from terrace level T1 (two sub-levels) and T2 (higher sub-level) are reported in Dey et al. (2016).

For the single depth profile from terrace level T2 (T2-P1) (Fig. 4.6a), we obtain a well constrained exposure age of 15.6±1.2 ka (Table 4.1). One depth profile from terrace level T3, located close to the village of Jalari (T3-P1) (Fig. 4e), reveals a more complex pattern of ^{10}Be concentrations. This pattern may reflect two alluvial-fill units interrupted by a period of exposure, as the data appear to define two trends of exponentially decreasing concentrations with depth: an upper trend between the surface and ~100 cm depth, and a lower trend starting between 100 and 120 cm depth and continuing to the bottom of the pit (Fig. 4.6b). However, we did not observe any substantial change in the clast compositions with depth, nor did we recognize any depositional hiatus or soil layer separating the two trends in the samples. The only visible difference was in the clast roundness and the degree of weathering: the upper 1 m of the pit was rich in polished and stronger clasts compared to the lower part of the pit, suggesting the occurrence of a later aggradation event potentially related to a lateral shift of the braided fluvial network, as we observed commonly in the modern river network of the study area. Depth-profile simulations of the upper fill unit (upper exponential trend) furnish a surface-exposure age of 10.1±0.9 ka (Table 4.2, Fig. 4.6b). To simulate the exposure time of the bottom-fill unit, the concentrations of the bottom-fill samples were first corrected for post-burial production using the concentration curve derived from the upper fill unit (we subtracted the post-burial nuclide accumulation from the measured concentrations of the bottom fill unit). Following this correction, the depth-profile simulations of the lower fill suggest that the inferred contact between the two fills was exposed for 6.3±0.3 kyr before the upper fill covered it (Fig. 4.6b). Interestingly, the absolute exposure age for the proposed contact (16.4±0.9 ka, based on adding the exposure age of the upper unit to the exposure duration of the lower unit) is in good agreement with the T2-P1 exposure age (15.6±1.2 ka). The second depth profile in terrace level T3 (T3-P2) yields a surface exposure age of 9.0±1.0 ka (Fig. 4.6c) (Table 4.2). The single depth-profile from terrace level T5 (T5-P1) yields an age of 5.7 ± 0.5 ka (Fig. 4.6d).

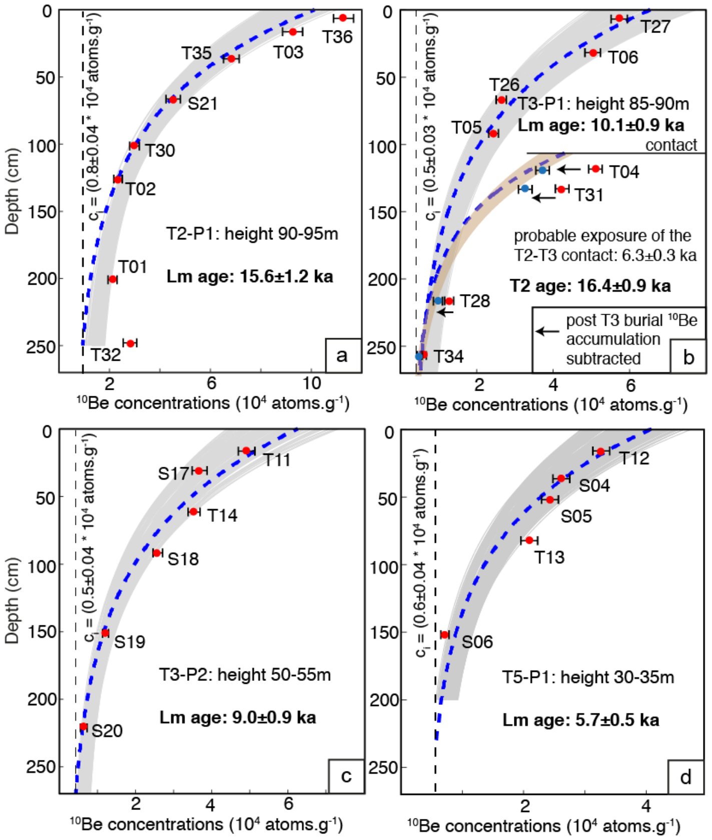

***Figure 4.6**: ^{10}Be concentrations and exposure ages inferred from Monte Carlo simulations of depth profiles, where Ci is the model-derived inheritance and red circles represent the samples from specific depth horizon.*

(see Table 4.1 for details). (a) Depth profile of T2-P1, sampled from the tilted terrace level T2 (see Fig. 4.4g, 4.4h). (b) Depth profile of T3-P1, sampled from terrace level T3 along the Baner Khad. Our favored interpretation is that it comprises two different fill events resulting in two mean trends (red-dashed lines) of ^{10}Be with depth. Due to two-stage filling of the sediments sampled, the concentrations of the samples from the lower unit were corrected for production after the subsequent burial. The blue circles represent the sample concentrations corrected for pre-burial ^{10}Be accumulation. (c) Depth profile of T3-P2 sampled from terrace level T3 along the Baner Khad. (d) Depth-profile of T5-P1 sampled from terrace level T5 along Gaj Khad.

Surface samples from terrace level T3, samples T3-S1 and T3-S2, yield exposure ages of 9.2±0.7 ka and 8.8±0.7 ka, respectively. Two surface samples from terrace level T4, T4-S1 and T4-S2, provide exposure ages of 6.3±0.4 ka and 7.1±0.4 ka respectively. Two more surface samples from the youngest terrace level (T6), T6-S1 and T6-S2, yielded exposure ages of 2.8±0.3 ka and 3.4±0.2 ka respectively (Table 4.2).

In comparison, Thakur et al. (2014) reported OSL ages of the alluvium overlying the Siwalik strath terraces and proposed aggradation phases at ~32 to ~30 ka, ~23 to ~19 ka (both phases considered part of the AF1 fill in this study) and ~14 to ~11 ka (AF2 fill), respectively. Our ^{10}Be exposure ages from the terraces (terrace level T2 sculpted into AF1 remnants and levels T3-T6 sculpted into AF2 fill) postdate the OSL ages that underlie them. Hence, our results are stratigraphically and chronologically consistent with OSL-derived ages of the fill.

Table 4.2: Surface exposure ages from different terrace levels

Terrace id	Latitude (°)	Longitude (°)	Elevation (m)	Inheritance-corrected surface ^{10}Be conc. (10^3 atoms.g^{-1}) a	Mean Surface exposure age with external uncertainty (Lm age) (ka) b, c
T2-P1	32.10649	76.26223	750	96.26±6.52	15.6±1.2
T3-P1	32.05772	76.22650	625	56.61±4.51	10.1±0.9
T3-P2	32.09825	76.34386	750	55.63±5.22	9.0±0.9
T3-S1	32.07733	76.22884	650	52.76±3.43	9.2±0.7
T3-S2	32.01226	76.21296	530	43.86±2.68	8.8±0.7
T4-S1	32.11710	76.26030	715	37.57±1.91	6.3±0.4
T4-S2	32.13490	76.18970	632	40.12±1.97	7.0±0.4
T5-P1	32.18295	76.27620	785	35.90±3.03	5.7±0.5
T6-S1	32.09243	76.33201	690	15.04±1.43	2.8±0.3
T6-S2	32.08780	76.49418	1082	25.13±1.57	3.3±0.2

a - inheritance-corrected ^{10}Be concentrations calculated in Table 1.

b - Lm ages refer to time-dependent Lal (1991) and Stone (2000) production model.

c - Lm ages calculated using SLHL reference production rate of 4.01 atoms.g^{-1}.a^{-1} (Borchers et al., 2016) in CRONUScalc web calculator (Marrero et al., 2016).

***Table 4.2**: Surface-exposure ages (Lm age) of the ^{10}Be samples from T2-T6 terraces along with the sample locations.*

4.4.3. Shortening rate on the JMT

As described in section 4.4.2.1, we relate the change in the height of terrace level T3 across the JMT to recent fault displacement since the time of terrace abandonment, providing us with a time-averaged uplift rate on the JMT-ramp. To calculate the shortening or slip rate, accurate knowledge of the dip of the fault-plane is crucial. In the field, we measured the dip of several fault zones close to the trace of the JMT in the vicinity of the Baner Khad (Fig. 4.4f). We obtained a mean dip of 38° for fault planes cutting the Siwalik bedding, which dips at a slightly lower angle of 32-35° towards the NE. Both Powers et al. (1998) and Prasad et al. (2011) assumed an average dip of 30° for the JMT from seismic reflection profiles at a depth of 2-6 km for a section running parallel to, but ~15-20 km to the east of our study area. Hence, we calculate shortening rates based on three different possible thrust-fault dip angles: the average dip measured in the field (38°), the dip from seismic reflection profile (30°), and a mean of these two dips (34°). In Table 3, we report the resulting range of fault slip (*FS*) and shortening rate (*S*) estimates based on the following equations:

$$FS = U/\sin\theta \quad (4)$$

$$S = U/\tan\theta \quad (5)$$

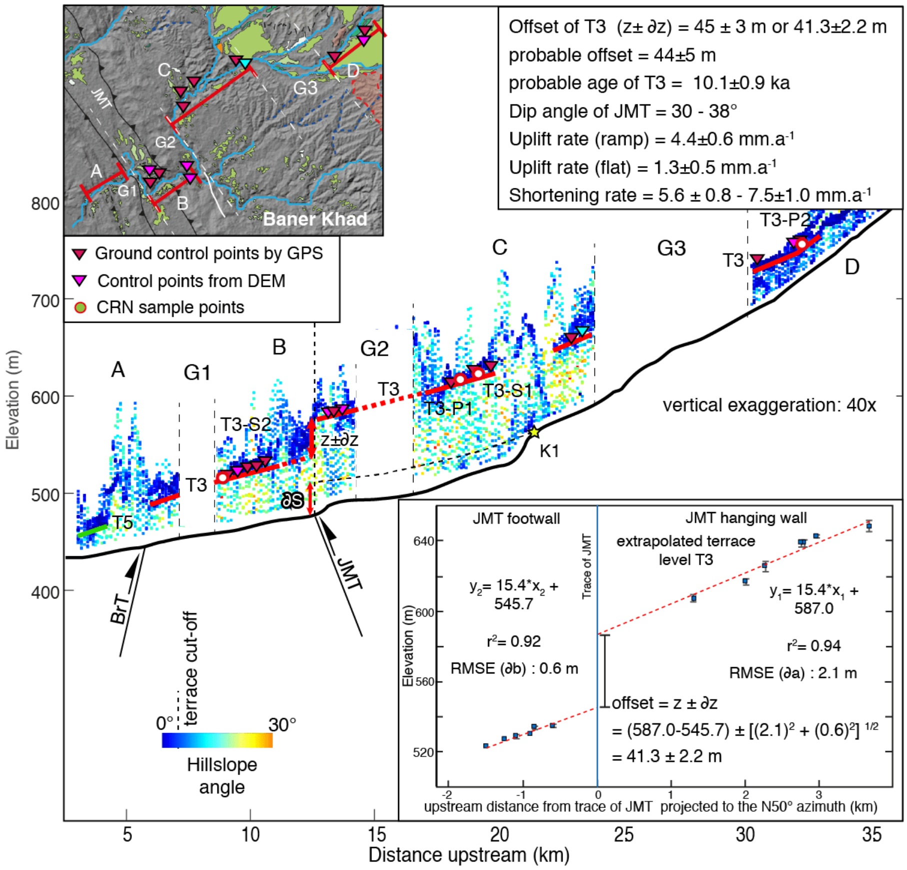

Figure 4.7: Schematic cross-section along Baner Khad showing relative heights of terrace and stream profile. Terrace level T3 (10.1±0.9 ka) is extrapolated along the river profile onto a vertical line representing the trace of JMT. The offset of T3 on that line is equal to the differential uplift across the thrust since the formation of T3.

With a total vertical offset of 44±5 m, the shortening rate across the Jwalamukhi Thrust is 5.6±0.8 -7.5±1.0 mm.a^{-1}.

where U is the uplift rate and θ is the dip angle of the fault plane. We measured the vertical component of the total slip of 45±4 m from the hillslope angle plot derived from the DEM and 41.4±2.2 m from the extrapolated handheld GPS measurements (Fig. 4.7, Table S1). We conservatively estimate that the uncertainty on slip across the JMT spans the cumulative range of these two independent measurements, resulting in an offset of 44±5 m (e.g., Zechar and Frankel, 2009). To determine the slip rate, we used the oldest age obtained from terrace level T3, assuming that the younger ages are likely to have been affected by more erosion. Therefore, our shortening rate (S) estimate ranges between 5.6±0.8 and 7.5±1.0 mm.a^{-1} based on the three different assumed thrust-fault angles (Table 4.3). Considering that there is a change in the dip of the JMT thrust plane from the flat (10 to 12°) to the ramp (30 to 38°) segment, rock uplift above the ramp segment of JMT is ~3.5 times faster than above the flat segment of the JMT.

Our newly obtained shortening rates of 5.6±0.8 to 7.5±1.0 mm.a^{-1} since 10 ka are faster than previously published estimates of 3.5 to 4.2 mm.a^{-1} over the last 30 ka by Thakur et al., (2014), whose estimates were derived from OSL-dated alluvium lying above the uplifted strath surfaces along the Baner Khad (see previous section). These lower rates might be a result of the older ages used for the deformed terraces, which are derived from the timing of alluvial deposition rather than the timing of terrace abandonment.

Table 4.3: Deformation rates on the JMT based on terrace offset, fault dip angle and age of terrace T3

Offset of T3 (m) $_a$	Age of T3 (ka)	Thrust dip (°)	Uplift rate on ramp (mm.a^{-1})	Shortening rate (mm.a^{-1})	Slip rate (mm.a^{-1})
44±5	10.1±0.9	30°	4.4± 0.6	7.5±1.1	8.7±1.2
		34°		6.4±0.9	7.8±1.1
		38°		5.6±0.8	7.0±1.0

$_a$- Offset of T3 is estimated by two independent measurements from the DEM and the hand-held GPS. The difference between these measurements was propagated as uncertainty on the offset value.

Table 4.3*: Estimation of uplift, shortening and slip rates across the JMT based on varying fault-dip angles.*

4.4.4. Fluvial network and stream morphometry

All streams originating from the southern flank of the Dhauladhar Range cross the MBT fault zone to enter the Kangra Basin. There, the channels are generally wider and they meander near the southern margin of the basin. Near the southwestern margin of the basin, several streams converge and only two rivers traverse the tilted Upper-Siwalik conglomerates via narrow and deeply incised gorges across the hanging wall of the JMT and the BrT. As they flow through the tilted Siwalik units, they are characterized by sudden flow-direction shifts from strike-perpendicular to strike-parallel with respect to the WNW-ESE striking JMT/BrT zones (Fig. 4.3, Fig. 4.5) before they cross the fault, where individual fault segments of the JMT terminate and/or overlap.

Longitudinal profiles of the streams traversing the JMT and BrT show overall concave-upward shapes with k_{sn} values ranging from less than 20 to greater than 150 m$^{0.9}$ (Fig. 4.8a). Stream profiles are marked by breaks in slope and changes in k_{sn} values, which we illustrate with an example (Fig. 4.8b).

All streams show relatively high k_{sn} values in the hanging wall of the JMT. These steep stream segments are 4 to 5 km in length (upstream from the trace of the fault) and are marked by knickpoints (K1) at their upstream ends (Fig. 4.7a). These K1 knickpoints occur in both streams where they pass through the Upper Siwaliks and enter the Middle Siwaliks.

There is a good agreement between changes in the Vfw:Vh ratio with changes in the k_{sn} values (Fig. 4.9). For the Baner Khad, the Vfw:Vh ratio is very low in the Dhauladhar Range (< 0.4), but it increases to values of 2 to 4 within the Kangra Basin, and it reaches 5.5 at its southern extremity of the basin (Fig. 4.9). Farther downstream, the ratio falls to 1 when crossing the uplifted Siwalik-strata on the hanging wall of the JMT. Similar low ratios are obtained where the river crosses the BrT. Along the Gaj Khad, the Vfw:Vh ratio is higher (3 to 5) within the Kangra basin and drops to 2 to 3 where it crosses the uplifted Siwalik strata in the hanging wall of the JMT.

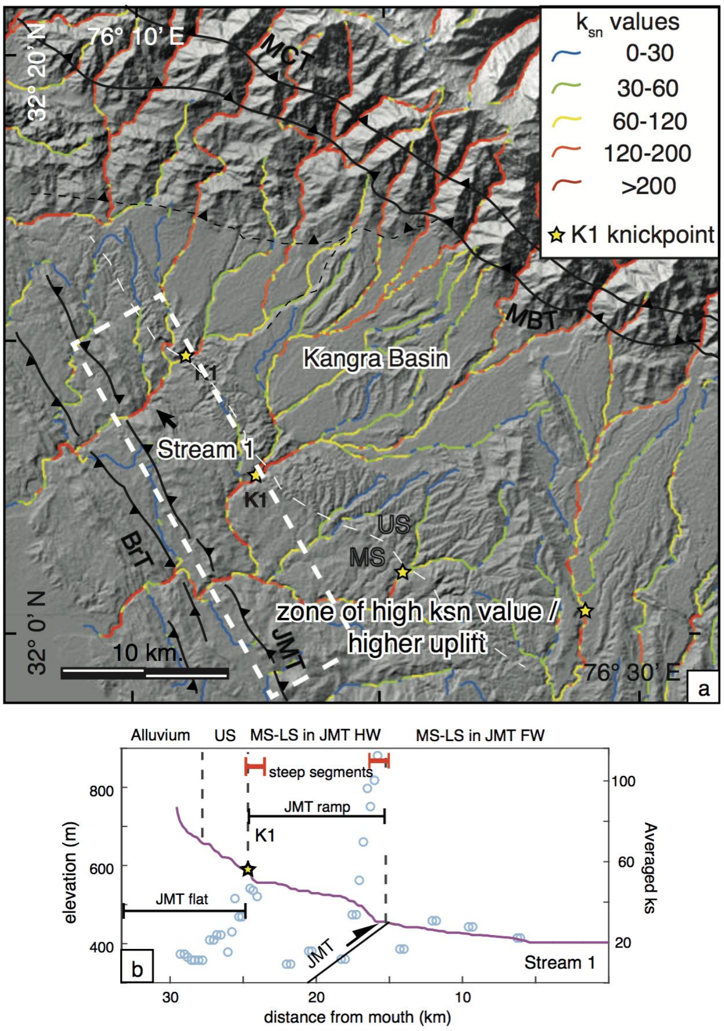

Figure 4.8*: (a) Normalized steepness indices map of the study area showing zones of higher uplift and knickpoint locations on the stream network. (b) Stream 1 (from figure a), shows a longitudinal stream profile across the JMT, where knickpoint K1 reflects the transition from flat-to-ramp on the JMT thrust plane or zone of higher rock uplift.*

4.5. Discussion

Our field observations and results from morphometric and exposure-age analyses reveal several important aspects of the late Pleistocene-Holocene morphotectonic evolution of the Kangra re-entrant. Here, we combine our new data on deformation rates and fluvial incision patterns with previously published OSL-data to (1) better understand the spatial distribution of deformation across the Sub-Himalaya and (2) to explore potential links between the timing of incision and the occurrence of out-of-sequence deformation within the Kangra Re-entrant.

4.5.1. Activity of the JMT

Previous authors have used field relationships, seismic reflection profiles, balanced cross sections, and uplifted strath terraces to quantify the tectonic activity along the JMT (Powers et al., 1998; Thakur et al., 2014) on different timescales, but the age constraints and therefore rate estimates were limited. Powers et al. (1998) proposed that on average, nearly one third of the total Sub-Himalayan shortening (between the PT and the MFT) of 14 ± 2 mm.a^{-1} has been accommodated during the Quaternary. However, this is a minimum estimate, as these authors used the approximate timing of cessation of sedimentation of the Upper Siwaliks to constrain the onset of folding and faulting. They inferred an age of 1.9 to 1.6 Ma for the termination of Upper Siwalik sedimentation based on extrapolation of paleomagnetic profiles located ~15 to 20 km east of the study area and assuming a constant sedimentation rate (Rao et al., 1993). Therefore, their rate estimates may differ from the actual long-term shortening rate. Revised stratigraphic constraints used by Hirschmiller et al. (2014) provide a shortening rate of 8.52±1.6 mm.a^{-1} since 2.7±0.3 Ma, also using an interpolated age of the Upper/Middle Siwalik boundary. However, this boundary is likely time transgressive along strike, and the accuracy of the estimate in the Kangra Basin is difficult to assess. Furthermore, as mentioned in section 4.3, the rate estimates from Thakur et al. (2014) may underestimate the true deformation rates because their OSL ages likely overestimate the abandonment ages of the deformed terraces.

Our new chronologic data and the application of a fault-bend fold model to quantify the deformation in the Sub-Himalaya result in a shortening rate of 5.6±0.8 to 7.5±1.0 mm.a^{-1} across the JMT since 10±0.9 ka (the oldest obtained exposure (abandonment) age of terrace level T3), considering a range of different dip angles of the JMT fault plane. In the following sections, we review our findings in the context of deformed fluvial terraces and the observed knickpoints in stream profiles.

4.5.1.1. Deformation of the alluvium and terraces

Srivastava et al. (2009) suggested a rapid late Pleistocene sedimentation phase (< 78 ka) in the Kangra Basin, which they related to reactivation of the MBT and some other regional faults. The evidence for this fault reactivation, however, is ambiguous, and the sediment aggradation can alternatively be argued to result from a higher sediment supply due to climatic changes on multi-millennial time scales (Dey et al., 2016). In any case, the angular unconformity between the Siwalik units and the overlying Pleistocene alluvial fill (Fig. 4.4c, 4.4h) suggest slip on the JMT was ongoing prior to deposition of the late Pleistocene sediments. The presence of a thin veneer of alluvium on top of the tilted Siwaliks in close proximity to the JMT suggests that sediment deposition in the basin surpassed the basin boundary and also occurred downstream.

In addition to the vertical offset of terrace T3 across the JMT (see section 4.3), we also interpret the 12-13° northeast-tilted T2 terrace surface (Fig. 4.4h) southwest of the town of Kangra to reflect motion along the MHT. Specifically, we suggest that motion along the fault transported the terrace from an initial position above the flat portion of the MHT onto the first thrust ramp segment along the JMT (Fig. 4.9) after terrace abandonment at ~15.6±1.2 ka.

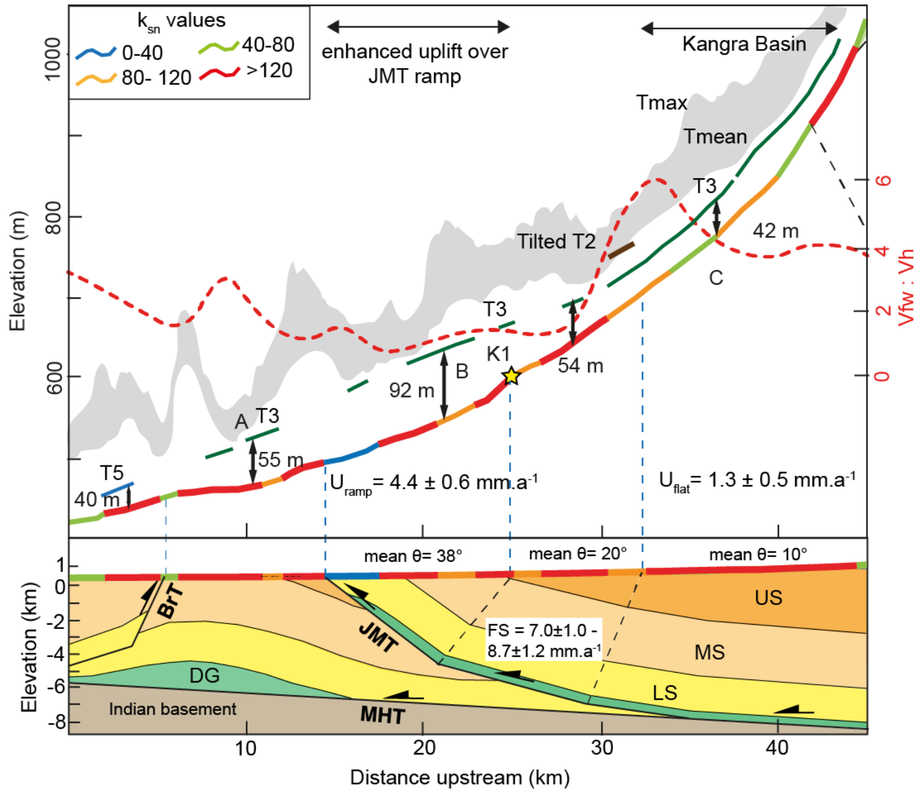

Figure 4. 9: Longitudinal river profiles along the Baner Khad plotted together with terrace profiles, topographic swath (swath window 2 km; Tmax: maximum topography, Tmean: mean topography), valley-floor width to valley height ratio (red dashed line, right axis) and normalized steepness indices. The river profile is characterized by pronounced knickpoints. We interpret knickpoint K1 to be quasistatic, reflecting differential uplift over segments of the fault with differing dips. Segments undergoing faster uplift are characterized by relatively low Vfw:Vh ratios and relatively high k_{sn} *values. Fault slip rate (FS) and uplift rates (U) on the JMT are mentioned.*

4.5.1.2. Morphometric evidence of tectonic activity

Our k_{sn} map (Fig. 4.8a) reveals that streams are characterized by high k_{sn} values ($k_{sn} > 120$) while crossing the JMT hanging wall (above the ramp) and in the 4 to 5 km reach upstream from the fault trace. Farther upstream, k_{sn} values are lower (<60). Knickpoints marking the upstream end of the high-steepness zone (K1) correspond to lithologic contacts (Fig. 4.3, 4.8a), but because this contact is a hard-to-soft transition (partly cemented Upper Siwalik conglomerates are less erodible than the Middle Siwalik sandstones), the K1 knickpoints cannot be lithologically-controlled. If they were, the segment downstream from the K1 knickpoints would have lower k_{sn} values compared to the segment upstream from it. Instead, this set of knickpoints more likely reflects the transition from flat-to-ramp along the JMT thrust, and therefore may represent the northern limit of enhanced uplift rates. Therefore, our favored interpretation of the K1 knickpoints is that they are quasistatic, reflecting spatially differential uplift due to changes in the dip of the thrust plane at depth. This interpretation is supported by our field observations: where we have good constraints on the ramp geometry in our field area, the region of higher k_{sn} and low valley-width to valley-height ratio corresponds well to the inferred position of the ramp (Fig. 4.9).

In summary, our fault-slip rate estimates, k_{sn} patterns, Vfw:Vh ratios, and field observations such as the back-tilted terrace suggest activity of the JMT since at least 18 ka. Our results provide new and independent estimates of shortening on millennial time scales, which complement the previously proposed long-term average tectonic shortening rates (Powers et al., 1998; Thakur et al., 2014; Hirschmiller et al., 2014). Whereas the offset terrace allows us to constrain tectonic uplift due to JMT activity, the k_{sn} values on longitudinal stream profiles provide a qualitative estimate of uplift patterns across the entire region. Different segments of the hanging wall of the JMT are expected to have different uplift rates depending on the dip of the thrust plane. Indeed, the ramp segment with higher rock uplift yields higher k_{sn} values and lower Vfw:Vh ratios, while the flat segment yields lower k_{sn} values and higher Vfw:Vh ratios. In short, our tectonic rate estimates are supported by our morphometric analyses.

4.5.2. Importance of Sub-Himalayan thrusts with respect to a critically-tapered wedge

Previous workers (Powers et al., 1998; Malik et al., 2007; Thakur et al., 2014) have inferred that only the Sub-Himalayan thrusts (JMT, ST, MFT, and related back-thrusts) are accommodating modern crustal shortening. Although potential activity on the MBT has been proposed in the NW Himalaya based on thermochronology data (Deeken et al., 2011; Thiede et al., 2016), which would suggest an overall reduced contribution of Sub-Himalayan shortening, the long averaging time scale of thermochronology data makes it difficult to accurately assess recent activity. Our morphometric analyses of the re-entrant supports these earlier interpretations of the activity of Sub-Himalayan faults, and specifically the JMT (section 4.4). Thakur et al. (2014) proposed a shortening rate of 3.5 to 4.2 mm.a^{-1} on the JMT over the last 30 ka and 6 to 6.9 mm.a^{-1} on the MFT over the last 40 ka. Powers et al. (1998) proposed that 25-30% of the total Sub-Himalayan shortening has been accommodated by the JMT. With our new shortening estimates over the last ~10 ka (5.6±0.8 to 7.5±1.0 mm.a^{-1}), we show that Holocene shortening on the JMT has been comparable to the activity of the MFT estimated over 30 ka (Thakur et al., 2014). Present-day geodetic measurements of shortening in the Kangra re-entrant have been estimated at 14±2 mm.a^{-1} (Banerjee and Burgmann, 2002; Kundu et al., 2014) and 13.3±1.7 mm.a^{-1} (Stevens and Avouac, 2015), whereas underthrusting of the Indian plate has been estimated to be ~4 mm.a^{-1} (Bollinger et al., 2004). Combined with our new results, the data reveal that the JMT accommodates ~40-50 % of the total convergence across the NW Himalaya at least since the Holocene. Hence, it appears as if the majority of the Holocene shortening has been nearly equally distributed over the JMT and other Sub-Himalayan thrusts (including the MFT) in the Kangra re-entrant.

To try to explain why so much Holocene shorting has been accommodated within the interior of the Sub-Himalaya in the form of out-of-sequence faulting, we consider the critically-tapered wedge model (Davis et al., 1983). In analogue and numerical models of critically tapered wedges, changes in sedimentary load have been shown to influence the location of faulting (Davis et al., 1983). Sediment aggradation within intermontane valleys or near the front of a wedge can potentially increase the taper and thus induce foreland propagation of deformation to maintain critical taper (Dahlen, 1988; Willett & Beaumont, 1994; Hilley and Strecker, 2004). Conversely, removal of stored sediments in intermontane basins lower the frontal taper, rendering it sub-critical, and hence causing the retreat of the deformation front and out-of-sequence thrusting, until the wedge re-establishes its critical taper (Dahlen, 1990). The applicability of the critical taper model for the whole Himalaya is highly debated and is certainly oversimplified. Nonetheless, it has commonly been used as a first-order framework to explain the tectonic evolution and deformation of the frontal fold-and-thrust belt of the Himalaya, as this region satisfies the mechanical criteria for the evolution of a critical Coulomb wedge (Hilley and Strecker, 2004; Mugnier et al., 2004; Mukul et al., 2010; Singh et al., 2012; Hirschmiller et al., 2014).

In this context, the deformation pattern within the Sub-Himalaya may be linked to the history of sediment aggradation and removal in the Kangra re-entrant. Considering an initial in-sequence development of the major thrusts within the Kangra re-entrant, the JMT must have once been the southernmost deformation front of the Himalayan wedge. With continuous convergence between the Himalaya and the underthrusting Indian plate, new surface-breaking thrusts emerged, extending the MHT décollement towards the foreland. Based on balanced cross-sections and seismic profiles, a total shortening of ~23 km over the last 1.6-1.9 Ma within the Sub-Himalaya has been estimated (Powers et al., 1998). From these cross-sections, we can deduce a total shortening on the JMT of 6 to 6.8 km and obtain long-term average shortening rate of 3.6±0.3 mm.a^{-1}. From the same balanced cross-sections, we can deduce a long-term average slip rate of 0.7±0.2 mm.a^{-1} on the MFT. These rates are significantly below slip estimates averaged since the late Pleistocene or Holocene, including those from Thakur et al., (2014) and from this study. This inconsistency between short- and long-term slip estimates points to temporal variation of fault activity throughout the last 1.6-1.9 Ma, possibly with periods of low or no activity.

Sediment cycles operate on 10^4-10^5 year timescales and can potentially influence tectonic stress-fields by changing the sediment load (Hilley and Strecker, 2004; 2005). Extensive aggradation reaching up to the contiguous foreland around 40-50 ka has been reported by many previous studies (Gibling et al., 2005; Clift et al., 2012; Thakur et al., 2014; Dey et al., 2016). Late Pleistocene sediment aggradation of more than 200 m across the Kangra Basin (from ~80–20 ka) (Srivastava et al., 2009; Dey et al., 2016) spanning more than ~1500 km^2 over the hanging wall of the JMT may have stabilized the critical taper involving the JMT- MHT during times of high loading and therefore forced deformation to localize towards the frontal structures of the wedge. Later, when the transiently-stored basin-fill sediments were excavated (only 10-15% of the total volume of sediments stored during full-basin stage remains at present on the hanging wall of JMT), the effective normal stresses on the décollement of the JMT would have been reduced, potentially leading to a sub-critical taper (Singh et al., 2012). By transfer or renewal of out-of-sequence fault activity to inherited structures such as the JMT within the Kangra re-entrant, the critical taper would have been restored. Although detailed modeling is necessary to test these ideas in detail, the coincidence in the timing of sediment excavation from the Kangra Basin with an apparent increase in slip rate along the JMT provides a compelling argument for linking the two events in the context of a critically tapered wedge.

4.6. Conclusions

Within the Kangra intermontane basin, deformation of well-preserved Holocene terraces indicates neotectonic activity along the Jwalamukhi Thrust (JMT). The basin hosts evidence for at least two aggradation and incision sedimentary cycles during late Pleistocene to Holocene times. The latest of these aggradation periods was succeeded by episodic re-incision and terrace abandonment, creating at least four terrace levels (T3-T6) during the Holocene, the oldest and best-preserved of which (T3) was formed at 10.1±0.9 ka. Differential uplift of 44±5 m of the best preserved terrace level (T3) across the JMT suggests out-of-sequence faulting along the JMT and yields a shortening rate of 5.6±0.8 to 7.5±1.0 mm.a^{-1} over the last ~10 kyr. In the context of recently published shortening rates averaged over the past ~2 Myr (Powers et al., 1998) and 30 to 40 ka (Thakur et al., 2014), as well as GPS-derived shortening rates (Kundu et al., 2014), our results suggest that a significant proportion of the shortening has been accommodated by the JMT over the Holocene. This shortening corresponds to about 40 to 60% of the total Sub-Himalayan shortening, or 30 to 50% of the total convergence accommodated within the Himalaya. We propose that the recent out-of-sequence faulting that we document along the JMT is potentially related to a tectonic reorganization triggered by temporal variations in sedimentary loading within the toe area of the Himalayan orogenic wedge.

Acknowledgements

The digital elevation data used for this study is 30 m Cartosat 1 data downloaded from http://bhuvan.nrsc.gov.in/data/download/index.php (satellite program from Indian Space Research Organization). CRN data are listed in the provided tables and GPS data from the terraces are listed in Supplementary Table S1. Additional information for CRN age calculations and terrace offset measurement are provided in Appendix 2. This study was funded by DFG-GRK 1364 (Deutsche Forschungsgemeinschaft grants to M.R. Strecker (STR 373/19-2) and R. C. Thiede (TH 1371/5-1). T. Schildgen is supported by DFG Emmy-Noether grant SCH 1241/1-1. We thank S. Mukherjee, V. Jain, and J. Faruhn for their help with fieldwork and logistics, and we thank S. Binnie for AMS support in Cologne. We thank G. Zeilinger, W. Schwanghart, and J. Mey for discussions, A. Whittaker and H. Sinclair for their constructive reviews on an earlier version of this manuscript. We thank D. Grudjic and two anonymous reviewers for constructive and helpful reviews and C. Faccenna for editorial handling and suggestions.

Chapter 5: Deep-seated exhumation along the Tectonically Active MBT: The Dhauladhar Range in the NW Himalaya

Key points

The cooling pattern of new and previously published ZHe and AFT combined with 3D thermokinematic modeling reveal that:

- The MBT emerges along the southern foothills of the 5 km-high Dhauladhar range and forms a deep-seated fault ramp where rocks exhume from a crustal depth of 8–10 km, which implies mean geothermal gradients since at least the mid-Miocene.
- Our modeling results indicate that the obtained ZHe and AFT cooling could only be obtained by mean slip rates on the MBT fault ramp of ~2–3 mm.a^{-1} since the fault ramp's activation, which means ~2 mm.a^{-1} of crustal shortening across the Himalaya have been accommodated by the MBT in this segment of the orogen over a Myr timescale.
- These results imply significant along-strike structural variations of the Himalayan wedge compared to the structural architecture of the Central Himalaya.

Abstract

This study yielded interesting constraints on deformation patterns across the Himalayan orogenic wedge and its along-strike variation. Other studies have proposed classic Himalayan models for orogenic domains to the east, where the internal structure of the basal décollement — the Main Himalayan Thrust (MHT) — forms a time-transient mid-crustal ramp, Precambrian-Proterozoic sediments covering the underthrusted Indian basement are detached from the footwall, and the underthrusted Indian craton is incorporated into the Himalayan wedge in the form of the Lesser Himalayan duplex. This first-order tectonic feature of the orogenic wedge is missing within the Dhauladhar range segment. New zircon helium (ZHe) ages combined with existing low-temperature data sets (ZHe, apatite fission track (AFT)) across the Dhauladhar range yield new constraints on its exhumation history. Additional field observation and 3D thermokinematic modeling (PECUBE) suggest that the range bounding the Main Boundary Thrust (MBT) in this sector (a) has been tectonically active, (b) has propelled the growth of the >5000 m-high frontal Dhauladhar range, and (c) has accommodated deep-seated exhumation since at least the mid-Miocene. Our modeling results indicate that the obtained ZHe and AFT cooling ages could only be explained by mean slip rates of ~2–3 mm.a^{-1} on the ~40 km-long MBT fault ramp. As such, a fraction (~1.3-2 mm.a^{-1}) of the total convergence has been accommodated since the establishment of the deep-seated MBT ramp, which most likely merges directly into the MHT.

5.1. Introduction

Various orogenic growth models have been proposed to explain the evolution of the Himalayan wedge extending for over 1000 km from the Sutlej-Beas region of NW-India into central Nepal since the Miocene, but the sections that structurally deviate from the classic Central Nepal Himalayan sector are comparatively less studied and raise questions about the applicability of these orogenic growth models to the entire Himalaya. The classic central Himalayan wedge is topographically characterized by a sharp physiographic transition forming a broadly developed Lesser Himalaya with rather moderate relief and topographic peaks (mostly ≤ 3000 m), to the rapidly rising Greater Himalaya with high relief and peaks > 6000 m (Duncan et al., 2003; Wobus et al., 2003; Lave and Avouac, 2001). It has been shown that this physiographic transition correlates with major knickpoint zones along major orogen-crossing longitudinal river profiles (see Seeber and Gornitz, 1983), high fluvial incision rates (Lave and Avouac, 2001), and the occurrence of exceptionally young mineral cooling ages (Robert et al., 2011; Herman et al., 2010; Blythe et al., 2004). All these findings suggest higher regional rock uplift and exhumation rates within a ~30–50 km-wide zone upstream of the physiographic transition (PT) zone (Hermann et al., 2010; Thiede et al., 2009). Structural, petrologic, and thermochronologic studies indicate that the exposed high-grade rocks have been rapidly uplifted and exhumed from a mid-crustal depth since the mid- to late Miocene (e.g., Thiede et al., 2013 and 2009; Hermann et al., 2010; Vannay et al., 2004; Jain et al., 2000; Lat et al., 1999; Sorkhabi et al., 1996). This zone of localized rock uplift and deep-seated exhumation is exposed within the orogenic wedge ~150 km north of the orogenic front. The clustering of microseismicity below this physiographic transition zone has been ascribed to a mid-crustal ramp in the basal décollement (the Main Himalayan Thrust (MHT)) underlying this transition zone (see Avouac, 2007) and been related to the growth of Lesser Himalayan duplexes (see Hermann et al., 2010; Thiede et al., 2009; Bollinger et al., 2004; Vannay et al., 2004; Cattin and Avouac, 2000). Despite this rapid exhumation, studies of permanent geodetic networks indicate that the majority of crustal shortening is accommodated along the MFT (Lave and Avouac, 2000) and not along the orogen interior. In contrast to these findings from the Central Nepal sector, The entire NW Himalaya is characterized (Figure 5.1) by strongly undulating MBT fault bounding on the topographic range front and has formed extensive Himalayan re-entrant structures (such as the Kangra and Dehradun re-entrants) where the exposure of the Lesser Himalaya is limited to a narrow width (≤10 km), while the active fault systems bounding the Himalayan wedge to the south — the Main Frontal Thrust (MFT) — remain relatively uniform and arc-parallel. Recent studies in the Kangra re-entrant indicate (a) significant crustal shortening and strain partitioning to the north of the MFT fault system due to out-of-sequence faulting in the Sub-Himalaya (Dey et al., in revision; Thakur et al., 2014; Powers et al., 1998) and (b) ongoing deep-seated exhumation in the hanging wall of the Main Boundary Fault (MBT) (Deeken et al., 2011), suggesting a possibly ongoing crustal shortening accommodated in the hanging wall of the MBT in this segment. An improved understanding of the structural architecture of the frontal faults is therefore essential to understanding the lateral variation in the growth of the Himalayan wedge, which also has important implications for understanding the orogen-wide seismotectonics.

In this study, we focused on an orogen-perpendicular southwest-northeast-oriented traverse across the Kangra re-entrant, Dhauladhar range, and neighboring Chamba region of the Northwest Himalaya in Himachal Pradesh, India (Fig. 5.1). This is located northwest of the Sutlej River and adjacent to the classic central Himalayan tectonic setting (Figs. 5.1b and 5.2). This sector of the NW Himalaya is less studied than areas in the central Himalaya and is significantly diverted, with a distinctly different topography and tectonic and geological setting (Webb, 2013; Deeken et al., 2011; Webb et al., 2011; Yin et al., 2006; DiPietro and Pogue, 2004). To better constrain the temporal and spatial evolution of this range-front segment and to further elaborate its structural uniqueness, we add new thermochronology data to previously published ones by Deeken et al., (2011). We applied PECUBE thermokinematic modeling to obtain better control over the exhumation rates and were therefore able to come up with improved mean fault displacement rates on the MBT. More specifically, seven new zircon (U-Th)/He (ZHe) ages yielded Pliocene-reset cooling ages, implying rapidly ongoing depth-seated exhumation in the MBT hanging wall within this range front segment since at least the late Miocene. By combining the new physiographic analyses, the available thermochronologic dataset, and 3D thermokinematic modeling (PECUBE, Braun et al., 2012, 2003; Robert et al., 2011), we were able to test how well the various structural models matched with the obtained cooling age patterns. This study allowed us to yield better constraints on the MBT fault displacement and related exhumation rates. The combined results of this study provide new constraints and allow implications to be made about the regional structural architecture of the Himalayan wedge within this orogenic segment. For instance, we estimated the north-south extent of the MBT fault ramp and consequently propose that this fault ramp is most likely deep-seated and converges directly to the basal décollement of the MHT, in contrast to earlier suggestions (see Webb et al., 2011).

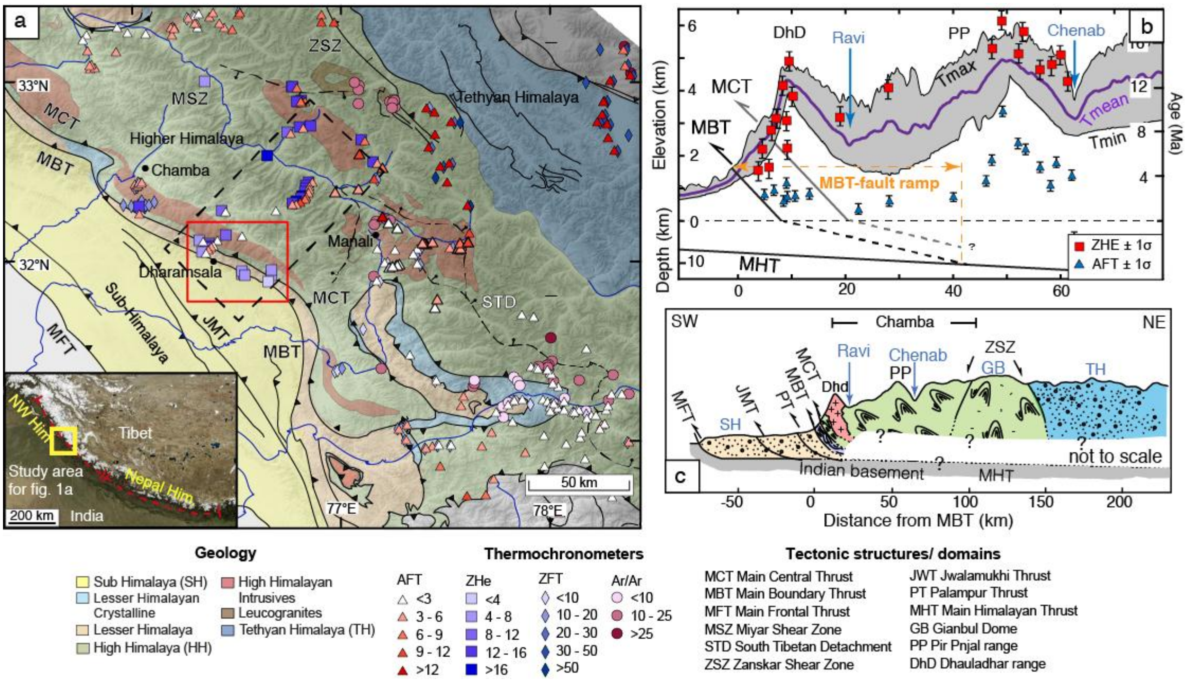

Figure 5.1: Geology of the NW-Himalaya with a compilation of low-temperature cooling ages. (a) Generalized geologic map modified from Steck (2003) and draped over STRM 90m DEM. New and compiled zircon ^{238}*U-Th/He data (ZHe), apatite (AFT) and zircon fission track (ZFT), and* ^{40}*Ar/*^{39}*Ar white mica data. For precise sample location of individual ZHe ages see Tab. 1. Published low-temperature chronology are from (Deeken et al., 2011; Jain et al., 2000; Kumar et al., 1995; Lal et al., 1999; Schlup et al., 2003; Schlup et al., 2011; Thiede et al., 2004; Thiede et al., 2005; Thiede et al., 2009; Vannay et al., 2004). Black dashed polygon indicates location of the swath profile (b) and simplified geologic cross section of Chamba (c). (b) Topographic swath profile across Chamba and in the hanging wall of MBT, running perpendicular to the major morphotectonic units. AFT and ZHe data are projected onto the transect (plotted with respect to their age and not their sample elevation). Bold violet line (T mean) denotes mean elevation, whereas black line (T min/T max) minimum and maximum elevation. Note the scale change of the depth below sea level and elevation. Orange dashed line indicate the extent of the MBT-fault ramp based on extent of young AFT ages despite large elevation changes. (c) simplified geologic cross section with respect to the location of the MBT modified after Steck (2003), running*

parallel to swath profile in b. The exact geometry of the geologic units and structures at deeper crustal level is poorly known; therefore, parts of the cross-section is kept white.

5.2. Geologic setting of the Dhauladhar range and field observations

In general, the central Himalayan wedge can be divided into fault bounded tectono-stratigraphic units exposed from south to north, where the Main Frontal Thrust (MFT) delineates the southernmost front of the wedge. It is assumed to form the most southern segment of the MHT and accommodates the majority of crustal shortening since at least the last ~2 Ma (e.g., Lave and Avouac, 2000; Powers et al., 1998). In its hanging wall the Sub-Himalayan fold-and-thrust belt is exposed and bounded to the north by Main Boundary Thrust (MBT) and the rocks of the Lesser Himalaya. These Lesser Himalayan rocks are moderate to non-metamorphosed, which are assumed to represent the former sedimentary cover units over the Indian basement, but have never been buried to greater depth (Jessup et al., 2015; Web et al., 2011; Hodges et al., 2000). Further to the north, the Main Central Thrust (MCT) separates the high-grade metamorphic Higher and Lesser Himalayan crystalline complex. Following up to the north, the prominent Zanskar shear zone represents a regional part of the southern Tibetan detachment system, juxtaposing the basal section of the Tethyan Himalayan strata (the Haimantas), over the high-grade High Himalayan Crystalline.

As the Indian plate submerges beneath the Himalayan wedge during its northward migration, about ~20 mm.a^{-1} of convergence is accommodated along the MHT basal décollement of the Central Himalaya from which other first order fault systems (MCT, MBT, MFT) divert as imbricate faults from it (e.g., Gao et al., 2016; Stevens and Avouac, 2015; Lavé, 2005; Lavé and Avouac, 2000; Hauck et al., 1998). Seismotectonic models for the Himalaya assume that all great earthquakes occur along this gently northward dipping detachment or along proposed mid-crustal ramp (Rajendra Prasad et al., 2011; Molnar, 1990; Ni Barazangi, 1984; Seeber and Armbruster, 1981). An observed 20-30 km wide transition zone between the seismically active detachment to the south and the aseismically slipping detachment zone to the north tends to concentrate low magnitude earthquakes (Mw 3-5) in a belt / cluster (Pandey et al., 1995) and has been referred as a ~20° dipping mid-crustal ramp in the MHT (Cattin and Avouac, 2000).

Diverting from classic topographic setting of central Himalaya, where the major physiographic transition is located between Lesser and Higher Himalaya, in the Kangra sector of the northwest Himalaya, the topography rises abruptly from the broad and low-lying Sub-Himalaya (< 1000 m a.s.l.) to a series of peaks forming the crest line of Dhauladhar Range ≥ 5000 m in altitude, and stays steadily high across Chamba region to the north. Two of the major Himalayan thrusts, the Main Boundary Thrust (MBT) and the Main Central Thrust (MCT) run unusually close to each other (< 4-5 km), along the base of this steep range front. Furthermore, the Higher Himalayan nappes are preserved near the orogenic front, and the exposure of the Lesser Himalayan is limited here to a narrow stretch of <4-5 km (see Fig. 5.1). The exposure of high-grade crystalline units, typical of classic central Himalayan setting are limited to the Kishtwar and Kullu-Rampur tectonic windows and located towards the northwest and east, respectively, of the study area (Figs. 5.1b and 5.2). In the study area between these tectonic windows, the weakly to moderately metamorphosed sedimentary cover rocks of the Haimanta Group are exposed and are preserved across Chamba. The Haimantas consist of a ~8 km thick, continuous, flysch sequence of late Precambrian to early Paleozoic age and are interpreted to be integral part of the Higher Himalayan nappes (e.g., Thakur, 1998; Frank et al., 1995; Fuchs and Linner, 1995; Griesbach,1891) and that can be correlated with the Phe Formation (Nanda and Singh, 1976) at the base of the Tethyan Himalaya in Zanskar (Dèzes et al., 1999; Frank et al., 1995). The structural style in Chamba is dominated by large anticlines and synclines with amplitudes of several kilometres and the exposure of the Lower Haimantas are restricted to the MCT hanging wall exposed along southern flanks of the Dhauladhar Range (Frank et al., 1995).

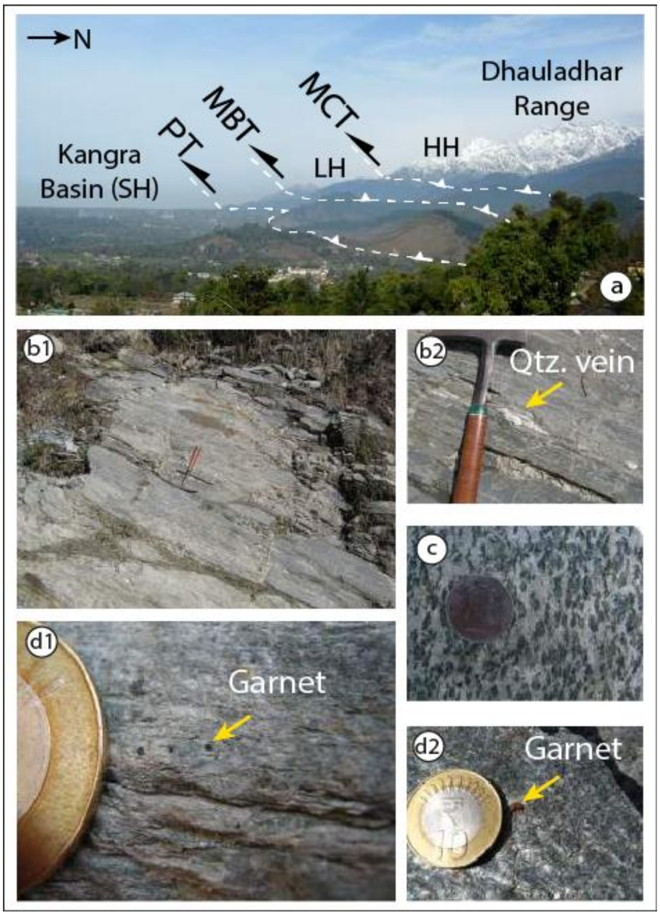

Figure 5.2*: Field photos of southern Dhauladhar Range front and typical rocks observed across MBT hanging wall. (a) Dhauladhar Rang to the north and Kangra Basin as part of the Sub Himalaya to south (looking west), dashed white lines denotes approximate exposure of the range bounding faults. Note the close extent between MBT and MCT. (b) Strongly deformed and sheared quartz veins in schists exposed in proximity of the MBT fault. (B2) is zoom in of B1. (c) Phyllitic schist close to the inactive MCT fault zone. (d) Garnet porphyroblasts in phyllitic schists of the MCT hanging wall.*

In contrast to the central Himalaya, where the MCT juxtaposes the high-grade Higher Himalayan crystalline (HHC) against low-grade Lesser Himalayan rocks, the MCT in Chamba (known locally as the Panjal Thrust) juxtaposes only ~1-2-km-thick high grade unit at the base of the Haimantas onto lower grade Lesser Himalaya (e.g., Yin, 2006; Thakur, 1998; Frank et al., 1995; Thakur and Rawat, 1992). This could be related to a ramp over which the MCT cuts laterally up-section between the central Himalaya and Chamba, or, conversely, the HHC in Chamba could form a southward-thinning wedge between the Tethyan Himalaya at the top and the Lesser Himalaya at the base, in which case the MCT would simply represent the original flat-over-flat relationship between the Tethyan and Lesser Himalaya when the High Himalayan was thrust over the Lesser Himalaya (Yin, 2006). Field observation along the Dhauladhar Range and in Chamba suggest that mylonites with foliations dipping ~35° and mineral lineations plunging ~20–35° to the NE in the basal MCT hanging wall (Thakur, 1998; Rautela and Thakur, 1992; own observations) suggest that this structure reaches the surface at similar high angles. Another notable difference of the NW

Himalaya with the classic central Himalaya is in the positions of small and moderate magnitude earthquake epicenters. In contrast to the Central Himalaya, microseismicity tends to concentrate in a narrow belt (Pandey et al., 1995), in NW Himalaya, there is a notable scatter in moderate seismicity over 80-km-wide region in the hanging wall of the MBT along the possibly flat-dipping MHT in the north of the Dhauladhar Range and further west (Gahalaut and Kundu, 2012).

Interestingly, our own field observations along southern flanks for the Dhauladhar Range, both north of McLeodganj and Palampur, we observed strongly sheared quartz veins in phyllites in proximity of the MBT hanging wall and very prominently-developed layer-parallel schistosity suggesting strongly sheared rocks under lower and moderate greenschist facies conditions (see Fig. 5.2B1, 5.2B2, 5.2C). Brittle fault planes and regional schistosity dip ~33-38° towards NE, providing hints about orientation of the fault movement. In addition, further up section at the base of the MCT hanging wall, we observed mm-sized garnet porphyroblasts in mica schists (Fig. 5.2D1, 5.2D2), just a few kilometer stratigraphically up section from the MBT, which we relate to early Miocene MCT activity.

5.3. Methods and results

5.3.1. Thermochronology

Combing our new ZHe with previously published ZHe and AFT cooling ages (Deeken et al., 2011) we obtain a densely sampled 80-km long range-perpendicular transects pattern in the hanging wall of the MBT. These ages are also in agreement with recently published AFT and Zircon Fission Track ages from the western flank of the Dhauladhar Range, about 50 km west of the study area (Adlakha et al., 2013).

With the Help of the thermokinmatic PECUBE-modelling, we are able to reconstruct the time-temperature pathway of exposed upper crustal rocks on their way to the surface. At higher temperatures, daughter isotopes of natural radioactive decay diffuse as an isotopic open system through the crystal lattice, until during cooling they reach a mineral decay specific threshold temperature range, where diffusion rates significant lowers and until its cessation is reached. When this happens the daughter isotopes get ‘locked’ within the crystal lattice and the system is isotopically closed and they are therefore preserved. For the ZHe this happens at temperatures of ~230 –200°C (Reiners and Brandon, 2006; Reiners et al., 2002) and for AFT at temperatures of ~ 130 –100°C, (Gleadow and Duddy, 1981) depending on cooling rate of rocks during their uplift. Combining information about the subsurface geometrical architecture of the most important fault system, timing of cooling of the rocks by thermochronologic constraints and thermal modelling gives us a opportunity to reconstruct the particle pathway within the orogenic wedge (Braun et al., 2012; Braun, 2002b; Ehlers, 2005; Mancktelow and Grasemann, 1997; Stuwe et al., 1994). We obtain a predicted cooling and exhumation history and regional distribution of predicted ages of the exposed rocks at the surface. The lowest misfits between the model-predicted and measured cooling ages help to explore best parameter combination suited for the area of interest. When rocks are moved over a fault ramp, the exhumed rocks are characterized by significant vertical component and the natural thermal field of the upper crust is strongly disturbed resulting in simultaneous vertical and lateral cooling (Huntington et al., 2007). For crustal temperature isotherms close to surface changes in relief/topography and can effect the crustal cooling pattern(Braun, 2002b). Applying 3D thermokinematic models, the effects of some of these parameters onto the evolution of the thermal field can be tested and quantified.

Previous publications (Adlakha et al., 2013; Deeken et al., 2011) provided key information about cooling history along base of the Dhauladhar range and had indications of a break in slope in the age-elevation relationship, however, these were based only on single data points. The previous studies were insufficient to answer if the exhumation along the toe of Dhauladhar range was deep seated and if exhumed rocks show signature of partial retention zone of ZHe or thermally fully reset Pliocene ZHe ages. Therefore we expanded the existing data set with seven new samples, collected at low elevation along the southern flank of the Dhauladhar Range, where Lesser and Higher Himalayan rocks in the hanging wall of the MBT and MCT are exposed. Standard mineral separation procedures were conducted at the University of Potsdam. All samples yielded high quantity of zircon phenocrysts. By handpicking, suitably sized (80-150 µm) pristine zircon grains were screened for large inclusions, cracks and their state of alteration using a binocular microscope magnification. The grain dimensions were measured for the calculation of the alpha-correction factor after Farley et al. (1996). Afterwards the single grains were packed in Nb-tubes for U-Th/He analysis and measured at the University of Tübingen using a Patterson Helium extraction line, which is equipped with a 960nm diode laser to extract the helium gas. After Helium analysis the grain packages was dissolved for U, Th, and Sm measurements using an ICP-MS (analytical procedure described in Stübner et al., 2016). At least three aliquot replicates per sample have been analyzed.

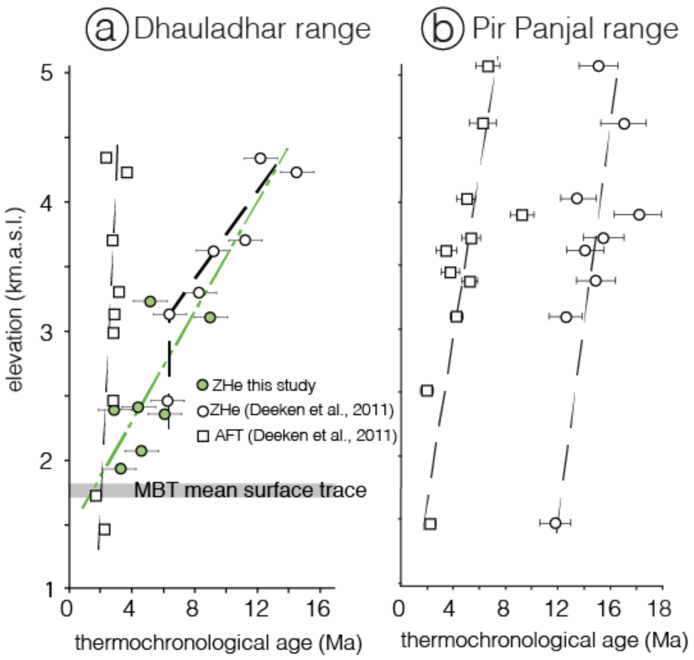

Figure 5.3: Updated age-elevation plot from Dhauladhar and Pir Panjal Range modified after Deeken et al., 2011. Green dote show newly obtained ZHe-ages. Note the difference of the age elevation trends of the two data sets. (A) AFT and ZHe data from the Dhauladhar Range, where AFT yield approximately the same age, despite large elevation difference and trend of ZHe is clearly different. (B) In contrast age-elevation trends of Pir Panjal Range run approximately parallel indicating constant but moderate exhumation rates.

The analytical error of the mass spectrometer measurements is generally very low and do not exceed 2%. In contrast, the reproducibility of the sample age constitutes a much larger error. We therefore report the mean U-Th/He age and the standard deviation of the measured aliquots as the sample error. For single grain ages, we apply a 3% 1-sigma-error-based on the reproducibility of standard measurements in the lab (Fig. 5.3; Table 5.1).

Table 5.1: U, Th, and He data from single grain zircons from southern flanks of the Dhauladhar Range, northwest India, Himalaya.

Sample	Grain count	Formation	rock type	Latitude (°)	Longitude	Altitude (m)	^{238}U (ppm)	^{232}Th (ppm)	eU	Th/U	^{4}He (mol) X 10^{-14}	blank (%)	He age (Ma)	Ft correction	Corrected He age (Ma)	Avg Age (Ma)	SD (Ma)	1σ (Ma)	ZHe ± 1σ (Ma)
RT13-33	5	Chail Fm.	Metagranite	32.16261	76.55833	2430	1565.0	205.3	1613.3	0.13	21.63	0.139	2.3	0.8	2.7	**3.0**	**0.3**	**0.2**	3.0±0.2
	6						1989.4	430.5	2090.6	0.22	59.61	0.050	2.8	0.9	3.3				
	9						1842.5	349.6	1924.6	0.19	22.14	0.179	2.3	0.8	2.9				
RT13-27	5	Chail Fm.	Metagranite	32.18478	76.55933	1955	1002.7	162.0	1040.8	0.17	26.68	0.110	3.4	0.8	4.1	**4.0**	**0.3**	**0.1**	4.0±0.4
	6						883.1	291.0	951.5	0.34	15.61	0.187	3.5	0.8	4.4				
	7						1000.5	86.0	1020.7	0.09	15.40	0.237	3.0	0.8	3.7				
	9						756.3	1291.7	1059.8	1.75	10.78	0.367	3.1	0.8	3.9				
RT12-37	4	Chail Fm.	Metagranite	32.1769	76.54966	1930	2564.6	205.1	2612.8	0.08	177.94	0.022	3.0	0.9	3.4	**3.4**	**0.5**	**0.2**	3.4±0.2
	6						1127.8	492.4	1243.5	0.45	26.49	0.138	2.3	0.8	2.7				
	7						1462.4	180.0	1504.7	0.13	21.54	0.133	2.7	0.8	3.4				
	8						1268.5	488.4	1383.3	0.39	39.42	0.074	2.8	0.9	3.2				
	10						1124.7	373.4	1212.5	0.34	26.85	0.109	3.4	0.8	4.1				
AD09-35	3	Haimantas	Grt-Micaschist	32.18047	76.68947	3110	388.7	102.6	412.8	0.27	8.81	0.324	6.8	0.8	9.0	**6.7**	**2.0**	**1.2**	6.7±1.2
	4						838.3	221.8	890.4	0.27	11.51	0.254	4.0	0.8	5.2				
	5						1024.4	274.5	1088.9	0.27	2.99	0.968	4.2	0.7	5.8				
AD09-38a	2	Chail Fm.	Metagranite	32.12808	76.67400	1920	769.6	356.5	853.3	0.48	8.80	0.449	4.6	0.8	6.1	**4.1**	**1.4**	**0.6**	4.1±0.6
	3						1292.0	231.1	1346.3	0.18	13.88	0.285	2.2	0.8	2.7				
	4						719.2	231.9	773.7	0.33	4.07	0.715	2.8	0.8	3.7				
	6						1370.0	191.4	1415.0	0.14	26.97	0.108	2.6	0.8	3.1				
	8						732.7	166.6	771.8	0.23	12.91	0.222	3.9	0.8	4.8				
RT12-38	1	Chail Fm.	Gneiss	32.16161	76.54948	1930	473.3	167.2	512.6	0.36	18.47	0.215	6.5	0.8	8.0	**5.1**	**2.5**	**1.5**	5.1±1.5
	3						2195.2	438.8	2298.3	0.21	12.39	0.320	3.2	0.8	4.2				
	2						2693.6	315.9	2767.8	0.12	14.47	0.274	2.5	0.8	3.2				
AD09-37	1	Haimantas	Metagranite	32.16124	76.69226	2411	974.1	187.9	1018.2	0.20	20.37	0.195	3.5	0.8	4.4	**6.1**	**1.9**	**1.1**	6.1±1.1
	2						1034.0	213.6	1084.2	0.21	68.02	0.058	6.9	0.8	8.2				
	3						1952.4	438.3	2055.4	0.23	57.34	0.069	4.5	0.8	5.7				

Chail /Shali Fm. Belongs to the Lesser Himalaya, Haimanta Gr. belongs to the Higher Himalaya

Table 5.1: U, Th and He data from the southern flank of the Dhauladhar Range with the mean ZHe ages with 1-σ uncertainty.

5.3.2. Model-setup for 3D-kinematic PECUBE modelling

To quantify the tectonic evolution of a region of interest, one needs to assess the parameter space of the thermo-kinematic properties to obtain the subsurface behavior of thermal field. With forward modelling, we evaluated the sensitivity and parameter space of single parameters, before we elaborated best combination of parameters using inverse modelling approach. Thereby the misfit between model-predicted and observed ages measures suitability of the model-parameter combination. Present day topography was inferred from the Shuttle Radar Topographic Mission (SRTM) 90 m digital elevation model (DEM) version 4.1. The kinematic model incorporates the MHT as NNE-dipping low-angle detachment and the MFT and MBT as NNE-dipping high-angle fault ramps (Fig.5.4). We took advantage of some published rock thermal diffusivity measurement presented in (Thiede et al., 2009) and inferred for all other physical parameters of the rocks within geologically meaningful ranges. For more details, please see the data repository (Fig. S5.2-S5.5).

For the forward runs, the thermal diffusivity lays between 28 and 60 km²/ Myr. The mean surface temperature and the atmospheric lapse rate were set to 6°C and 6°C/km, respectively. The heat production varied between 0 °C/Myr and 40 °C/Myr. The basal temperature also varied between 600°C and 1000°C. Fault slip rates was inferred from present day GPS-derived convergence rates (Stevens and Avouac, 2015; Schiffman et al., 2013) and corrected to strike-perpendicular convergence rate of the Dhauladhar Range, which runs 115° ESE. We split the total convergence rate of 14 mm.a^{-1} into the three faults. In particular, we set the Indian under-thrusting rate along MHT to a constant value of 5 mm.a^{-1} for the duration of the model runs, while the remaining 9 mm.a^{-1} are split between MBT and MFT. We deduced the following temporal constraints from fault activity in the models as following: ZHe ages from high elevations (>3000 m) obtained both from Dhauladhar and Pir-Panjal range between 18-12 Ma with considerable scatter (Fig.5.3), and therefore have been related to post tectonic slow exhumation, potentially through the partial retention zone, after the MCT-activity terminated in Middle Miocene. Based on independent geologic constraints, it is assumed, that activity along the MBT was established between ~9 Ma to ~11 Ma (Thakur, 2014; DeCelles 2001; Meigs, 1995). Hence, we assumed 10 Ma as a certain minimum onset time for the MBT. Nevertheless, the model runs start at 18 Ma to allow the thermal field to relax from any previous disturbance. For example, the MBT activity was assumed 0 mm/yr at 18 Ma (no activity) and 1-4 mm/yr (full activity) between 10 Ma and 0 Ma.

5.3.2.1. Forward model runs

Within the first series of forward model runs we evaluated different structural settings of classic subsurface fault geometries models of the Himalaya wedge for their plausibility. While the first geometry (Fig. 5.4) comprises a relatively simple MFT-MBT-MHT relation, all other initial models (see the Data Repository for details) encompass more complex subsurface fault geometries. Only geometry I (Fig. 5.4) is able to predict cooling age pattern similar to observed once. Fault geometries II, III, and IV (in Appendix 3) are able explain the observed cooling age pattern across the Dhauladhar Range. We test various fault parameters and geometry such as (a) the MBT fault slip rate (1 - 4 mm/yr), (b) dip angle of the MBT-fault ramp (20-60°) and (c) basal temperature. Lowest mismatch between predicted and observed ages was found with this following combination: 2 - 3 mm.a^{-1} slip rate on MBT-ramp, 40 - 45° dip of MBT-ramp and basal temperatures of the model 750°C to 800°C.

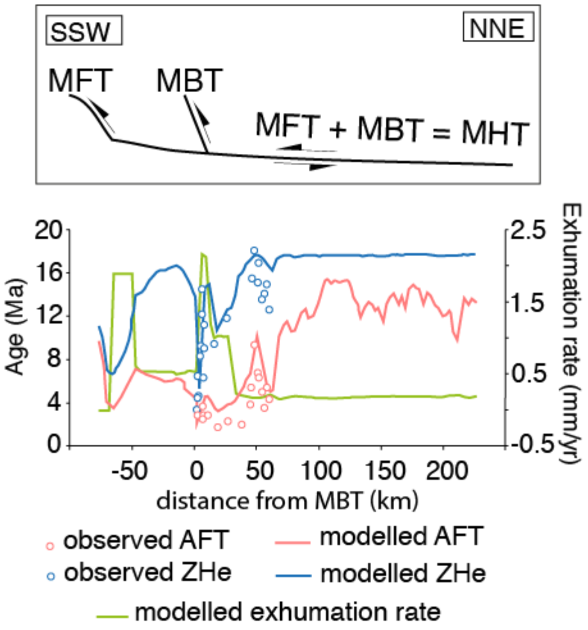

***Figure 5.4**: Model (I) of fault geometry below the Dhauladhar Range and forward model runs comparing observed and model predicted cooling ages with respect to fault geometry setting. Alternative fault geometry models are presented in the data repository. Arrows indicate the kinematic of the faults. Note that dotes represent projected and measured data points, while lines show the predicted mean age over the full width (50 km) at sample location. The green line represents the predicted mean exhumation with respect to the MBT. Abbreviations as in Fig. 5.1.*

5.3.2.2. Inverse model runs

As the next step we performed inverse modeling, following the methods presented in Robert et al. (2011). We built a multidimensional parameter space consists of 5 free parameters and found that 3 km grid-cell-resolution worked best for the area. These parameters are (1) the basal temperature (600 - 1200°C), (2) the slip rates on the MBT and (3) MFT (1 - 3 mm/yr and 8 - 6 mm/yr, respectively), (4) the internal heat production (0 - 45 °C/Myr) and (5) the thermal diffusivity (25 - 60 km²/Myr). Fig. 5.5 shows the obtained results from inversion modelling. For the thermal diffusivity, the lowest misfit values range between 46 and 50 km²/Myr, indicating a low sensitivity of that material constant on the cell size. In contrast, the internal heat production scatters most between 3 and 30 °C/Myr. The constant temperature at 25 km depth varies between 625 and 662 °C, yielding model wide geothermal gradients from 25 °C/km to 26.3 °C/km, respectively. These values represent a crustal mean arise from the medium crustal depth of the model and the position at the very orogenic front, where a cold underthrusting Indian basement influences the thermal field. In summary, the parameters suggest the following: (a) rock averages physical parameters can be applied, (b) the MBT fault ramp must be deep-seated to obtain Pliocene reset ZHE ages in hanging wall and extend ~30-40 km to the north to obtain reset AFT cooling of <3 Ma across the entire Dhauladhar range, independent of strong variations in elevation.

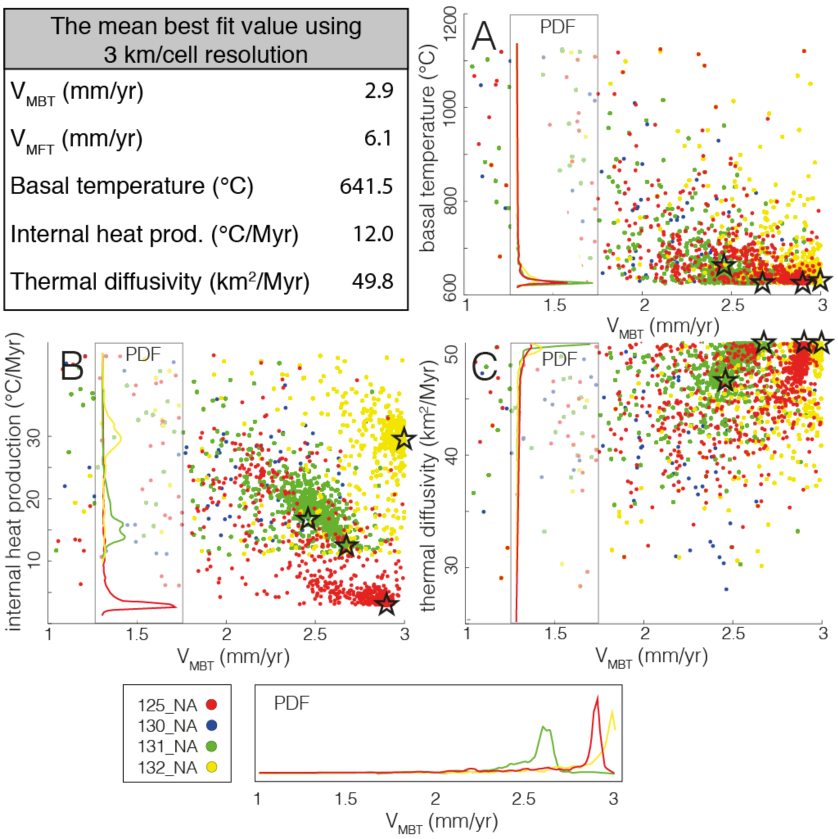

The mean best fit value using 3 km/cell resolution	
V_{MBT} (mm/yr)	2.9
V_{MFT} (mm/yr)	6.1
Basal temperature (°C)	641.5
Internal heat prod. (°C/Myr)	12.0
Thermal diffusivity (km²/Myr)	49.8

Figure 5.5: Examples of the results of the inverse model runs together with their parameter space PDF's. The color coding stands for the misfit value of each model. Black stars denote the best fit parameter combination. Overall model dataset, calculated with 3km-cellsize (125_NA, 131_NA) and 1 km cell-size (130_NA, 132_NA), proving observation by Valla et al. (2011) .

5.3.3. Evaluation of the sensitivity of model ages with respect to topography and different MBT-onset times

Obtained from earlier inversion modeling results, we used a mean of the best fit parameters (see Table 5.2) to investigate effect of denudation-induced topographic amplification onto the predicted model ages and test potential effect of variable fault activity scenarios of the MBT (see Appendix 3; Fig. S5.6, onset variation), such as we varied the MBT-onset time between 2 and 14 Ma. Using varying sensitivity test we explored effects on thermal cooling of four possible “topography - fault - onset scenarios”- scenarios A, B, C and D.

1) In scenario (A) the effect of varying temporal constraints for onset of the MBT activity and topography. Here a pre-existing topography is assumed at the time, when the MBT became active. This pre-existing topography results from shortening across the MCT and built up prior to 15 Ma. At the time when the MBT became active, the topography was assumed be already 100% of the modern topography.

2) In scenario (B) we study of abrupt onset MBT-fault and rapid topographic growth onto the predicted model ages. In the different sub-scenarios MBT-faulting starts abruptly faulting at a certain point, where also the topography grows to 100% suddenly from prior assumed no-topography setting.

3) Throughout scenario (C), the topographic evolution is decoupled from onset of faulting, assuming topography (100%) remained constant and equal to the modern topography during the whole model run.

4) The last scenario (D) comprises a relief growth, which accounts for the interior part (Pir Panjal Range) of the model, where relief growth should decrease due to effective shielding by reasons such as a rising range front.

In summary, all these model runs indicate that a minimum activity of 8 Ma is necessary, to reproduce the observed cooling age pattern, except for scenario 3, were it is achieved after 6 Myr already. This value seems to be the response time to establish the needed thermal field perturbation. This is in good agreement with previous findings (Deeken et al., 2011). Despite the generally younger ages in scenarios 3 and 4, a time invariant behavior of the model- predicted ages, referred as to be close to exhumational steady state (Willet and Brandon, 2002) could have evolved after 8 Ma of fault activity. Model scenarios A and B yield to old ZHe ages, indicating that high topography was probably established prior to MBT activity.

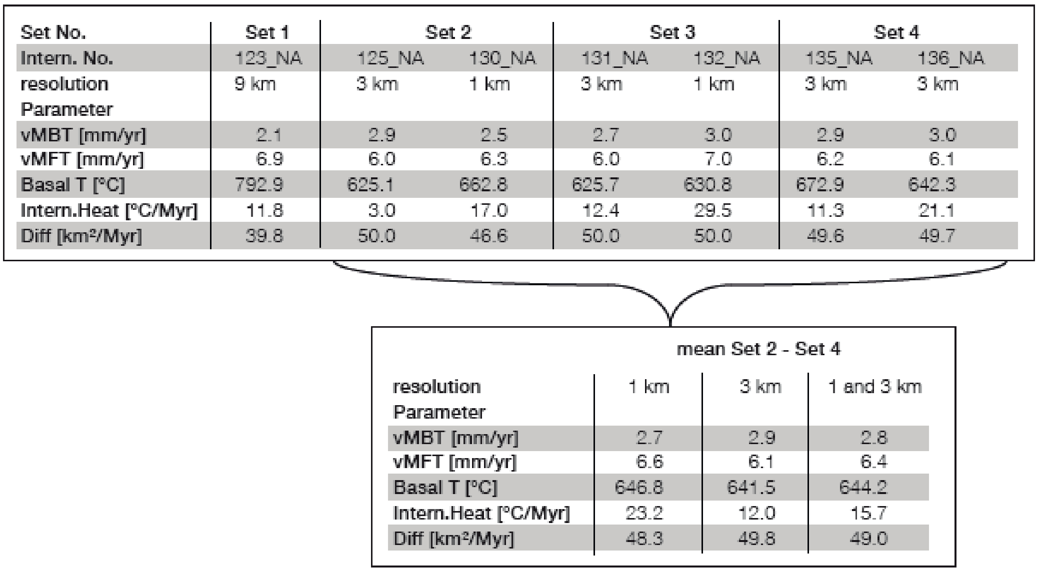

Set No.	Set 1	Set 2		Set 3		Set 4	
Intern. No.	123_NA	125_NA	130_NA	131_NA	132_NA	135_NA	136_NA
resolution	9 km	3 km	1 km	3 km	1 km	3 km	3 km
Parameter							
vMBT [mm/yr]	2.1	2.9	2.5	2.7	3.0	2.9	3.0
vMFT [mm/yr]	6.9	6.0	6.3	6.0	7.0	6.2	6.1
Basal T [°C]	792.9	625.1	662.8	625.7	630.8	672.9	642.3
Intern.Heat [°C/Myr]	11.8	3.0	17.0	12.4	29.5	11.3	21.1
Diff [km²/Myr]	39.8	50.0	46.6	50.0	50.0	49.6	49.7

	mean Set 2 - Set 4		
resolution	1 km	3 km	1 and 3 km
Parameter			
vMBT [mm/yr]	2.7	2.9	2.8
vMFT [mm/yr]	6.6	6.1	6.4
Basal T [°C]	646.8	641.5	644.2
Intern.Heat [°C/Myr]	23.2	12.0	15.7
Diff [km²/Myr]	48.3	49.8	49.0

Table 5.1: *Results of inversion modelling in PECUBE. The upper table denotes the results from all inversion attempts and the lower table shows the mean best fit values of the different model parameters and different resolutions. The mean of the 3 km/cell model has been used for examining the different MBT-onset timings.*

5.4. Discussion

We combined our field observations, structural information, and new and previously published thermochronology data in order to test possibly active ongoing faulting and deep-seated rock exhumation of the MBT hanging wall along the Dhauladhar range. This is strikingly different from most other transects through the MBT along-strike of the Himalaya. By combining topographic, structural, and rock cooling patterns as input parameters for 3D thermokinematic modeling, we were able to obtain information (a) on the timing of faulting and rates of exhumation, (b) important implications on the extent of the MBT fault ramp (Fig. 5.1b), and (c) on the structural architecture of the fault geometry below the Dhauladhar range front, as well as of the adjacent orogen interior.

The obtained AFT and ZHe age transects encompass the main orographic barriers, the Dhauladhar and Pir Panjal ranges, but their cooling patterns across the two ranges show systematic differences (Fig. 5.3). All AFT samples (n = 10) across the Dhauladhar range yielded young cooling ages ranging between 1.7±0.3 and 3.7±0.4 Ma, despite strong differences in sample elevations ($\Delta Z = 2.8$ km). Furthermore, the AFT ages appear to be elevation-invariant up to a distance of ~40 km north of the MBT, which suggests a high vertical rock uplift component and a strong perturbation of its closure isotherms. In this case, it is running approximately parallel to the first-order topography (Ehlers, 2005; Braun, 2002a). This scenario implies that all of the samples required approximately the same amount of time to pass the closure isotherm and approach the surface, independent of their sample elevations. Such a perturbation of the thermal field strongly implies a ~40 km-long and deep-seated MBT fault ramp beneath the Dhauladhar range (Fig. 5.1b), which would have forced the rocks to uplift and cool rapidly. It seems that the topographic wavelength of the Dhauladhar range exceeds the critical wavelength of the AFT isotherm (Braun, 2002a). In contrast, AFT ages (n = 9) across the Pir Panjal range in the orogen interior yielded older ages and showed much larger scatter (Fig. 5.1b). More specifically, they ranged between 3.5±0.8 and 9.3±0.9 Ma and indicated some degree of elevation dependency (Fig. 5.3). Overall, these ages indicated continuous but significantly lower exhumation rates across the Pir Panjal range than across the Dhauladhar range when passing the AFT closure isotherm range, which has already been described in Deeken et al., 2011.

Our field observations, which described the exposure of greenschist metamorphic rocks in the hanging wall of the MBT versus unmetamorphosed rock in the footwall, documented approximately ~20–35 km of fault displacement accommodated along this fault zone within this segment of the Himalayan wedge. In the footwall of the MBT, rocks related to the Subathu and Dharamsala Formations are bounded by faults known as the Palampur thrust, and run approximately parallel to the MBT strike (Fig. 5.2) (Powers et al., 1998; Ranga Rao, 1988). However, these rocks are only slightly deformed, show no metamorphic overprinting, and thrust over the younger Siwalik strata. We interpreted this to mean that the MBT fault ramp forms the main range-bounding fault zone exposed along the toe of the frontal range, which has maintained a high crest line with peaks exceeding 5000 m a.s.l. at present. This is in clear contrast to observations made by Najman et al. (2009), who described that the MBT hanging wall at the eastern end of the Kangra re-entrant consists of non–metamorphosed rocks and illustrates significant lateral variation in mean fault displacement and exhumation along the MBT hanging wall. Their findings were consistent with many other MBT segments along-strike of the orogen (DeCelles et al., 2001; Hodges, 2000). In summary, these field observations strongly suggest that only significant fault displacement could explain the change in metamorphic grade observed across the MBT fault zone, and therefore only the MBT could have acted as the first-order fault zone accommodating the majority of the displacement. The ZHe ages (n = 16) across the Dhauladhar and Pir Panjal ranges both show some scattered age-elevation relationships (Fig. 5.3) and systematic younger ages along the toe of the Dhauladhar range. However, the northern flank of the frontal range is characterized by AFT and ZHe ages ranging between 2.9±0.3 and 9.2±0.9 Ma and 9.4±0.9 and 14.5±1.5 Ma, respectively (Fig. 1b). These differences were previously accredited to oblique heat advection resulting from the southward-directed thrust motion on the MHT or MBT fault ramp (Deeken et al., 2011).

Previous studies using constraints from abrupt changes in the sedimentary records of the Sivaliks with the Kangra re-entrant suggested an onset of MBT fault activity between 8 and 10 Ma ago (Brozovic and Burbank, 2000; Meigs et al., 1995). They also implied that the rocks yielding ZHe ages < 10 Ma have at least partially or fully reset since the onset of MBT activity and are only documenting the onset of the recent deformation of the Himalayan range front in this segment. Previous studies already showed that both the thermochronometers across the Pir Panjal range recognize an age-elevation relationship (Fig.5.1b). Their trends run approximately parallel, indicating no significant changes in exhumation rates within the confines of the data resolution (Deeken et al., 2011). Overall, these results imply slower exhumation related to sub-horizontal fault displacement along a flat-dipping MHT below the Pir Panjal range, causing slow cooling and a long transition through the ZHe partial retention and AFT annealing zones. This also probably explains some of the observed data scatter (Deeken et al., 2011). The high elevated (>3.7 km a.s.l.) ZHe ages (>10 Ma) across the Dhauladhar and Pir Panjal ranges (Fig. 5.3a) have been interpreted to imply late cooling related to the MCT fault active until the mid-Miocene, which has stayed above closure temperature since that time.

Several structural fault geometries of the Himalayan wedge were tested with forward thermal model runs for the studied segment of the Northwest Indian Himalaya. Only one of the tested scenarios — an imbricated MBT fault ramp rooted to the MHT — could explain the observed cooling pattern derived from the low-temperature thermochronology data (geometry I) (Fig. 5.4). Neither a 'flat-ramp' geometry nor a duplex beneath the Pir Panjal range would be sufficient to reproduce the observed cooling age pattern (Appendix 3; Fig. S5. 2). The exhumation rates obtained from such geometries would be too high and yield too-young model surface ages, which would not correlate with the cooling age pattern measured across the Dhauladhar range. This is also supported by the regional scatter of smaller-magnitude earthquakes (M<5) from the ISC catalog and from local networks run by the India Metrological Department (IMD) (Gahalaut and Kundu, 2012) that indicate an absence of any mid-crustal ramp along the MHT within this segment, unlike in other Himalayan segments further east. This suggests that the MHT décollement dips with a uniform trend of ~3–5° to the NE, and has not formed a ramp structure beneath the Dhauladhar range. Furthermore, we used another set of forward models to test deviant MBT dip angles (see Appendix 3, fig. S5.3a, S5.3b) and discovered that a dip of 30 to 40° (MBT ramp) yielded the lowest misfit between the observed and the modeled ages. Nevertheless, a steeper MBT fault ramp would result in a rapid exhumation zone with a narrower width. Only the mentioned ideal range of angles would be able to reproduce the observed range front cooling pattern with lowest misfit. A similar dip of the MBT has been reported by Adlakha et al. (2013) for the Dalhousie region, 50 km west of our working area. In contrast, a study conducted on the Central Nepal segment by DeCelles et al. (2001) inferred a ~10° dip of the MBT as the frontal ramp continues for about 50 km to the north and merges with the MHT décollement at a depth of ~8 km.

The Dhauladhar range's spatial confinement and present altitudes are the result of the angulated slip on the MBT fault ramp. When combined with the aforesaid assumption about the structural information derived from the thermochronometric dating, it can be deduced that the minimum fault displacement on the frontal fault is in the range of 25 to 30 km. Our detailed inverse model runs suggested uniform slip rates of about 2.5 to 3 mm.a^{-1} on the MBT (Fig. 5.5, table 5.2). However, these slip rates merely account for the combination with the other tested best-fit parameters; an even higher range could be expected due to the large displacement. Our inverse modeling yielded a basal temperature between 625 and 672°C at a crustal depth of 25 km, which led to overall thermal gradients of 25–27°C/km. At the point in depth where the MBT merges with the décollement, this thermal gradient would result in a temperature slightly above 300°C. The inferred lower greenschist facies conditions derived from the mineral assemblages observed in the field (Fig. 5.2) presume a temperature of 300–450°C temperature and a pressure level of 1–4 kbar. This corresponds to a depth lower than 15 kilometers and therefore fits with the assumed structural architecture. As previously mentioned, other geometries would exhume material from a greater depth, resulting in increased metamorphic facies, which have only been observed north of the Pir Panjal (Deeken et al., 2011), where uplift across the Gianbul dome comprises different fault relations and thermal regimes. The observed garnet growth in the field (Fig. 5. 2D) implies temperatures of > 400°C and did not fit with our modeling. However, several possibilities could explain the existence of the garnets. They could have grown in more pronounced p-T-conditions at deeper depths and could therefore have been initially transported southward along the décollement, then have been uplifted over the MBT ramp. Alternatively, the temperature conditions could have been higher, but then the overall thermal system could have been cooled down by the old and cold crust of the subducting Indian slab. After surpassing the MHT, the material could then have been thrusted southward into its recent position. The fact that we found these garnets so close to the MCT fault zone could also hint that Higher Himalayan material was transported by the MCT from a deep interior source during the early to midMiocene. In summary, the inverse model runs confirmed the previously mentioned assumption derived from thermochronometric dating, which clearly showed intense and long-lasting frontal exhumation above a steep frontal MBT fault ramp.

We also tested the sensitivity of the models to different MBT initiation timings (Supplementary Fig. S5.6). These models showed that a minimum activity for the MBT of at least 6 Myr would have been necessary to reproduce the observed cooling age pattern. At least 8–10 Myr would have been needed to establish a time-invariant pattern. Such a pattern evolves if the exhumation is in a near-steady state (Willet and Brandon, 2002). Our model results therefore confirm the sedimentary constraints presented by Meigs et al., 1995 as well as Brozovic and Burbank, 2000. The Dhauladhar range therefore could have nearly achieved an exhumational steady state for at least the last couple of million years. The most realistic exhumation behavior is thereby obtained when the topographic evolution slows down after the frontal range reaches a certain threshold elevation where fault motion and rock uplift are balanced by deep-seated erosion and exhumation across the entire Dhauladhar range (Appendix 3; Figure S5.6d). Assuming that the local climate pattern has been approximately consistent since the Dhauladhar range was established, the first-order orographic barrier was formed ~10 Ma ago. A possible climatic feedback between fast erosion and denudation-induced unloading and rock uplift, which helped maintain the steep southern flanks of the Dhauladhar range, would explain the fast modeled exhumation rates and the localization of the deformation over a 10 Myr time frame, which is rather unusual compared to other MBT segments along the entire Himalaya, but which confirms the earlier findings of Deeken et al., 2011.

In summary, our study highlighted the complex relationship between morphology, underlying structural architecture, and thermochronometric systems. It also emphasized the Dhauladhar range's significance as a structurally unique range front segment among the along-strike Himalayan fault segments. The local exhumation history is strongly interconnected with the underlying structural architecture and dates back to at least 6 Ma, if not the last 8–10 Myr. This segment probably accommodated about 2–3 mm.a^{-1} of crustal shorting over the last 10 Ma, which has not been recognized in estimates made across this segment of the Himalayan wedge by previous researchers, who tend to assert that the Sub-Himalaya has accommodated the total Himalayan crustal shortening since 2 Ma.

5.5. Conclusions

Combining the new ZHe and AFT cooling ages from this study with those from Deeken et al., 2011 and the 3D thermokinematic inversion modeling of the Dhauladhar range provided key information about the exhumational history of the range front since the mid-Miocene as well as the structural pattern of the orogenic wedge in this sector of the Himalaya.

The MBT bordering the Dhauladhar range on its southern flank forms a deep-seated fault ramp, along which 8–10 km of rock exhumation since the mid-Miocene can be inferred from the observed low-temperature thermochronologic ages (assuming a mean geothermal gradient). Our modeling results suggest that the documented ZHe and AFT cooling ages could only be obtained if there has been a slip rate of ~2–3 $mm.a^{-1}$ on the MBT fault ramp since its activation. This means that, over a longer timescale (several Myr), the MBT accommodated nearly 10–15% of the crustal shortening (~2 $mm.a^{-1}$) in this sector of the Himalaya. This finding contradicts previous studies (Thakur et al., 2014; Powers et al., 1998), which claim that all of the crustal shortening in the Himalaya has been solely accommodated within the Sub-Himalaya over the last 2 Ma.

This study also suggests significant changes in the structure of the Himalayan orogenic wedge. The observed and modeled exhumation pattern suggests that there is probably no mid-crustal ramp or duplexing of the Lesser Himalayan sequence beneath the Dhauladhar range, as the observed cooling age pattern would only possible if the exhumation occurred along a steeply-dipping fault ramp soled directly into the gently-dipping MHT décollement. The absence of these tectonic features supports the idea of along-strike variation of the sub-surface geometry of the Himalayan wedge, as the Dhauladhar range exhibits a strikingly dissimilar structural pattern to the more frequently studied Kullu-Rampur window, the nearby Kishtwar Window and even the Central Nepal Himalaya. However, the maintenance of pronounced topographic mountain front of Dhauladhar Range support strong feedback tectonic uplift and erosion, as our previous study suggested (Deeken et al., 2011).

Acknowledgements

This study was funded by Deutsche Forschungsgemeinschaft (DFG) grants to R. Thiede (TH 1371/5-1) and DAAD-DST (PPP-India # 57035520) to R. Thiede and V. Jain. We acknowledge the collaboration and logistic support provided by V. Jain and group (IIT Gandhinagar, India). We obtained further support for J. Faruhn and S. Dey from the Graduate School DFG-GRK 1364 to M. Strecker (STR 373/19-2). We also thank T. Ehlers for collaboration and ZHe-dating support at the University of Tubingen and P. van der Beek for hosting R. Thiede at ISTerre, University of Grenoble. France.

Chapter 6: Discussion and conclusions

The findings of the studies presented in this thesis address the key research questions on the impact of tectonic-climactic interaction on the evolution of certain mountain belts. The primary objectives of Chapter 3 and Chapter 4 were to understand the effects of tectonic and climatic forcing on sediment delivery out of the active Himalayan orogen over 10^3-10^5-year timescales and to assess if these factors have significant feedback on each other. Meanwhile, Chapter 5 deals with the assessment of tectonic activity of the Main Boundary Thrust over a Myr (10^6) timescale.

I have examined a case study from the Kangra re-entrant in the Northwest Himalaya. The Kangra re-entrant exposes the ~80 km-wide Sub-Himalayan fold-thrust belt. Ongoing crustal shortening accommodated by slip on several arc-parallel Sub-Himalayan thrusts have created a few intermontane piggyback basins within the re-entrant. The Kangra Basin (~700-< 1000 m asl) is one of these basins, formed in the hanging wall of the NW-SE-striking Jwalamukhi Thrust. Shortening accommodated along the Jwalamukhi Thrust created this basin on its hanging wall and provided the accommodation space for the transient storage of foreland-bound sediments originating from the Dhauladhar range, encompassing the Lesser and Higher Himalayan rocks. Preserved alluvial fills and several levels of fluvial terraces in and around the Kangra Basin and well-constrained catchment area provide an excellent opportunity to study the variations in sediment transport out of the Main Himalayan orogen. Sedimentary records of more than 200 m of valley fill in the past in the basin also adds to the novelty of this study area, as this level of valley fill has never been reported before from any sediment archive from the Himalayan mountain front. To achieve temporal constraints over fluvial incision, I performed surface-exposure dating of the fluvial terraces and alluvial fan tops using in-situ cosmogenic nuclide (^{10}Be). By combining OSL-IRSL ages from previous studies by Srivastava et al. (2009) and Thakur et al. (2014) with the new exposure age results, I was able to constrain the episodic depositional and erosional phases observed in the Kangra Basin. The intermontane Kangra Basin hosts late Pleistocene-Holocene basin-fill sediments, in which at least six different fluvial terrace levels have been formed over the last ~60 ka. Field evidence suggests that the sediment aggradation in the basin can be largely divided into two basin-fill phases (AF1 > 80-60 ka and AF2 ~15-11 ka) with some minor re-aggradation phases (~32-28 ka and 22-18 ka). Surface-exposure dating with in-situ ^{10}Be suggests the terraces (T1-T6) were formed at ~53±5, 17±2, 10±0.9, 7.8±0.7, 5.7±0.4, and 3.3±0.3 ka, respectively, at successively lower elevations from the riverbed. While T1 and T2 were sculpted into the AF1 fill, the latest of the aggradation periods (AF2) was succeeded by episodic re-incision and terrace abandonment, creating at least four terrace levels (T3-T6) during the Holocene, the oldest and best-preserved of which (T3) was formed at 10.1±0.9 ka.

The other significant feature in the study area is the Dhauladhar range, which exposes the MBT and the MCT on the southern flank and creates a sharp topographic contrast with the Kangra Basin on the footwall of the MBT. Highly deformed sheared rocks on the MBT hanging wall suggest the exhumation of these rocks from a greater depth and provide the opportunity to evaluate the activity of the MBT as well as the structural pattern of the Himalayan orogenic wedge in this segment. I worked with the group of scientists on the study focusing on slip on the MBT fault ramp since at least the mid-Miocene and assessing the structural pattern of the MBT-MHT décollement with the help of low-temperature thermochronology and 3D thermokinematic modeling (PECUBE). The compilation of newly-obtained ZHe and AFT ages along with previously-published ages from Deeken et al., (2011) and inversion modeling based on five different model parameters suggests that the lowest misfit between the observed cooling age pattern and the model-derived cooling age pattern would require ~2-3 mm.a^{-1} slip on the MBT fault ramp since at least 10 Ma. This in turn suggests that the MBT in this segment of the Himalayan mountain front has been active over a longer timescale and has accommodated ~2 mm.a^{-1} crustal shortening since its activation.

6.1. Effect of climatic forcing on sediment cycle

Variability in monsoonal strength, as well as glacial-interglacial periods has been suggested to influence sediment flux in the Himalaya (Bookhagen et al. 2005; Wulf et al., 2010; Dortch et al., 2013). Climatic changes related to both ISM oscillations and glacial-interglacial cycles are documented in speleothem oxygen-isotope ($\delta^{18}O$) records from Dongge cave, China (Dykoski et al., 2005), the Shillong Plateau of NE India (Dutt et al., 2015), and the Hulu and Sanbao caves, southeast China (Wang et al., 2008). The isotope trends match well with one another, supporting continent-wide, synchronous trends at 10^3-10^4-year timescales. $\delta^{18}O$ records are typically assumed to be inversely proportional to rainfall in the Himalaya, as intensified monsoon circulation and associated convection leads to depletion of the lighter isotope, resulting in lower $\delta^{18}O$ values. In this thesis I showcase how these climate trends can be potentially linked to the depositional and erosional phases observed in the study area. Such links have been proposed for other areas, but have not been rigorously tested with detailed chronologic data.

AF1 alluvial-fan remnants represent the oldest preserved upper Pleistocene fill in the Kangra Basin. IRSL ages of intercalated loess/paleosol levels located in the upper third of the basin fills in the Kangra area (Srivastava et al., 2009) suggest that AF1 aggradation probably started prior to 78.7±17.7 ka. Our exposure ages of terrace remnants yielding ages between 53±3 (depth profile T1-P1) and 43±3 ka (depth profile T1-P2) support these earlier inferences that basinwide net aggradation had ended by ~53 ka. The difference in our exposure ages for terrace level T1, combined with the different sediment layers exposed in the sampling pits and IRSL-dated loess deposits (Srivastava et al., 2009), suggest at least one minor aggradation phase between ~53 and 43 ka. The ~53 ka pit exposes the older, weathered aggradational unit (AF1a) and the exposure age marks the onset of 'T1a' incision. The less weathered unit exposed in the ~43 ka pit refers to the later, short aggradation phase as 'AF1b', which was terminated by the 'T1b' incision phase. T1a incision, which marks the onset of incision into the oldest-preserved basin fill, commences after the transition from the drier MIS4 to the wetter MIS3. Stronger monsoon phases with more precipitation would lead to a higher transport capacity and higher incision potential, leading to incision of the AF1a fill. However, incision could be counteracted by an increased sediment flux from the hillslopes. We are unsure of the sediment flux at that time, however, the low basin-wide denudation rates suggest that near the end of AF1a aggradation, the sediment flux could have decreased, thus resulting in incision during a time of overall wetter conditions. In addition, it may be hypothesized that during such a humid phase vegetation cover in higher and drier areas eventually stabilized the landscape and counteracted the removal of hillslope material, thus leading to incision of the main stem. The less-weathered, 'fresh' sediments of the AF1b fill suggest an absence of reworked material and instead a source from the high-elevation sectors of the Dhauladhar Range. Between 55 and 42 ka, stable-isotope trends suggest an overall slight decrease in monsoon intensity with a few short-term excursions toward higher precipitation. Although the minor aggradation event (AF1b) could be associated with one of these short-term events, the available data is insufficiently precise to resolve any clear link. Nonetheless, the alternations between incision and aggradation during MIS3 with no substantial net aggradation or net incision is likely associated with these short-term variations in monsoon intensity.

Following the formation of T1b (~43 ka), significant sediment removal (including ~80-100 m of river incision) occurred throughout the Kangra Basin until the end of the LGM. However, this substantial net incision was interrupted by two short-lived aggradation events from ~32-28 ka (AF1c) and ~22-18 ka (AF1d), as indicated by previously published OSL data and their stratigraphic relationships (Thakur et al., 2014). Because fill AF1d sits at a lower elevation than AF1c (Thakur et al., 2014), incision of >25 m must have occurred in between the two minor aggradation phases. Interestingly, significant LGM aggradation has been observed primarily in large drainage basins draining the High Himalaya, but has not been recognized along the foothills of the Dhauladhar range, which might be related to the limited glacial cover along its steep southern flanks. The first (Af1c) aggradation phase started at the beginning of the LGM during a brief period of increased monsoon intensity (Fig. 3.5), indicating that an increased sediment flux was more important than an increased fluvial transport capacity for the fluvial response. The end of that phase has no terrace record preserved. Between AF1c and AF1d aggradation, δ^{18}O data from NE India (Dutt et al., 2015) show a few variations between low and high intensities of the ISM within an overall weakening trend. Incision during a time of decreased precipitation must result from a decreased sediment flux. The second (AF1d) aggradation episode was during the latter half of the LGM. This aggradation was possibly related to the growth of Himalayan glaciers and lowering of the periglacial frost-cracking and solifluction zone, causing an increased sediment flux, together with a lower fluvial transport capacity associated with the relatively weak ISM (e.g., Scherler et al., 2015). A pulse of greatly increased sediment flux might have occurred when glaciers rapidly retreated (Dortch et al., 2013; Eugster et al., 2016), and large quantities of sediment stored as moraines in the Higher or Lesser Himalayan valleys were delivered to the fluvial network (resulting in AF1d aggradation), as previous studies recognized (Densmore et al., 2015; Dortch et al., 2013). However, the AF1d aggradation in the Kangra Basin is not volumetrically extensive.

Our ^{10}Be-exposure ages illustrate that the AF1d aggradation phase was followed shortly by incision of the alluvial deposits and formation of T2 terrace ~16±2 ka. T2 incision phase corresponds to a very weakened ISM towards the end of the LGM (18-15 ka). During this period (the end of MIS2), the fluvial transport capacity may have been low (if glacial melt water is insignificant), in which case incision can only be explained if the sediment flux was even lower. Another interpretation for this T2 incision phase is that post-LGM glacial retreat had supplied high discharge due to glacial melt water even during the relatively weak monsoon, while the sediment supply was reduced as hillslope erosion, periglacial activity, and mobilization of transiently-stored sediment were minimal.

The Indian Summer Monsoon strengthened rapidly after ~15ka, with a short interruption during the Younger Drayas (14-12 ka). It stayed relatively strong until ~6 ka (Dutt et al., 2015; Dykoski et al., 2005). The climate signal shows that the ISM had significant weaker periods within this overall strong monsoon phase. There is widespread evidence that the ~15 to 10 ka period correlates with rapid sediment aggradation in the Lesser Himalaya and High Himalayan domains along the Sutlej valley (Bookhagen et al., 2006) and the Dehradun intermontane basin (Densmore et al., 2015). Within the Kangra Basin, Thakur et al. (2014) suggested an aggradation phase from 15 to 11 ka (during increasing ISM strength) based on OSL ages. These regionally correlative events suggest that despite increased precipitation and rising sediment transport capacity, an increased sediment flux to the rivers led to deposition in areas where the rivers encountered low-slope areas, such as, widened valley sections, intermontane basins ,or the foreland (Clift et al., 2012; Gibling et al., 2005). We suggest that transiently-stored material in the form of moraines, fill terraces, and hillslope regolith was mobilized during the strengthened monsoon phase at the transition from MIS2 to MIS1. A sharp increase in the ISM intensity could have also increased the frequency of landslides and debris flows which is observed within the AF2 fill.

The T3 terrace level marks the cessation of AF2 aggradation at ~10 ka, while the ISM was still very strong. Since ~ 8-6 ka, however, the ISM subsequently started to weaken again (Dykoski et al., 2005). Our exposure ages of terrace levels T4 through T6, marking the onset of repeated incision phases, illustrate a broad correlation with weakened monsoon phases in Holocene, and they correlate well with exposure ages of terraces in the Sutlej valley (Bookhagen et al., 2006). Incision during this period of decreasing transport capacity requires a decline in the sediment flux. This could have happened due to a decrease in hillslope erosion rates, potentially linked to the removal of easily eroded sediments from the source area during the early MIS1 strong monsoon. Together, the data furnishes support for fluvial aggradation during periods of high or increasing ISM intensity when the sediment flux was high, and incision during periods of low or decreasing ISM intensity, or mostly when the sediment flux was relatively low.

6.2. Out-of-sequence activity of the Jwalamukhi Thrust

Previous authors have used field relationships, seismic reflection profiles, balanced cross sections, and uplifted strath terraces to quantify the tectonic activity along the JMT (Powers et al., 1998; Thakur et al., 2014) on different timescales, but the age constraints and therefore rate estimates were limited. Powers et al. (1998) proposed that on average, nearly one third of the total Sub-Himalayan shortening (between the PT and the MFT) of 14 ± 2 $mm.a^{-1}$ has been accommodated during the Quaternary. However, this is a minimum estimate, as these authors used the approximate timing of cessation of sedimentation of the Upper Siwaliks to constrain the onset of folding and faulting. Revised stratigraphic constraints used by Hirschmiller et al. (2014) provide a shortening rate of 8.52±1.6 $mm.a^{-1}$ since 2.7±0.3 Ma, also using an interpolated age of the Upper/Middle Siwalik boundary. The rate estimates for Jwalamukhi Thrust (3.5-4.2 $mm.a^{-1}$) from Thakur et al. (2014) may underestimate the true deformation rates because their OSL ages likely overestimate the abandonment ages of the deformed terraces. I furnish new chronologic data and the application of a fault-bend fold model to quantify the deformation in the Sub-Himalaya result in a shortening rate of 5.6±0.8 to 7.5±1.0 $mm.a^{-1}$ across the JMT since 10±0.9 ka (the oldest obtained exposure (abandonment) age of terrace level T3), considering a range of different dip angles of the JMT fault plane.

Srivastava et al. (2009) suggested a rapid late Pleistocene sedimentation phase (< 78 ka) in the Kangra Basin, which they related to reactivation of the MBT and some other regional faults. The evidence for this fault reactivation, however, is ambiguous, and the sediment aggradation can alternatively be argued to result from a higher sediment supply due to climatic changes on multi-millennial time scales (Dey et al., 2016). In any case, the angular unconformity between the Siwalik units and the overlying Pleistocene alluvial fill suggest slip on the JMT was ongoing prior to deposition of the late Pleistocene sediments. In addition to the vertical offset of terrace T3 across the JMT, we also interpret the 12-13° northeast-tilted T2 terrace surface, situated near southwest of the town of Kangra to reflect motion along the MHT. Specifically, we suggest that motion along the fault transported the terrace from an initial position above the flat portion of the MHT onto the first thrust ramp segment along the JMT after terrace abandonment at ~15.6±1.2 ka.

In summary, our fault-slip rate estimates are supported by k_{sn} patterns, Vfw:Vh ratios, and field observations such as the back-tilted terrace suggesting activity of the JMT since at least 18 ka. Our results provide new and independent estimates of shortening on millennial time scales, which complement the previously proposed long-term average tectonic shortening rates (Powers et al., 1998; Thakur et al., 2014; Hirschmiller et al., 2014). Whereas the offset terrace allows us to constrain tectonic uplift due to JMT activity, the k_{sn} values on longitudinal stream profiles provide a qualitative estimate of uplift patterns across the entire region. Different segments of the hanging wall of the JMT are expected to have different uplift rates depending on the dip of the thrust plane. Indeed, the ramp segment with higher rock uplift yields higher k_{sn} values and lower Vfw:Vh ratios, while the flat segment yields lower k_{sn} values and higher Vfw:Vh ratios.

6.3. Impact of tectonic uplift on fluvial incision

Slip along the JMT plane since at least Holocene has caused differential uplift on the hanging wall, with variations in uplift rate due to a change in the dip angle of the fault plane over the ramp-flat transition. Fill terraces within the Kangra Basin that overlie the flat segment should show a ~1.5 mm.a^{-1} uplift rate associated with tectonic uplift, whereas strath and cut-and-fill terraces on the ramp shows a ~4.5 mm.a^{-1} uplift rate (Dey et al., 2016 –Chapter 4). At steady state, the surface uplift must be balanced by fluvial incision. Hence, we can predict that nearly 15 m of the total incision after the formation of T3 (~10 ka) is related to tectonic uplift. However, because post-T3 incision over the flat is 55-60 m, we conclude that a majority of the incision is governed by changes in the balance between sediment flux and fluvial transport capacity within the system, which in turn is governed by climate change.

6.4. Potential feedback of variations in sediment delivery on regional tectonics

Previous workers (Powers et al., 1998; Malik et al., 2007; Thakur et al., 2014) have inferred that only the Sub-Himalayan thrusts (JMT, ST, MFT, and related back-thrusts) are accommodating modern crustal shortening. Although potential activity on the MBT has been proposed in the NW Himalaya based on thermochronology data (Deeken et al., 2011; Thiede et al., 2016- Chapter 5), which would suggest an overall reduced contribution of Sub-Himalayan shortening, the long averaging time scale of thermochronology data makes it difficult to accurately assess recent activity. Thakur et al. (2014) proposed a shortening rate of 3.5 to 4.2 mm.a^{-1} on the JMT over the last 30 ka and 6 to 6.9 mm.a^{-1} on the MFT over the last 40 ka. Powers et al. (1998) proposed that 25-30% of the total Sub-Himalayan shortening has been accommodated by the JMT. With our new shortening estimates over the last ~10 ka (5.6±0.8 to 7.5±1.0 mm.a^{-1}), we show that Holocene shortening on the JMT has been comparable to the activity of the MFT estimated over 30 ka (Thakur et al., 2014). This study reveals that the JMT accommodates ~40-50 % of the total convergence across the NW Himalaya at least since the Holocene. Hence, it appears as if the majority of the Holocene shortening has been nearly equally distributed over the JMT and other Sub-Himalayan thrusts (including the MFT) in the Kangra re-entrant.

To try to explain why so much Holocene shorting has been accommodated within the interior of the Sub-Himalaya in the form of out-of-sequence faulting, we consider the critically-tapered wedge model (Davis et al., 1983). In analogue and numerical models of critically tapered wedges, changes in sedimentary load have been shown to influence the location of faulting (Davis et al., 1983). Sediment aggradation within intermontane valleys or near the front of a wedge can potentially increase the taper and thus induce foreland propagation of deformation to maintain critical taper (Dahlen, 1988; Willett & Beaumont, 1994; Hilley and Strecker, 2004). Conversely, removal of stored sediments in intermontane basins lower the frontal taper, rendering it sub-critical, and hence causing the retreat of the deformation front and out-of-sequence thrusting, until the wedge re-establishes its critical taper (Dahlen, 1990). The applicability of the critical taper model for the whole Himalaya is highly debated and is certainly oversimplified. Nonetheless, it has commonly been used as a first-order framework to explain the tectonic evolution and deformation of the frontal fold-and-thrust belt of the Himalaya, as this region satisfies the mechanical criteria for the evolution of a critical Coulomb wedge (Hilley and Strecker, 2004; Mugnier et al., 2004; Mukul et al., 2010; Singh et al., 2012; Hirschmiller et al., 2014).

In this context, the deformation pattern within the Sub-Himalaya may be linked to the history of sediment aggradation and removal in the Kangra re-entrant. Considering an initial in-sequence development of the major thrusts within the Kangra re-entrant, the JMT must have once been the southernmost deformation front of the Himalayan wedge. With continuous convergence between the Himalaya and the underthrusting Indian plate, new surface-breaking thrusts emerged, extending the MHT décollement towards the foreland. Based on balanced cross-sections and seismic profiles (Powers et al., 1998), we can deduce a total shortening on the JMT of 6 to 6.8 km and obtain long-term average shortening rate of 3.6±0.3 mm.a^{-1}. From the same balanced cross-sections, we can deduce a long-term average slip rate of 0.7±0.2 mm.a^{-1} on the MFT. These rates are significantly below slip estimates averaged since the late Pleistocene or Holocene, including those from Thakur et al., (2014) and from this study. This inconsistency between short- and long-term slip estimates points to temporal variation of fault activity throughout the last 1.6-1.9 Ma, possibly with periods of low or no activity.

Sediment cycles operate on 10^4-10^5 year timescales and can potentially influence tectonic stress-fields by changing the sediment load (Hilley and Strecker, 2004; 2005). Extensive aggradation reaching up to the contiguous foreland around 40-50 ka has been reported by many previous studies (Gibling et al., 2005; Clift et al., 2012; Thakur et al., 2014). Late Pleistocene sediment aggradation of more than 200 m across the Kangra Basin (from ~80–20 ka) (Srivastava et al., 2009; Dey et al., 2016) spanning more than ~1500 km^2 over the hanging wall of the JMT may have stabilized the critical taper involving the JMT-MHT during times of high loading and therefore forced deformation to localize towards the frontal structures of the wedge. Later, when the transiently-stored basin-fill sediments were excavated (only 10-15% of the total volume of sediments stored during full-basin stage remains at present on the hanging wall of JMT), the effective normal stresses on the décollement of the JMT would have been reduced, potentially leading to a sub-critical taper (Singh et al., 2012). By transfer or renewal of out-of-sequence fault activity to inherited structures such as the JMT within the Kangra re-entrant, the critical taper would have been restored. Although detailed modeling is necessary to test these ideas in detail, the coincidence in the timing of sediment excavation from the Kangra Basin with an apparent increase in slip rate along the JMT provides a compelling argument for linking the two events in the context of a critically tapered wedge.

6.5. Activity and structure of the MBT in the Kangra sector

By combining topographic, structural, and rock cooling patterns as input parameters for the 3D thermokinematic modeling, we were able obtain information on the timing of faulting and rates of exhumation as well as important implications on the structural architecture of the Dhauladhar range to the front of and adjacent to the orogen interior.

All AFT samples across the Dhauladhar range yielded young cooling ages between 1.7±0.3 and 3.7±0.4 Ma, despite strong differences in sample elevations (ΔZ=2.8 km). Furthermore, up to ~40 km north of the MBT, the AFT ages appear to be elevation invariant, suggesting a high vertical rock uplift component. Such a perturbation of the thermal field implies the existence of a ~40-km-long and deep-seated MBT fault ramp beneath the Dhauladhar range, forcing the rocks to uplift and cool rapidly. In contrast, across the Pir Panjal range in the orogen interior, AFT ages yield older ages (3.5±0.8-9.3±0.9 Ma), show much larger scatter, and indicate some degree of elevation dependency. Overall, these ages indicate significant lower exhumations rates across Pir Panjal than across the Dhauladhar range when passing the AFT-closure isotherm range (Deeken et al., 2011).

The exposure of greenschist facies rocks in the hanging wall of the MBT versus unmetamorphosed rock in the footwall documents approximately ~20-35 km of fault displacement. The MBT fault ramp lies beneath the frontal range, which has maintained a high crest line, with peaks exceeding 5000 m asl to this day. This is in clear contrast to observations made by Najman et al. (2009), who described that the MBT hanging wall at the eastern end of the Kangra re-entrant consists of non–metamorphosed rocks and illustrates significant lateral variation in mean fault displacement and exhumation along the MBT hanging wall. Their findings were consistent with many other MBT segments along-strike of the orogen (DeCelles et al., 2001; Hodges, 2000). These field observations strongly suggest that significant fault displacement is the only thing that can explain the change in metamorphic grade observed across the MBT fault zone. The ZHe ages show some scattered age-elevation relationship, as well as systematic younger ages along the toe of the Dhauladhar range. Previous works using constraints from abrupt changes in the sedimentary records of the Siwaliks with the Kangra re-entrant suggest an onset of MBT fault activity between 8 and 10 Ma ago (Brozovic and Burbank, 2000; Meigs et al., 1995). This also implies that the rocks yielding ZHe ages < 10 Ma have been at least partially or fully reset since the onset of MBT activity and are only documenting the onset of the recent deformation of the Himalayan range front in this segment.

Several structural fault geometries of the Himalayan wedge were tested for the studied segment of the Northwest Himalaya. Only one of the tested scenarios, an imbricated MBT fault ramp rooted to the MHT, could explain the observed cooling pattern derived from the low-temperature thermochronology data. Neither a ‘flat-ramp’ geometry nor a duplex beneath the Pir Panjal range would be sufficient to reproduce the observed cooling age pattern. This is also supported by the regional scatter of smaller-magnitude earthquakes ($M < 5$) (Gahalaut and Kundu, 2012), which indicates an absence of any mid-crustal ramp along the MHT within this segment, unlike in other Himalayan segments. This suggests that the MHT décollement dips with a uniform trend of ~ 3–5° to the NE, and has not formed ramp structure beneath the Dhauladhar range. Furthermore, we used another set of forward models to test deviant MBT dip angles and discovered that a dip of 30 to 40° (MBT ramp) yielded the lowest misfit between the observed and the modeled ages. A similar dip of the MBT has been reported by Adlakha et al. (2013) for the Dalhousie region, 50 km west of this area. Together with the aforementioned assumption on the structural information derived from the thermochronometric dating, the minimum fault displacement on the frontal fault is in the range of 25 to 30 km, which suggests uniform slip rates of ~ 2.5 to 3 $\mathrm{mm.a^{-1}}$ on the MBT. Our modeling yields a basal temperature between 625–672°C at 25 km crustal depth, which leads to overall thermal gradients of 25–27°C/km. At the point in depth where the MBT merges with the décollement, this thermal gradient would result in a temperature slightly above 300°C. The inferred lower greenschist facies conditions, derived from the mineral assemblages observed in the field, presume a temperature of 300–450°C and 1–4 kbar of pressure. This corresponds to a depth lower than 15 kilometers and therefore fits with the assumed structural architecture. As mentioned above, other geometries would exhume material from a greater depth, resulting in increased metamorphic facies, which has only been observed north of the Pir Panjal (Deeken et al., 2011), where uplift across the Gianbul dome comprises different fault relations and thermal regimes.

This study also accounts for the sensitivity of the models to different MBT initiation timings. These models show that a minimum MBT activity of 6 Myr would be necessary to reproduce the observed cooling age pattern and at least 8–10 Myr would be needed to establish a time–invariant pattern. Such a pattern evolves if the exhumation is in a near-steady state (Willet and Brandon, 2002). Therefore, our model results are in agreement with the sedimentary constraints presented by Meigs et al. (1995) — the Dhauladhar range could have nearly achieved an exhumational steady state for at least the last couple of million years.

In summary, our study highlights the complex relationship between morphology, underlying structural architecture, and thermochronometric systems. It also emphasizes the outstanding role of the Dhauladhar range as a structurally unique range front segment among the along-strike Himalayan fault segments. The local exhumation history is strongly interconnected with the underlying structural architecture and dates back to at least 6 Ma, if not the last 8–10 Ma. This segment probably accommodated about 2 mm.a^{-1} of crustal shorting over the last 10 Ma, which has not been recognized during estimates of the Himalayan wedge across this segment by previous workers, who have argued that the Sub-Himalaya has accommodated the total Himalayan crustal shortening for 2 Ma.

6.6. Conclusions

These aforesaid investigations provide to some key information for understanding the tectonic-climatic impact on Earth’s surface processes on different timescales. This particular case study from the Kangra Basin demonstrate how changes in climatic forcing and sediment flux affects the sediment routing from the Himalayan orogen and how that variation in sediment routing can have a feedback on the regional tectonic scenario. This study also portrays a new approach to estimate fault displacement rates over 10^3-10^4 year timescales. Along with these findings, compilation of low-temperature thermochronology data from the Dhauladhar range provide an assessment of the activity of the MBT and the geometry of the Himalayan orogenic wedge in this sector.

By combining our new surface-exposure data with previously published OSL (Thakur et al., 2014) and IRSL (Srivastava et al., 2009) ages, we inferred that pronounced aggradation pulses as well as incision events in the Kangra Basin largely correlate with climatic trends on varying timescales. On 10^4-yr timescales, net aggradation occurred during the first half of the last glacial cycle (~100 to ~60 ka), and net incision occurred during the second half (~50 ka). On shorter timescales of 10^3-10^4 years, aggradation occurred during relatively small time windows when the ISM intensity became stronger or when the sediment flux was especially high. In contrast, incision into the aggraded material (marked by terrace formation) occurred during periods of weaker or decreasing monsoon intensity and when the sediment supply was low. Our constraints on the timing of fluvial incision in the Kangra Basin reveal that it was coeval with incision from the Sutlej Valley, suggesting regionally synchronous sediment transport cycles affected by climate change.

Within the intermontane Kangra Basin, the deformation of well-preserved Holocene terraces (especially the T3 terrace) indicates neotectonic activity along the Jwalamukhi Thrust (JMT). Differential uplift of 44±5 m of the best-preserved terrace level (T3) across the JMT suggests out-of-sequence faulting along the JMT and yields a shortening rate of 5.6±0.8 to 7.5±1.0 mm.a^{-1} over the last ~10 ka. In the context of the published shortening rates averaged over the past ~1.9-1.6 Ma (Powers et al., 1998), ~2.3 Ma (Hirschmiller et al., 2014), and 30 to 40 ka (Thakur et al., 2014), as well as GPS-derived shortening rates (Kundu et al., 2014), our results suggest that a significant proportion of the shortening has been accommodated by the JMT over the Holocene. This shortening corresponds to about 40 to 60% of the total Sub-Himalayan shortening, or 35 to 50% of the total convergence accommodated within the Himalaya. We propose that the recent out-of-sequence faulting that we documented along the JMT is potentially related to a tectonic reorganization triggered by temporal variations in sedimentary loading within the toe area of the Himalayan orogenic wedge. The climate-driven sediment cycles in the interior of the Sub-Himalayan wedge disturb the critical condition and, most likely, prompted the tectonic re-organization we observed in the area that has taken place since the beginning of the Holocene at the latest.

Recent studies have proposed that all the shortening accommodated by the Himalayan wedge is achieved by the shortening of the Sub-Himalayan fold-thrust belt. However, the exhumation pattern of the MBT hanging wall rocks and thermokinematic PECUBE modeling of the Dhauladhar range front suggest that a long-term shortening of ~2 mm.a^{-1} has been accommodated by the MBT since the mid-Miocene. This also means that, on a longer timescale, the MBT has achieved nearly 10-20% of the total convergence in this transect of the Northwest Himalaya. Moreover, the absence of a Lesser Himalayan duplex or mid-crustal ramp and the typical exhumation pattern suggest a deep-seated steep ramp on the MHT below the Dhauladhar range, which is strikingly dissimilar to the Kullu-Rampur and the Kishtwar sections nearby or even the frequently-studied Central Nepal sector to the east.

References

Ader, T., Avouac, J.-P., Liu-Zeng, J., Lyon-Caen, H., Bollinger, L., Galetzka, J., Genrich, J., Thomas, M., Chanard, K., Sapkota, S.N., others, 2012. Convergence rate across the Nepal Himalaya and interseismic coupling on the Main Himalayan Thrust: Implications for seismic hazard. J. Geophys. Res. Solid Earth 117.

Adlakha, V., Patel, R.C., Lal, N., Mehta, Y.P., Jain, A.K., and Kumar, A., 2013, Tectonics and climate interplay: exhumation patterns of the Dhauladhar Range, Northwest Himalaya: Current Science, v. 104 p. 1551.

Ali, S., Hathorne, E.C., Frank, M., Gebregiorgis, D., Stattegger, K., Stumpf, R., Kutterolf, S., Johnson, J.E., Giosan, L., 2015. South Asian monsoon history over the past 60 kyr recorded by radiogenic isotopes and clay mineral assemblages in the Andaman Sea. Geochemistry Geophys. Geosystems 16, 505–521. doi:10.1002/2014gc005586

Allen, J.P., Fielding, C.R., Rygel, M.C., Gibling, M.R., 2013. Deconvolving Signals of Tectonic and Climatic Controls From Continental Basins: An Example From the Late Paleozoic Cumberland Basin, Atlantic Canada. J. Sediment. Res. 83, 847–872. doi:10.2110/jsr.2013.58

Allen, P. and Heller, P.A., 2012. Dispersal and preservation of tectonically generated alluvial gravels in sedimentary basins. Tectonics Sediment. Basins Recent Adv. 111–130.

Anderson, B., Mackintosh, A., 2006. Temperature change is the major driver of late-glacial and Holocene glacier fluctuations in New Zealand. Geology 34, 121–124. doi:10.1130/g22151.1

Anderson, R.S., Repka, J.L., Dick, G.S., 1996. Explicit treatment of inheritance in dating depositional surfaces using in situ 10Be and 26Al. Geology 24, 47–51. doi:10.1130/0091-7613(1996)024<0047:ETOIID>2.3.CO

Armitage, J.J., Duller, R.A., Whittaker, A.C., Allen, P.A., 2011. Transformation of tectonic and climatic signals from source to sedimentary archive. Nat. Geosci. 4, 231–235. doi:10.1038/ngeo1087

Avouac, J.-P., Meng, L., Wei, S., Wang, T., Ampuero, J.-P., 2015. Lower edge of locked Main Himalayan Thrust unzipped by the 2015 Gorkha earthquake. Nat. Geosci. 8, 708–711.

Avouac, J., Tapponnier, P., 1993. Kinematic model of active deformation in central Asia. Geophys. Res. Lett. 20, 895. doi:10.1029/93GL00128

Balco, G., Stone, J.O., Lifton, N.A., Dunai, T.J., 2008. A complete and easily accessible means of calculating surface exposure ages or erosion rates from (10)Be and (26)Al measurements. Quat. Geochronol. 3, 174–195. doi:10.1016/j.quageo.2007.12.001

Banerjee, P., Burgmann, R., 2002. Convergence across the northwest Himalaya from GPS measurements. Geophys. Res. Lett. 29. doi:10.1029/2002gl015184

Beaumont, C., Jamieson, R.A., Nguyen, M.H., Lee, B., 2001. Himalayan tectonics explained by extrusion of a low-viscosity crustal channel coupled to focused surface denudation. Nature 414, 738–742. doi:10.1038/414738a

Benn, D.I., Owen, L.A., 1998. The role of the Indian summer monsoon and the mid-latitude westerlies in Himalayan glaciation: review and speculative discussion. J. Geol. Soc. London. 155, 353–363. doi:10.1144/gsjgs.155.2.0353

Berger, A., Loutre, M.-F., 1991. Insolation values for the climate of the last 10 million years. Quat. Sci. Rev. 10, 297–317.

Bettinelli, P., Avouac, J.P., Flouzat, M., Jouanne, F., Bollinger, L., Willis, P., Chitrakar, G.R., 2006. Plate motion of India and interseismic strain in the Nepal himalaya from GPS and DORIS measurements. J. Geod. 80, 567–589.

Bilham, R., Gaur, V.K., Molnar, P., 2001. Earthquakes - Himalayan seismic hazard. Science (80-.). 293, 1442–1444. doi:10.1126/science.1062584

Bilham, R., Larson, K., Freymueller, J., Jouanne, F., LeFort, P., Leturmy, P., Mugnier, J.L., Gamond, J.F., Glot, J.P., Martinod, J., Chaudury, N.L., Chitrakar, G.R., Gautam, U.P., Koirala, B.P., Pandey, M.R., Ranabhat, R., Sapkota, S.N., Shrestha, P.L., Thakuri, M.C., Timilsina, U.R., Tiwari, D.R., Vidal, G., Vigny, C., Galy, A., deVoogd, B., 1997. GPS measurements of present-day convergence across the Nepal Himalaya. Nature 386, 61–64. doi:10.1038/386061a0

Blothe, J.H., Munack, H., Korup, O., Fulling, A., Garzanti, E., Resentini, A., Kubik, P.W., 2014. Late Quaternary valley infill and dissection in the Indus River, western Tibetan Plateau margin. Quat. Sci. Rev. 94, 102–119. doi:10.1016/j.quascirev.2014.04.011

Bollinger, L., Avouac, J.P., Cattin, R., Pandey, M.R., 2004. Stress buildup in the Himalaya. J. Geophys. Res. Earth 109. doi:10.1029/2003jb002911

Bookhagen, B., 2010. Appearance of extreme monsoonal rainfall events and their impact on erosion in the Himalaya. Geomatics Nat. Hazards Risk 1, 37–50. doi:10.1080/19475701003625737

Bookhagen, B., Burbank, D.W., 2006a. Topography, relief, and TRMM-derived rainfall variations along the Himalaya. Geophys. Res. Lett. 33, 5. doi:10.1029/2006gl026037

Bookhagen, B., Burbank, D.W., 2010. Toward a complete Himalayan hydrological budget: Spatiotemporal distribution of snowmelt and rainfall and their impact on river discharge. J. Geophys. Res. Surf. 115. doi:10.1029/2009jf001426

Bookhagen, B., Fleitmann, D., Nishiizurrli, K., Strecker, M.R., Thiede, R.C., 2006b. Holocene monsoonal dynamics and fluvial terrace formation in the northwest Himalaya, India. Geology 34, 601–604. doi:10.1130/g22698.1

Bookhagen, B., Thiede, R.C., Strecker, M.R., 2005a. Abnormal monsoon years and their control on erosion and sediment flux in the high, and northwest Himalaya. Earth Planet. Sci. Lett. 231, 131–146. doi:10.1016/j.epsl.2004.11.014

Bookhagen, B., Thiede, R.C., Strecker, M.R., 2005b. Late Quaternary intensified monsoon phases control landscape evolution in the northwest Himalaya. Geology 33, 149–152. doi:10.1130/g20982.1

Borchers, B., Marrero, S., Balco, G., Caffee, M., Goehring, B., Lifton, N., Nishiizumi, K., Phillips, F., Schaefer, J., Stone, J., 2016. Geological calibration of spallation production rates in the CRONUS-Earth project. Quat. Geochronol. 31, 188–198.

Braun, J., 2002a, Estimating exhumation rate and relief evolution by spectral analysis of age-elevation datasets: Terra Nova, v. 14, p. 210-214.

Braun, J., 2002b, Quantifying the effect of recent relief changes on age-elevation relationships: Earth And Planetary Science Letters, v. 200, p. 331-343.

Braun, J., van der Beek, P., Valla, P., Robert, X., Herman, F., Glotzbach, C., Pedersen, V., Perry, C., Simon-Labric, T., and Prigent, C., 2012, Quantifying rates of landscape evolution and tectonic processes by thermochronology and numerical modeling of crustal heat transport using PECUBE: Tectonophysics, v. 524–525, p. 1-28.

Brocard, G.Y., Van Der Beek, P.A., Bourlès, D.L., Siame, L.L., Mugnier, J.-L., 2003. Long-term fluvial incision rates and postglacial river relaxation time in the French Western Alps from 10 Be dating of alluvial terraces with assessment of inheritance, soil development and wind ablation effects. Earth Planet. Sci. Lett. 209, 197–214.

Brookfield, M.E., 1993. The Himalayan Passive Margin From Precambrian To Cretaceous Times. Sediment. Geol. 84, 1–35. doi:10.1016/0037-0738(93)90042-4

Brozovic, N., and Burbank, D.W., 2000, Dynamic fluvial systems and gravel progradation in the Himalayan foreland: Geological Society of America Bulletin, v. 112, p. 394-412.

Brozovic, N., Burbank, D.W., 2000. Dynamic fluvial systems and gravel progradation in the Himalayan foreland. Geol. Soc. Am. Bull. 112, 394–412. doi:10.1130/0016-7606(2000)112<0394:dfsagp>2.3.co;2

Bull, W.B., 1964. History + Causes of Channel Trenching in Western Fresno County California. Am. J. Sci. 262, 249–&. doi:10.2475/ajs.262.2.249

Bull, W.B., 2007. Tectonic geomorphology of mountains.

Burbank, D.W., Raynolds, R.G.H., 1988. Stratigraphic keys to the timing of thrusting in terrestrial foreland basins: Applications to the northwestern Himalaya, in: New Perspectives in Basin Analysis. Springer, pp. 331–351.

Burchfiel, B.C., Zhiliang, C., Hodges, K. V, Yuping, L., Royden, L.H., Changrong, D., Jiene, X., 1992. The South Tibetan detachment system, Himalayan orogen: Extension contemporaneous with and parallel to shortening in a collisional mountain belt. Geol. Soc. Am. Spec. Pap. 269, 1–41.

Carosi, R., Lombardo, B., Musumeci, G., Pertusati, P.C., 1999. Geology of the Higher Himalayan Crystallines in Khumbu Himal (Eastern Nepal). J. Asian Earth Sci. 17, 785–803. doi:10.1016/s1367-9120(99)00014-0

Chmeleff, J., von Blanckenburg, F., Kossert, K., Jakob, D., 2010. Determination of the 10Be half-life by multicollector ICP-MS and liquid scintillation counting. Nucl. Instruments Methods Phys. Res. Sect. B Beam Interact. with Mater. Atoms 268, 192–199. doi:10.1016/j.nimb.2009.09.012

Clift, P.D., Carter, A., Giosan, L., Durcan, J., Duller, G.A.T., Macklin, M.G., Alizai, A., Tabrez, A.R., Danish, M., VanLaningham, S., Fuller, D.Q., 2012. U-Pb zircon dating evidence for a Pleistocene Sarasvati River and capture of the Yamuna River. Geology 40, 211–214.

Clift, P.D., Hodges, K. V., Heslop, D., Hannigan, R., Van Long, H., Calves, G., 2008. Correlation of Himalayan exhumation rates and Asian monsoon intensity. Nat. Geosci. doi:10.1038/ngeo351

Clift, P.D., Shimizu, N., Layne, G.D., Blusztajn, J.S., Gaedicke, C., Schluter, H.U., Clark, M.K., Amjad, S., 2001. Development of the Indus Fan and its significance for the erosional history of the Western Himalaya and Karakoram. Geol. Soc. Am. Bull. 113, 1039–1051. doi:10.1130/0016-7606(2001)113<1039:dotifa>2.0.co;2

Coutand, I., Whipp, D.M., Grujic, D., Bernet, M., Fellin, M.G., Bookhagen, B., Landry, K.R., Ghalley, S.K., and Duncan, C., 2014, Geometry and kinematics of the Main Himalayan Thrust and Neogene crustal exhumation in the Bhutanese Himalaya derived from inversion of multithermochronologic data: Journal of Geophysical Research: Solid Earth, v. 119, p. 1446-1481.

Curray, J.R., Moore, D.G., 1971. Growth of the Bengal deep-sea fan and denudation in the Himalayas. Bull. Geol. Soc. Am. 82, 563–572.

Dahlen, F., 1990. Critical Taper Model Of Fold-And-Thrust Belts And Accretionary Wedges. Annu. Rev. Earth Planet. Sci. 18, 55–99. doi:10.1146/annurev.earth.18.1.55

Davis, D., Suppe, J., Dahlen, F.A., 1983. Mechanics of fold-and- thrust belts and accretionary wedges. J. Geophys. Res. 88, 1153–1172.

Debret, M., Bout-Roumazeilles, V., Grousset, F., Desmet, M., McManus, J.F., Massei, N., Sebag, D., Petit, J.R., Copard, Y., Trentesaux, A., 2007. The origin of the 1500-year climate cycles in Holocene North-Atlantic records. Clim. Past 3, 569–575.

DeCelles, P.G., Robinson, D.M., Quade, J., Ojha, T.P., Garzione, C.N., Copeland, P., Upreti, B.N., 2001. Stratigraphy, structure, and tectonic evolution of the Himalayan fold-thrust belt in western Nepal. Tectonics 20, 487–509. doi:10.1029/2000tc001226

DeCelles, P.G., Robinson, D.M., Quade, J., Ojha, T.P., Garzione, C.N., Copeland, P., and Upreti, B.N., 2001, Stratigraphy, structure, and tectonic evolution of the Himalayan fold-thrust belt in western Nepal: Tectonics, v. 20, p. 487-509.

Deeken, A., Thiede, R.C., Sobel, E.R., Hourigan, J.K., Strecker, M.R., 2011. Exhumational variability within the Himalaya of northwest India. Earth Planet. Sci. Lett. 305, 103–114. doi:10.1016/j.epsl.2011.02.045

DeMets, C., Gordon, R.G., Argus, D.F., Stein, S., 1990. Current plate motions. Geophys. J. Int. 101, 425–478. doi:10.1111/j.1365-246X.1990.tb06579.x

Densmore, A.L., Sinha, R., Sinha, S., Tandon, S.K., Jain, V., 2015. Sediment storage and release from Himalayan piggyback basins and implications for downstream river morphology and evolution. Basin Res.

Dewald, a., Heinze, S., Jolie, J., Zilges, a., Dunai, T., Rethemeyer, J., Melles, M., Staubwasser, M., Kuczewski, B., Richter, J., Radtke, U., von Blanckenburg, F., Klein, M., 2013. CologneAMS, a dedicated center for accelerator mass spectrometry in Germany. Nucl. Instruments Methods Phys. Res. Sect. B Beam Interact. with Mater. Atoms 294, 18–23. doi:10.1016/j.nimb.2012.04.030

Dey, S., Thiede, R. C., Schildgen, T. F., Wittmann, H., Bookhagen, B., Scherler, D., Jain, V. and Strecker, M. R. (2016). Climate-driven sediment aggradation and incision since the late Pleistocene in the NW Himalaya, India. *Earth and Planetary Science Letters*, *449*, 321-331.

Dey, S., Thiede, R., Schildgen, T., and Strecker, M., in revision, Tectonic control on Pleistocene basin-filling processes and landscape evolution: the intermontane Kangra Basin, NW Sub-Himalaya, India: Tectonics.

DiPietro, J.A., Pogue, K.R., 2004. Tectonostratigraphic subdivisions of the Himalaya: A view from the west. Tectonics 23. doi:10.1029/2003tc001554

Dortch, J.M., Owen, L.A., Caffee, M.W., 2013. Timing and climatic drivers for glaciation across semi-arid western Himalayan-Tibetan orogen. Quat. Sci. Rev. 78, 188–208.

Dunai, T.J., 2010. Cosmogenic nuclides: principles, concepts and applications in the earth surface sciences. Cambridge University Press.

Dunne, J., Elmore, D., Muzikar, P., 1999. Scaling factors for the rates of production of cosmogenic nuclides for geometric shielding and attenuation at depth on sloped surfaces. Geomorphology 27, 3–11.

Dutt, S., Gupta, A.K., Clemens, S.C., Cheng, H., Singh, R.K., Kathayat, G., Edwards, R.L., 2015. Abrupt changes in Indian summer monsoon strength during 33,800 to 5500years BP. Geophys. Res. Lett. 42, 5526–5532. doi:10.1002/2015gl064015

Dutta, S., Suresh, N., Kumar, R., 2012. Climatically controlled Late Quaternary terrace staircase development in the fold-and-thrust belt of the Sub Himalaya. Palaeogeogr. Palaeoclimatol. Palaeoecol. 356, 16–26.

Duvall, A., Kirby, E., Burbank, D., 2004. Tectonic and lithologic controls on bedrock channel profiles and processes in coastal California. J. Geophys. Res. Surf. 109. doi:10.1029/2003jf000086

Dykoski, C.A., Edwards, R.L., Cheng, H., Yuan, D., Cai, Y., Zhang, M., Lin, Y., Qing, J., An, Z., Revenaugh, J., 2005. A high-resolution, absolute-dated Holocene and deglacial Asian monsoon record from Dongge Cave, China. Earth Planet. Sci. Lett. 233, 71–86.

Ehlers, T.A., 2005, Crustal Thermal Processes and the Interpretation of Thermochronometer Data, *in* Reiners, P.W., ed., Low-Temperature Thermochronology: Techniques, Interpretations, and Applications, Volume 58: Reviews in Minerology & Geochemistry, Mineralogical Society of America, p. 315-350.

Einsele, G., Ratschbacher, L., Wetzel, A., 1996. The Himalaya-Bengal fan denudation accumulation system during the past 20 Ma. J. Geol. 104, 163–184.

Eugster, P., Scherler, D., Thiede, R.C., Codilean, A.T., Strecker, M.R., 2016. Rapid Last Glacial Maximum deglaciation in the Indian Himalaya coeval with midlatitude glaciers: New insights from 10Be-dating of ice-polished bedrock surfaces in the Chandra Valley, NW Himalaya. Geophys. Res. Lett.

Farley, K.A., Wolf, R.A., and Silver, L.T., 1996, The effects of long alpha-stopping distances on (U-Th)/He ages: Chemical Geology, v. 60, p. 4223-4229.

Finkel, R.C., Owen, L.A., Barnard, P.L., Caffee, M.W., 2003. Beryllium-10 dating of Mount Everest moraines indicates a strong monsoon influence and glacial synchroneity throughout the Himalaya. Geology 31, 561–564. doi:10.1130/0091-7613(2003)031<0561:bdomem>2.0.co;2

Fleitmann, D., Burns, S.J., Mudelsee, M., Neff, U., Kramers, J., Mangini, A., Matter, A., 2003. Holocene forcing of the Indian monsoon recorded in a stalagmite from Southern Oman. Science (80-.). 300, 1737–1739. doi:10.1126/science.1083130

Flint, R.F., 1974. 3 Theories In Time. Quat. Res. 4, 1–8. doi:10.1016/0033-5894(74)90059-3

Flint, R.F., 1974. Three theories in time. Quat. Res. 4, 1–8. doi:10.1016/0033-5894(74)90059-3

France-Lanord, C., 2004. Past and present fluxes from the Himalaya to the Bengal Fan. Geochim. Cosmochim. Acta 68, A419–A419.

Frostick, S. J., & Jones, L.E., 2002. Impact of periodicity on sediment flux in alluvial systems: grain to basin scale. Geol. Soc. London, Spec. Publ. 81–95.

Gahalaut, V.K., and Kundu, B., 2012, Possible influence of subducting ridges on the Himalayan arc and on the ruptures of great and major Himalayan earthquakes: Gondwana Research, v. 21, p. 1080-1088.

Gansser, A., 1964. Geology of the Himalayas. Intersci. Publ., New York.

Gao, R., Lu, Z., Klemperer, S.L., Wang, H., Dong, S., Li, W., and Li, H., 2016, Crustal-scale duplexing beneath the Yarlung Zangbo suture in the western Himalaya: Nature Geosci, v. advance online publication.

Garzanti, E., Baud, A., Mascle, G., 1987. Sedimentary Record Of The Northward Flight Of India And Its Collision With Eurasia (Ladakh Himalaya, India). Geodin. Acta 1, 297–312.

Gibling, M.R., Tandon, S.K., Sinha, R., Jain, M., 2005. Discontinuity-bounded alluvial sequences of the southern gangetic plains, India: Aggradation and degradation in response to monsoonal strength. J. Sediment. Res. 75, 369–385. doi:10.2110/jsr.2005.029

Gleadow, A.J.W., and Duddy, I.R., 1981, A natural long-term track annealing experiment for apatite: Nuclear Tracks, v. 5, p. 169-174.

Goodbred, S.L., 2003. Response of the Ganges dispersal system to climate change: A source-to-sink view since the last interstade. Sediment. Geol. 162, 83–104.

Goswami, P.K., Mishra, J.K., 2013. Climatic and tectonic controls on the sedimentary processes of an alluvial fan of the western Ganga Plain, India. Geol. Mag. 150, 240–253. doi:10.1017/s0016756812000490

Granger, D.E., Riebe, C.S., 2007. Cosmogenic nuclides in weathering and erosion. Treatise on geochemistry 5, 1–43.

Grujic, D., Coutand, I., Bookhagen, B., Bonnet, S., Blythe, A., Duncan, C., 2006. Climatic forcing of erosion, landscape, and tectonics in the Bhutan Himalayas. Geology 34, 801–804. doi:10.1130/g22648.1

Gupta, S., 1997. Himalayan drainage patterns and the origin of fluvial megafans in the Ganges foreland basin. Geology 25, 11–14. doi:10.1130/0091-7613(1997)025<0011:hdpato>2.3.co;2

Harvey, A.M., 1991. The influence of sediment supply on the channel morphology of - Howgill fells, Northwest England. Earth Surf. Process. Landforms 16, 675–684. doi:10.1002/esp.3290160711

Heyman, J., 2014. Paleoglaciation of the Tibetan Plateau and surrounding mountains based on exposure ages and ELA depression estimates. Quat. Sci. Rev. 91, 30–41.

Hidy, A.J., Gosse, J.C., Pederson, J.L., Mattern, J.P., Finkel, R.C., 2010. A geologically constrained Monte Carlo approach to modeling exposure ages from profiles of cosmogenic nuclides: An example from Lees Ferry, Arizona. Geochemistry Geophys. Geosystems 11. doi:10.1029/2010gc003084

Hilley, G.E., Strecker, M.R., 2004. Steady state erosion of critical Coulomb wedges with applications to Taiwan and the Himalaya. J. Geophys. Res. Earth 109. doi:10.1029/2002jb002284

Hilley, G.E., Strecker, M.R., 2005. Processes of oscillatory basin filling and excavation in a tectonically active orogen: Quebrada del Toro Basin, NW Argentina. Geol. Soc. Am. Bull. 117, 887–901. doi:10.1130/b25602.1

Hirschmiller, J., Grujic, D., Bookhagen, B., Coutand, I., Huyghe, P., Mugnier, J.-L., Ojha, T., 2014. What controls the growth of the Himalayan foreland fold-and-thrust belt? Geology 42, 247–250. doi:10.1130/g35057.1

Hodges, K. V, 2000. Tectonics of the Himalaya and southern Tibet from two perspectives. Geol. Soc. Am. Bull. 112, 324–350. doi:10.1130/0016-7606(2000)112<0324:tothas>2.3.co;2

Hodges, K. V, Wobus, C., Ruhl, K., Schildgen, T., Whipple, K., 2004. Quaternary deformation, river steepening, and heavy precipitation at the front of the Higher Himalayan ranges. Earth Planet. Sci. Lett. 220, 379–389. doi:10.1016/s0012-821x(04)00063-9

Hodges, K.V., 2000, Tectonics of the Himalaya and southern Tibet from two perspectives: Geological Society of America Bulletin, v. 112, p. 324-350.

Huang, W.L., Yang, X.P., Li, A., Thompson, J. a., Zhang, L., 2014. Climatically controlled formation of river terraces in a tectonically active region along the southern piedmont of the Tian Shan, NW China. Geomorphology 220, 15–29. doi:10.1016/j.geomorph.2014.05.024

Huntington, K.W., Ehlers, T.A., Hodges, K.V., and Whipp, D.M., 2007, Topography, exhumation pathway, age uncertainties, and the interpretation of thermochronometer data: Tectonics, v. 26.

Jain, M., Tandon, S.K., 2003. Fluvial response to Late Quaternary climate changes, western India. Quat. Sci. Rev. 22, 2223–2235. doi:10.1016/s0277-3791(03)00137-9

Jain, V., Sinha, R., 2005. Response of active tectonics on the alluvial Baghmati River, Himalayan foreland basin, eastern India. Geomorphology 70, 339–356. doi:10.1016/j.geomorph.2005.02.012

Jones, S.J., Arzani, N., Allen, M.B., 2014. Tectonic and climatic controls on fan systems: The Kohrud mountain belt, Central Iran. Sediment. Geol. 302, 29–43. doi:10.1016/j.sedgeo.2013.12.008

Jones, S.J., Frostick, L.E., Astin, T.R., 1999. Climatic and tectonic controls on fluvial incision and aggradation in the Spanish Pyrenees. J. Geol. Soc. London. 156, 761–769. doi:10.1144/gsjgs.156.4.0761

Jouanne, F., Mugnier, J.L., Gamond, J.F., Le Fort, P., Pandey, M.R., Bollinger, L., Flouzat, M., Avouac, J.P., 2004. Current shortening across the Himalayas of Nepal. Geophys. J. Int. 157, 1–14.

Koppes, M.N., Montgomery, D.R., 2009. The relative efficacy of fluvial and glacial erosion over modern to orogenic timescales. Nat. Geosci. 2, 644–647. doi:10.1038/ngeo616

Korschinek, G., Bergmaier, A., Faestermann, T., Gerstmann, U.C., Knie, K., Rugel, G., Wallner, A., Dillmann, I., Dollinger, G., von Gostomski, C.L., Kossert, K., Maiti, M., Poutivtsev, M., Remmert, A., 2010. A new value for the half-life of 10Be by Heavy-Ion Elastic Recoil Detection and liquid scintillation counting. Nucl. Instruments Methods Phys. Res. Sect. B Beam Interact. with Mater. Atoms 268, 187–191. doi:10.1016/j.nimb.2009.09.020

Kumar, R., Suresh, N., Sangode, S.J., Kumaravel, V., 2007. Evolution of the Quaternary alluvial fan system in the Himalayan foreland basin: Implications for tectonic and climatic decoupling. Quat. Int. 159, 6–20. doi:10.1016/j.quaint.2006.08.010

Kundu, B., Yadav, R.K., Bali, B.S., Chowdhury, S., Gahalaut, V.K., 2014. Oblique convergence and slip partitioning in the NW Himalaya: Implications from GPS measurements. Tectonics 33, 2013–2024. doi:10.1002/2014tc003633

Lal, D., 1991. Cosmic ray labeling of erosion surfaces: in situ nuclide production rates and erosion models. Earth Planet. Sci. Lett. 424–439.

Lave, J., Avouac, J.P., 2000. Active folding of fluvial terraces across the Siwaliks Hills, Himalayas of central Nepal. J. Geophys. Res. Earth 105, 5735–5770. doi:10.1029/1999jb900292

Le Fort, P., 1975. Himalaya: the collided range. Present knowledge of the continental arc. Am. J. Sci. 275A, 1–44.

Le Fort, P., 1981. Manaslu leucogranite: a collision signature of the Himalaya: a model for its genesis and emplacement. J. Geophys. Res. Solid Earth 86, 10545–10568.

Leech, M.L., Singh, S., Jain, A.K., Klemperer, S.L., Manickavasagam, R.M., 2005. The onset of India-Asia continental collision: Early, steep subduction required by the timing of UHP metamorphism in the western Himalaya. Earth Planet. Sci. Lett. 234, 83–97. doi:10.1016/j.epsl.2005.02.038

Leopold, L.B., Wolman, M.G., Miller, J.P., 2012. Fluvial processes in geomorphology. Courier Corporation.

Lupker, M., Blard, P.H., Lavé, J., France-Lanord, C., Leanni, L., Puchol, N., Charreau, J., Bourlès, D., 2012. 10Be-derived Himalayan denudation rates and sediment budgets in the Ganga basin. Earth Planet. Sci. Lett. 333-334, 146–156. doi:10.1016/j.epsl.2012.04.020

Lyon-Caen H, M.P., 1985. Gravity anomalies, flexure of Indian plate and the structure, support, and evolution of the Himalayan Ganga basin. Tectonics 513–538.

Macklin, M.G., Fuller, I.C., Lewin, J., Maas, G.S., Passmore, D.G., Rose, J., Woodward, J.C., Black, S., Hamlin, R.H.B., Rowan, J.S., 2002. Correlation of fluvial sequences in the Mediterranean basin over the last 200 ka and their relationship to climate change. Quat. Sci. Rev. 21, 1633–1641. doi:10.1016/s0277-3791(01)00147-0

Malik, J.N., Mohanty, C., 2007. Active tectonic influence on the evolution of drainage and landscape: Geomorphic signatures from frontal and hinterland areas along the Northwestern Himalaya, India. J. Asian Earth Sci. 29, 604–618. doi:10.1016/j.jseaes.2006.03.010

Mancktelow, N.S., and Grasemann, B., 1997, Time-dependent effects of heat advection and topography on cooling histories during erosion: Tectonophysics, v. 270, p. 167-195.

Marrero, S.M., Phillips, F.M., Borchers, B., Lifton, N., Aumer, R., Balco, G., 2016. Cosmogenic nuclide systematics and the CRONUScalc program. Quat. Geochronol. 31, 160–187.

Meigs, A., Burbank, D.W., and Beck, R.A., 1995, Middle-Late Miocene (pre-10 Ma) initiation of the Main Boundary Thrust in the western Himalaya: Geology, v. 23, p. 423-426.

Meigs, A.J., Burbank, D.W., Beck, R.A., 1995. Middle-Late Miocene (Greater-Than-10 Ma) Formation Of The Main Boundary Thrust In The Western Himalaya. Geology 23, 423–426. doi:10.1130/0091-7613(1995)023<0423:mlmmfo>2.3.co;2

Metivier, F., Gaudemer, Y., Tapponnier, P., Klein, M., 1999. Mass accumulation rates in Asia during the Cenozoic. Geophys. J. Int. 137, 280–318. doi:10.1046/j.1365-246X.1999.00802.x

Miller, T.K.., 1991. A model of stream channel adjustment: assessment of Rubey's hypothesis. J. Geol. 99, 699–710.

Molnar, P., 2004. Late cenozoic increase in accumulation rates of terrestrial sediment: How might climate change have affected erosion rates? Annu. Rev. Earth Planet. Sci. 32, 67–89. doi:10.1146/annurev.earth.32.091003.143456

Molnar, P., England, P., 1990. Late Cenozoic Uplift Of Mountain-Ranges And Global Climate Change - Chicken Or Egg. Nature 346, 29–34. doi:10.1038/346029a0

Montgomery, D.R., Brandon, M.T., 2002. Topographic controls on erosion rates in tectonically active mountain ranges. Earth Planet. Sci. Lett. 201, 481–489. doi:10.1016/s0012-821x(02)00725-2

Mukhopadhyay, D.K., Mishra, P., 1999. A balanced cross section across the Himalayan foreland belt, the Punjab and Himachal foothills: A reinterpretation of structural styles and evolution. Proc. Indian Acad. Sci. Planet. Sci. 108, 189–205.

Mukul, M., 2010. First-order kinematics of wedge-scale active Himalayan deformation: Insights from Darjiling-Sikkim-Tibet (DaSiT) wedge. J. Asian Earth Sci. 39, 645–657.

Mukul, M., Jaiswal, M., Singhvi, A.K., 2007. Timing of recent out-of-sequence active deformation in the frontal Himalayan wedge: Insights from the Darjiling sub-Himalaya, India. Geology 35, 999–1002. doi:10.1130/g23869a.1

Nábělek, J., Hetényi, G., Vergne, J., Sapkota, S., Kafle, B., Jiang, M., Su, H., Chen, J., Huang, B.-S., the Hi-Climb Team, 2009. Underplating in the Himalaya-Tibet Collision Zone Revealed by the Hi-CLIMB Experiment. Science (80-.). 325, 1371–1374.

Najman, Y., Bickle, M., Garzanti, E., Pringle, M., Barfod, D., Brozovic, N., Burbank, D., and Ando, S., 2009, Reconstructing the exhumation history of the Lesser Himalaya, NW India, from a multitechnique provenance study of the foreland basin Siwalik Group: Tectonics, v. 28, p. n/a-n/a.

Ni, J., Barazangi, M., 1984. Seismotectonics of the Himalayan Collision Zone: Geometry of the underthrusting Indian Plate beneath the Himalaya. J. Geophys. Res. Solid Earth 89, 1147–1163.

Olen, S.M., Bookhagen, B., Hoffmann, B., Sachse, D., Adhikari, D.P., Strecker, M.R., 2015. Understanding erosion rates in the Himalayan orogen: A case study from the Arun Valley. J. Geophys. Res. Earth Surf.

Olen, S.M., Bookhagen, B., Strecker, M.R., 2016. Role of climate and vegetation density in modulating denudation rates in the Himalaya. Earth Planet. Sci. Lett. 445, 57–67. doi:10.1016/j.epsl.2016.03.047

Owen, L.A., Finkel, R.C., Caffee, M.W., 2002. A note on the extent of glaciation throughout the Himalaya during the global Last Glacial Maximum. Quat. Sci. Rev. 21, 147–157. doi:10.1016/s0277-3791(01)00104-4

Pavlis, T.L., Hamburger, M.W., Pavlis, G.L., 1997. Erosional processes as a control on the structural evolution of an actively deforming fold and thrust belt: An example from the Pamir-Tien Shan region, central Asia. Tectonics 16, 810–822. doi:10.1029/97tc01414

Perg, L.A., Anderson, R.S., Finkel, R.C., 2001. Use of a new Be-10 and Al-26 inventory method to date marine terraces, Santa Cruz, California, USA. Geology 29, 879–882.

Pingel, H., Alonso, R.N., Mulch, A., Rohrmann, A., Sudo, M., Strecker, M.R., 2014. Pliocene orographic barrier uplift in the southern Central Andes. Geology 42, 691–694. doi:10.1130/g35538.1

Pinter, N., Keller, E.A., 1995. Geomorphological analysis of neotectonic deformation, northern Owens Valley, California. Geol. Rundschau 84, 200–212. doi:10.1007/BF00192251

Powers, P.M., Lillie, R.J., Yeats, R.S., 1998. Structure and shortening of the Kangra and Dehra Dun reentrants, sub-Himalaya, India. Geol. Soc. Am. Bull. 110, 1010–1027. doi:10.1130/0016-7606(1998)110<1010:sasotk>2.3.co;2

Prasad, B.R., Klemperer, S.L., Rao, V.V., Tewari, H.C., Khare, P., 2011. Crustal structure beneath the Sub-Himalayan fold--thrust belt, Kangra recess, northwest India, from seismic reflection profiling: Implications for Late Paleoproterozoic orogenesis and modern earthquake hazard. Earth Planet. Sci. Lett. 308, 218–228.

Pratt-Sitaula, B., Burbank, D.W., Heimsath, A., Ojha, T., 2004. Landscape disequilibrium on 1000–10,000 year scales Marsyandi River, Nepal, central Himalaya. Geomorphology 58, 223–241.

Raiverman V., Prasad DN, S.A.K., 1994. Structural style in northwestern Himalayan foothills. Himal. Geol. 263–280.

Ranga Rao, A., 1993. Magnetic-polarity stratigraphy of Upper Siwalik of north-western Himalayan foothills. Curr. Sci. 64, 863–873.

Rao, A.R., 1993. Magnetic-Polarity Stratigraphy Of Upper Siwalik Of North-Western Himalayan Foothills. Curr. Sci. 64, 863–873.

Ratschbacher, L., Frisch, W., Liu, G.H., Chen, C.S., 1994. Distributed Deformation In Southern And Western Tibet During And After The India-Asia Collision. J. Geophys. Res. Earth 99, 19917–19945. doi:10.1029/94jb00932

Ray, Y., Srivastava, P., 2010. Widespread aggradation in the mountainous catchment of the Alaknanda-Ganga River System: timescales and implications to Hinterland-foreland relationships. Quat. Sci. Rev. 29, 2238–2260. doi:10.1016/j.quascirev.2010.05.023

Raymo, M.E., Ruddiman, W.F., 1992. Tectonic Forcing Of Late Cenozoic Climate. Nature 359, 117–122. doi:10.1038/359117a0

Reiners, P.W., Brandon, M.T., 2006. Using thermochronology to understand orogenic erosion, in: Annual Review of Earth and Planetary Sciences. Annual Reviews, Palo Alto, pp. 419–466. doi:10.1146/annurev.earth.34.031405.125202

Reiners, P.W., Farley, K.A., and Hickes, H.J., 2002, He diffusion and (U-Th)/He thermochronometry of zircon: initial results from Fish Canyon Tuff and Gold Butte: Tectonophysics, v. 349, p. 297-308.

Repka, J.L., Anderson, R.S., Finkel, R.C., 1997. Cosmogenic dating of fluvial terraces, Fremont River, Utah. Earth Planet. Sci. Lett. 152, 59–73. doi:10.1016/s0012-821x(97)00149-0

Ritter, J.B., Miller, J.R., Enzel, Y., Wells, S.G., 1995. Reconciling the roles of tectonism and climate in Quaternary alluvial fan evolution. Geology 23, 245–248. doi:10.1130/0091-7613(1995)023<0245:RTROTA>2.3.CO;2

Robert, X., van der Beek, P., Braun, J., Perry, C., and Mugnier, J.-L., 2011, Control of detachment geometry on lateral variations in exhumation rates in the Himalaya: Insights from low-temperature thermochronology and numerical modeling: Journal of Geophysical Research: Solid Earth, v. 116, p. B05202.

Sah, M.P., Srivastava, R.A.K., 1992. Morphology and facies of the alluvial-fan sedimentation in the Kangra Valley, Himachal Himalaya. Sediment. Geol. 76, 23–42. doi:10.1016/0037-0738(92)90137-G

Schaller, M., Ehlers, T.A., Blum, J.D., Kallenberg, M.A., 2009. Quantifying glacial moraine age, denudation, and soil mixing with cosmogenic nuclide depth profiles. J. Geophys. Res. Earth Surf. 114.

Scherler, D., Bookhagen, B., Strecker, M.R., 2014. Tectonic control on 10 Be-derived erosion rates in the Garhwal Himalaya, India. J. Geophys. Res. Earth Surf. 119, 83–105. doi:10.1002/2013JF002955

Scherler, D., Bookhagen, B., Strecker, M.R., von Blanckenburg, F., Rood, D., 2010. Timing and extent of late Quaternary glaciation in the western Himalaya constrained by Be-10 moraine dating in Garhwal, India. Quat. Sci. Rev. 29, 815–831. doi:10.1016/j.quascirev.2009.11.031

Scherler, D., Bookhagen, B., Wulf, H., Preusser, F., Strecker, M.R., 2015. Increased late Pleistocene erosion rates during fluvial aggradation in the Garhwal Himalaya, northern India. Earth Planet. Sci. Lett. 428, 255–266. doi:10.1016/j.epsl.2015.06.034

Schiffman, C., Bali, B.S., Szeliga, W., and Bilham, R., 2013, Seismic slip deficit in the Kashmir Himalaya from GPS observations: Geophysical Research Letters, v. 40, p. 5642-5645.

Schildgen, T.F., Cosentino, D., Bookhagen, B., Niedermann, S., Yildirim, C., Echtler, H., Wittmann, H., Strecker, M.R., 2012. Multi-phased uplift of the southern margin of the Central Anatolian plateau, Turkey: A record of tectonic and upper mantle processes. Earth Planet. Sci. Lett. 317-318, 85–95.

Schildgen, T.F., Robinson, R.A.J., Savi, S., Phillips, W.M., Spencer, J.Q.G., Bookhagen, B., Scherler, D., Tofelde, S., Alonso, R.N., Kubik, P.W., others, 2016. Landscape response to late Pleistocene climate change in NW Argentina: Sediment flux modulated by basin geometry and connectivity. J. Geophys. Res. Earth Surf. 121, 392–414.

Schwanghart Scherler, D., W., 2014. TopoToolbox 2 – MATLAB-based software for topographic analysis and modeling in Earth surface sciences. Earth Surf. Dyn. 2, 1–7.

Schwanghart Scherler, D.W., 2014. TopoToolbox 2 – MATLAB-based software for topographic analysis and modeling in Earth surface sciences. Earth Surf. Dyn. 2, 1–7.

Searle, M., Corfield, R.I., Stephenson, B., McCarron, J., 1997. Structure of the North Indian continental margin in the Ladakh-Zanskar Himalayas: Implications for the timing of obduction of the Spontang ophiolite, India-Asia collision and deformation events in the Himalaya. Geol. Mag. 134, 297–316. doi:10.1017/s0016756897006857

Searle, M.P., Cooper, D.J.W., Rex, A.J., 1988. Collision Tectonics Of The Ladakh Zanskar Himalaya. Philos. Trans. R. Soc. a-Mathematical Phys. Eng. Sci. 326, 117–140. doi:10.1098/rsta.1988.0082

Shreve, R.L., 1968. Leakage and fluidization in air-layer lubricated avalanches. Bull. Geol. Soc. Am. 79, 653–658. doi:10.1130/0016-7606(1968)79[653:LAFIAL]2.0.CO;2

Singh, A.K., Parkash, B., Mohindra, R., Thomas, J. V, Singhvi, A.K., 2001. Quaternary alluvial fan sedimentation in the Dehradun Valley Piggyback Basin, NW Himalaya: Tectonic and palaeoclimatic implications. Basin Res. 13, 449–471.

Singh, T., Awasthi, A.K., Caputo, R., 2012. The sub-Himalayan fold-thrust belt in the 1905 Kangra earthquake zone: A critical taper model perspective for seismic hazard analysis. Tectonics 31.

Sinha, R., Kumar, R., Sinha, S., Tandon, S.K., Gibling, M.R., 2007. Late Cenozoic fluvial successions in northern and western India: an overview and synthesis. Quat. Sci. Rev. 26, 2801–2822. doi:10.1016/j.quascirev.2007.07.018

Sinha, S., Suresh, N., Kumar, R., Dutta, S., Arora, B.R., 2010. Sedimentologic and geomorphic studies on the Quaternary alluvial fan and terrace deposits along the Ganga exit. Quat. Int. 227, 87–103. doi:10.1016/j.quaint.2009.09.015

Snyder, N.P., Whipple, K.X., Tucker, G.E., Merritts, D.J., 2000. Landscape response to tectonic forcing: Digital elevation model analysis of stream profiles in the Mendocino triple junction region, northern California. Geol. Soc. Am. Bull. 112, 1250–1263. doi:10.1130/0016-7606(2000)112<1250:lrttfd>2.3.co;2

Srivastava, P., Rajak, M.K., Singh, L.P., 2009. Late Quaternary alluvial fans and paleosols of the Kangra basin, NW Himalaya: Tectonic and paleoclimatic implications. Catena 76, 135–154. doi:10.1016/j.catena.2008.10.004

Srivastava, P., Tripathi, J.K., Islam, R., Jaiswal, M.K., 2008. Fashion and phases of late Pleistocene aggradation and incision in the Alaknanda River Valley, western Himalaya, India. Quat. Res. 70, 68–80.

Steck, A., 2003. Geology of the NW Indian Himalaya. Eclogae Geol. Helv. 96, 147–U13. doi:10.1007/s00015-003-1091-4

Steck, A., Spring, L., Vannay, J.C., Masson, H., Stutz, E., Bucher, H., Marchant, R., Tieche, J.C., 1993. Geological Transect Across The Northwestern Himalaya In Eastern Ladakh And Lahul (A Model For The Continental Collision Of India And Asia). Eclogae Geol. Helv. 86.

Stevens, V., and Avouac, J., 2015. Interseismic coupling on the main Himalayan thrust: Geophys Res Lett, v. 42, p. 5828 - 5837.

Stolar, D.B., Willett, S.D., Roe, G.H., 2006. Climatic and tectonic forcing of a critical orogen. Geol. Soc. Am. Spec. Pap. 398, 241–250.

Stone, J.O., 2000. Air pressure and cosmogenic isotope production. J. Geophys. Res. Earth 105, 23753–23759. doi:10.1029/2000jb900181

Strecker, M.R., Hilley, G.E., Arrowsmith, J.R., Coutand, I., 2003. Differential structural and geomorphic mountain-front evolution in an active continental collision zone: The northwest Pamir, southern Kyrgyzstan. Bull. Geol. Soc. Am. 115, 166–181. doi:10.1130/0016-7606(2003)115<0166:DSAGMF>2.0.CO;2

Stübner, K., Drost, K., Schoenberg, R., Böhme, M., Starke, J., & Ehlers, T. A., 2016. Asynchronous timing of extension and basin formation in the South Rhodope core complex, SW Bulgaria, and northern Greece. *Tectonics*, *35*(1), 136-159

Stuwe, K., White, L., and Brown, R., 1994. The Influence of Eroding Topography on Steady-State Isotherms - Application to Fission-Track Analysis: Earth and Planetary Science Letters, v. 124, p. 63-74.

Suresh, N., Bagati, T.N., Kumar, R., Thakur, V.C., 2007. Evolution of Quaternary alluvial fans and terraces in the intramontane Pinjaur Dun, Sub-Himalaya, NW India: interaction between tectonics and climate change. Sedimentology 54, 809–833. doi:10.1111/j.1365-3091.2007.00861.x

Tandon, S.K., Kumar, R., Singh, P., 1984. Syntectonic Controls Of Paleoflow Reversals And Variability - Sediment-Vector Sequences In The Late Orogenic Fluvial Siwalik Basin, Panjab Sub-Himalaya, India. Sediment. Geol. 41, 97–112. doi:10.1016/0037-0738(84)90004-6

Thakur, V.C., Joshi, M., Sahoo, D., Suresh, N., Jayangondapermal, R., and Singh, A., 2014, Partitioning of convergence in Northwest Sub-Himalaya: estimation of late Quaternary uplift and convergence rates across the Kangra reentrant, North India: International Journal of Earth Sciences, v. 103, p. 1037-1056.

Thakur, V.C., Pandey, A.K., Suresh, N., 2007. Late Quaternary-Holocene evolution of Dun structure and the Himalayan Frontal Fault zone of the Garhwal Sub-Himalaya, NW India. J. Asian Earth Sci. 29, 305–319. doi:10.1016/j.jseaes.2006.02.002

Thiede, R.C., Arrowsmith, J.R., Bookhagen, B., McWilliams, M.O., Sobel, E.R., Strecker, M.R., 2005. From tectonically to erosionally controlled development of the Himalayan orogen. Geology 33, 689–692. doi:10.1130/g21483.1

Thiede, R.C., Bookhagen, B., Arrowsmith, J.R., Sobel, E.R., Strecker, M.R., 2004. Climatic control on rapid exhumation along the Southern Himalayan Front. Earth Planet. Sci. Lett. 222, 791–806. doi:10.1016/j.epsl.2004.03.015

Thiede, R.C., Ehlers, T.A., 2013. Large spatial and temporal variations in Himalayan denudation. Earth Planet. Sci. Lett. 371, 278–293. doi:10.1016/j.epsl.2013.03.004

Thiede, R.C., Ehlers, T.A., Bookhagen, B., and Strecker, M.R., 2009, Erosional variability along the northwest Himalaya: Journal of Geophysical Research-Earth Surface, v. 114, p. 19.

Valdiya, K.S., 1980. The 2 Intracrustal Boundary Thrusts Of The Himalaya. Tectonophysics 66, 323–348. doi:10.1016/0040-1951(80)90248-6

Valdiya, K.S., 1991. Quaternary Tectonic History of Northwest Himalaya. Curr. Sci. 61, 664–668.

Valla, P.G., van der Beek, P.A., and Braun, J., 2011, Rethinking low-temperature thermochronology data sampling strategies for quantification of denudation and relief histories: A case study in the French western Alps: Earth and Planetary Science Letters, v. 307, p. 309-322.

Vance, D., Bickle, M., Ivy-Ochs, S., Kubik, P.W., 2003. Erosion and exhumation in the Himalaya from cosmogenic isotope inventories of river sediments. Earth Planet. Sci. Lett. 206, 273–288. doi:10.1016/S0012-821X(02)01102-0

Vannay, J.C., Grasemann, B., 2001. Himalayan inverted metamorphism and syn-convergence extension as a consequence of a general shear extrusion. Geol. Mag. 138, 253–276.

Viseras, C., Calvache, M.L., Soria, J.M., Fernandez, J., 2003. Differential features of alluvial fans controlled by tectonic or eustatic accommodation space. Examples from the Betic Cordillera, Spain. Geomorphology 50, 181–202. doi:10.1016/s0169-555x(02)00214-3

von Blanckenburg, F., 2005. The control mechanisms of erosion and weathering at basin scale from cosmogenic nuclides in river sediment. Earth Planet. Sci. Lett. 237, 462–479. doi:10.1016/j.epsl.2005.06.030

Wallace, K., Bilham, R., Blume, F., Gaur, V.K., Gahalaut, V., 2005. Surface deformation in the region of the 1905 Kangra Mw=7.8 earthquake in the period 1846-2001. Geophys. Res. Lett. 32. doi:10.1029/2005gl022906

Wang, Y., Cheng, H., Edwards, R.L., Kong, X., Shao, X., Chen, S., Wu, J., Jiang, X., Wang, X., An, Z., 2008. Millennial- and orbital-scale changes in the East Asian monsoon over the past 224,000 years. Nature 451, 1090–3.

Wang, Y.J., Cheng, H., Edwards, R.L., An, Z.S., Wu, J.Y., Shen, C.C., Dorale, J.A., 2001. A high-resolution absolute-dated Late Pleistocene monsoon record from Hulu Cave, China. Science (80-.). 294, 2345–2348. doi:10.1126/science.1064618

Wang, Y.J., Cheng, H., Edwards, R.L., He, Y.Q., Kong, X.G., An, Z.S., Wu, J.Y., Kelly, M.J., Dykoski, C.A., Li, X.D., 2005. The Holocene Asian monsoon: Links to solar changes and North Atlantic climate. Science (80-). 308, 854–857. doi:10.1126/science.1106296

Webb, A.A.G., 2013, Preliminary balanced palinspastic reconstruction of Cenozoic deformation across the Himachal Himalaya (northwestern India): Geosphere, v. 9, p. 572-587.

Webb, A.A.G., Yin, A., Harrison, T.M., Celerier, J., Gehrels, G.E., Manning, C.E., and Grove, M., 2011, Cenozoic tectonic history of the Himachal Himalaya (northwestern India) and its constraints on the formation mechanism of the Himalayan orogen: Geosphere, v. 7, p. 1013-1061.

Wegmann, K.W., Pazzaglia, F.J., 2009. Late Quaternary fluvial terraces of the Romagna and Marche Apennines, Italy: Climatic, lithologic, and tectonic controls on terrace genesis in an active orogen. Quat. Sci. Rev. 28, 137–165. doi:10.1016/j.quascirev.2008.10.006

Wesnousky, S.G., Kumar, S., Mohindra, R., Thakur, V.C., 1999. Uplift and convergence along the Himalayan frontal thrust of India. Tectonics 18, 967–976. doi:10.1029/1999tc900026

Whipple, K.X., 2009. The influence of climate on the tectonic evolution of mountain belts. Nat. Geosci. 2, 97–104. doi:10.1038/ngeo413

Whipple, K.X., Tucker, G.E., 1999. Dynamics of the stream-power river incision model: Implications for height limits of mountain ranges, landscape response timescales, and research needs. J. Geophys. Res. Earth 104, 17661–17674. doi:10.1029/1999jb900120

Wiesmayr, G., Grasemann, B., 2002. Eohimalayan fold and thrust belt: Implications for the geodynamic evolution of the NW-Himalaya (India). Tectonics 21. doi:10.1029/2002tc001363

Willett, S.D., 1999. Orogeny and orography: The effects of erosion on the structure of mountain belts. J. Geophys. Res. Earth 104, 28957–28981. doi:10.1029/1999jb900248

Willett, S.D., Beaumont, C., others, 1994. Subduction of Asian lithospheric mantle beneath Tibet inferred from models of continental collision. Nature 369, 642–645.

Wobus, C., Heimsath, A.M., Whipple, K., Hodges, K. V, 2005. Active out-of-sequence thrust faulting in the central Nepalese Himalaya. Nature 434, 1008–1011.

Wobus, C.W., Tucker, G.E., Anderson, R.S., 2006. Self-formed bedrock channels. Geophys. Res. Lett. 33. doi:10.1029/2006gl027182

Wulf, H., Bookhagen, B., Scherler, D., 2010. Seasonal precipitation gradients and their impact on fluvial sediment flux in the Northwest Himalaya. Geomorphology 118, 13–21.

Yeats, R.S., Thakur, V.C., 1998. Reassessment of earthquake hazard based on a fault-bend fold model of the Himalayan plate-boundary fault. Curr. Sci. 74, 230–233.

Yildirim, C., Schildgen, T.F., Echtler, H., Melnick, D., Bookhagen, B., Ciner, A., Niedermann, S., Merchel, S., Martschini, M., Steier, P., Strecker, M.R., 2013. Tectonic implications of fluvial incision and pediment deformation at the northern margin of the Central Anatolian Plateau based on multiple cosmogenic nuclides. Tectonics 32, 1107–1120. doi:10.1002/tect.20066

Yin, A., 2006. Cenozoic tectonic evolution of the Himalayan orogen as constrained by along-strike variation of structural geometry, exhumation history, and foreland sedimentation. Earth-Science Rev. 76, 1–131. doi:10.1016/j.earscirev.2005.05.004

Yin, A., Dubey, C.S., Kelty, T.K., Gehres, G.E., Chou, C.Y., Grove, M., and Lovera, O., 2006, Structural evolution of the Arunachal Himalaya and implications for asymmetric development of the Himalayan orogen: Curr Sci, v. 90, p. 195-206.

Yin, A., Harrison, T.M., 2000. Geologic evolution of the Himalayan-Tibetan orogen. Annu. Rev. Earth Planet. Sci. 28, 211–280. doi:10.1146/annurev.earth.28.1.211

Zechar, J.D., Frankel, K.L., 2009. Incorporating and reporting uncertainties in fault slip rates. J. Geophys. Res. Solid Earth 114.

Appendix 1: Supplementary material for chapter 3

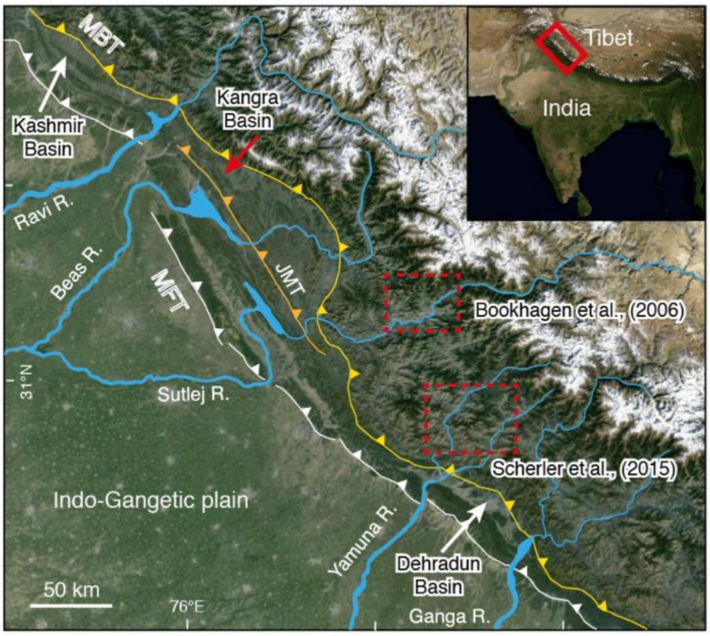

Figure S3.1: *An overview satellite image of the Northwestern Himalaya showing major drainages and intermontane basins, as well as the major thrusts defining the Sub-Himalayan belt. Holocene incision history in the Kangra Basin (this study) is similar with that in the Sutlej valley (Bookhagen et al., 2006).*

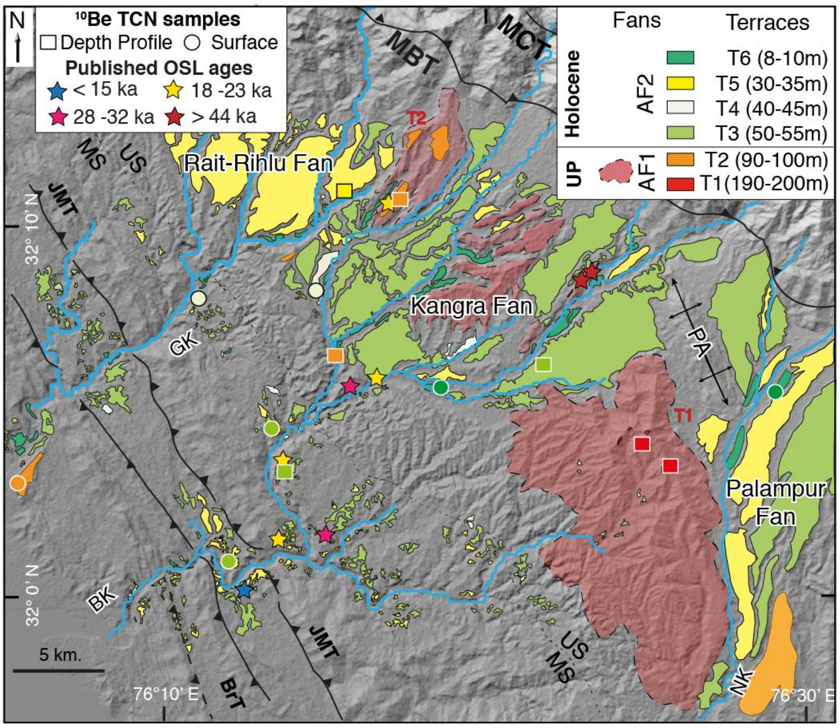

Figure S3.2: *Terrace map of the study area with sample locations for TCN surface-exposure dating.*

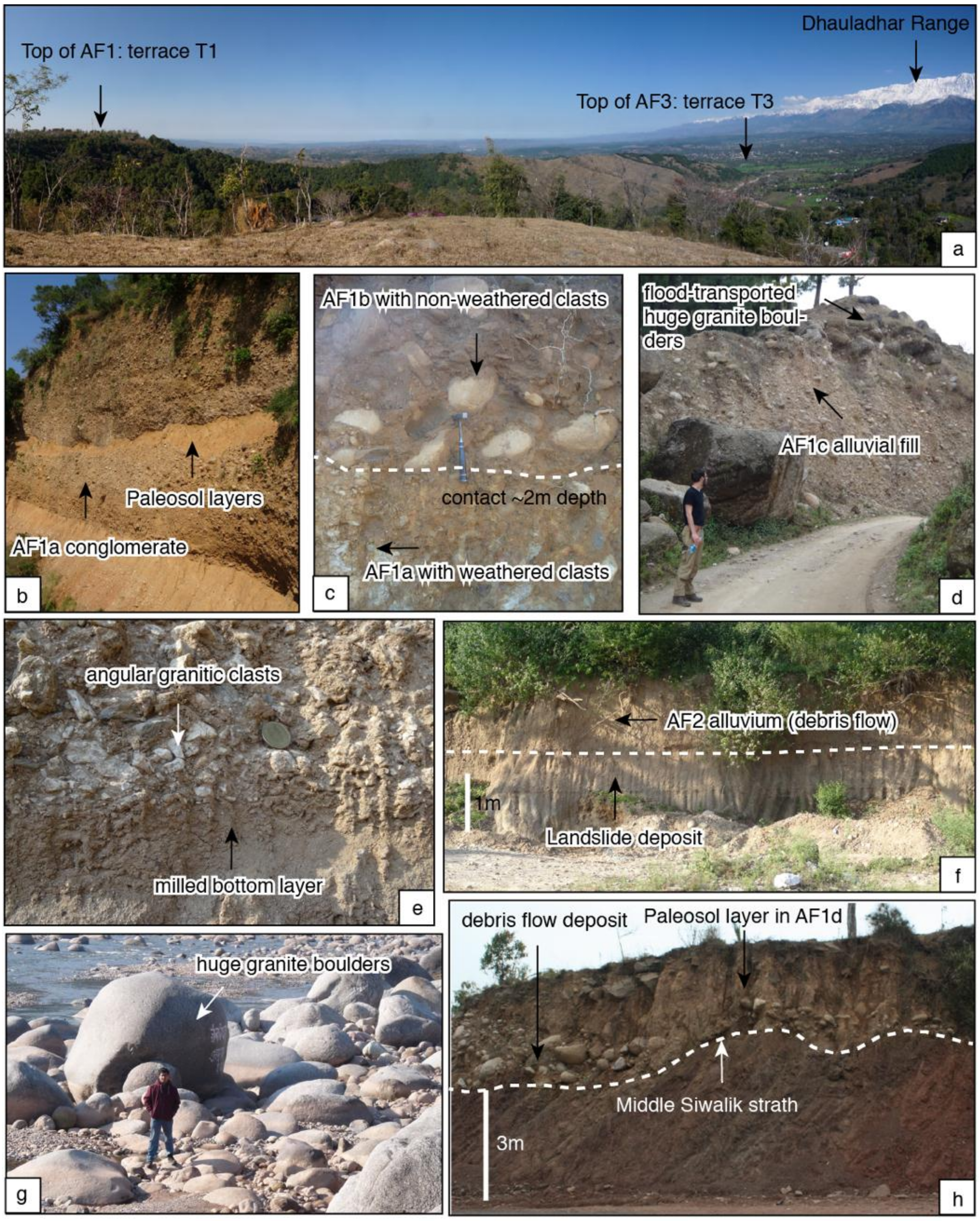

Figure S3.3*: Field photographs. (a) T1 terrace level exposed near south of Paror anticline, nearly 200m-high from the riverbed and the Dhauladhar Range is in the background. (b) Loess or paleosol layers within the conglomeratic alluvial fill from Af1a aggradation phase. (c) Evidence of different aggradation phases below the T1 surface. The lower fill (AF1a) consists of most-weathered granites and the upper fill, AF1b (0.3- 3m in thickness in most places) consists of pristine quartzite clasts. (d) Presence of large granitic boulders (>1m diameter) of Af2 phase on top of the Af1c alluvium. (e) Landslide deposit within AF2 fill recognized by characteristic angular clasts and milled bottom layer. (f) Outcrop view of the landslide deposit overlain by debris flow deposit constituting the AF2 fill. (g) Huge granite boulders in the Gaj Khad riverbed indicating high energy flood deposition in recent times. (h) AF1d alluvium above the Middle Siwalik strath where the fill constitutes debris flow deposits as well as ~1m thick paleosol layer.*

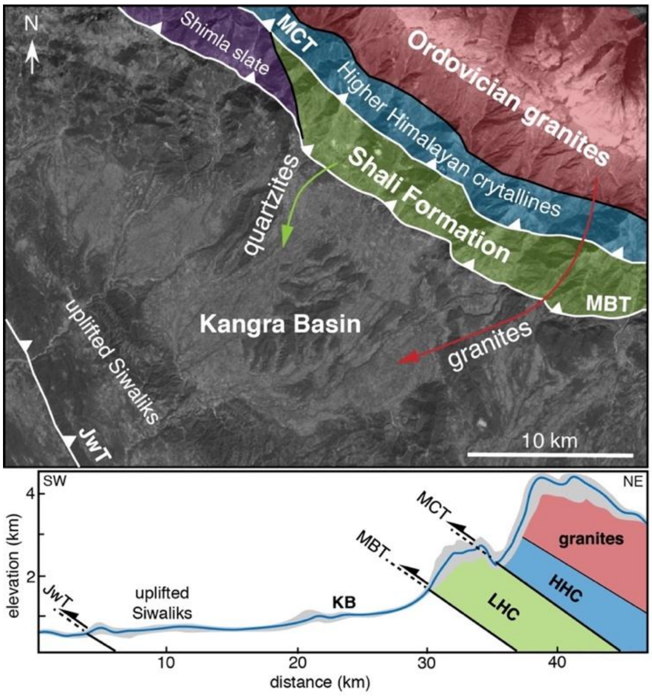

Figure S3.4: *Sources of sediments of the Kangra Basin from the Main Himalayan orogen (modified after Steck et al., 2003). The topographic swath perpendicular to the strike of the mountain front shows elevation differences (hints about difference in surface production rates or cosmogenic inheritance) of the sources.*

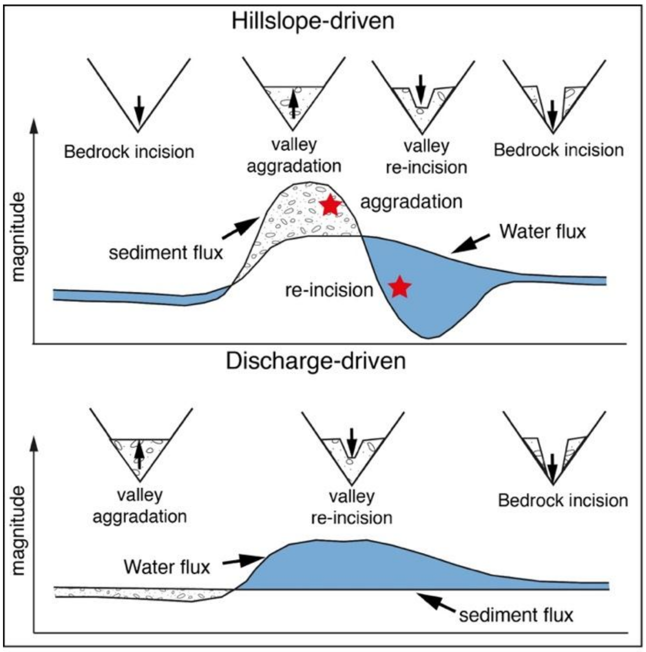

Figure S3.5: *Models for aggradation and incision of valley-fills based on hillslope and discharge (modified after Scherler et al., 2015), suggesting changes in the sediment cycle based on relative changes in sediment and water flux. The red stars denote two situations – in case 1, the sediment flux outbalances the water flux hence the valley aggrades; while, in case 2- the water flux is more than sediment flux, hence the valley-fills are incised. Discharge-driven model assumes a constant sediment flux, which may not be true for this case study.*

Appendix 2: Supplementary material for chapter 4

The supporting information for chapter 4 of this thesis contains additional information on the method of in-situ CRN sampling techniques and calculation of age, as well as method of composite stream and terrace profile analysis for calculation of terrace offset:

Surface exposure dating of terraces using depth profiles of in-situ ^{10}Be

Determining the exposure ages of fluvial fill terraces poses a challenge because the inherited concentration of cosmogenic radionuclides (CRNs) must be determined and then subtracted from the surface concentration in order to evaluate the correct exposure ages. For a single alluvial fill, it is assumed that the inheritance is similar for each depth beneath the surface and that deposition of the fill unit was fast compared to the surface exposure age (e.g., Repka et al., 1997). The CRN concentration decreases exponentially with depth according to the following relationship (in this case ignoring nuclide decay, as time (t) is negligible compared to the half-life of ^{10}Be, i.e. 1.39 Ma, (Chmeleff et al., 2010; Korschinek et al., 2010) is

$$C(z) = P0.e^{\left(-\frac{z\rho}{\Lambda}\right)t} + Ci \quad (1)$$

where $C(z)$ (atoms. g^{-1}) is the measured concentration at any depth z after an exposure time t. P_0 is the production rate at the surface, Λ is the attenuation length (160±5 g.cm^{-2} for neutron spallation) (Dunne et al., 1999), ρ is the density of the material (g.cm^{-3}) and Ci is the nuclide inheritance (atoms. g^{-1}).

Monte Carlo simulations of CRN concentrations within a depth profile enable us to evaluate the inheritance as well as the surface concentration of an alluvial fill unit (Hidy et al., 2010). For depth profiles, we have used an amalgamation method (Repka et al., 1997), whereby we have collected >20 to 30 clasts per horizon from 5 to 8 different depth intervals within pits excavated into the tops of fill units. CRN depth profiles show deviations from the expected exponential profile if there was mixing of the deposit (e.g., due to bioturbation or anthropogenic impacts), non-uniform inheritance with depth, or a depositional hiatus some time prior to the exposure of the top surface. A sample from the mixed layer would yield a lower concentration than the modelled concentration at that depth if material of higher concentration has been mixed with it (Granger and Riebe, 2007).

Another important factor for CRN age calculation is the surface production rate scaling scheme and the sea level high-latitude (SLHL) reference production rate. In this study, we have used 4.01 atoms. g^{-1}.a^{-1} as a reference SLHL production rate for ^{10}Be (Borchers et al., 2016) for age calculation and time-dependent spallogenic production model after Lal (1991) and Stone (2000). Previously, many studies have used a higher SLHL referenced production rate (4.5 to 4.7 atoms.g^{-1}.a^{-1}), which results in ages that are 15-20% younger compared to those calculated with this updated reference production rate. Depth-profile simulations after Hidy et al., (2010) are done using time-independent spallogenic production model after Lal (1991) and Stone (2000). Model surface concentrations (using the best fit line) and inheritance (with uncertainty) were obtained from each depth profile. The difference between the model surface concentration and inheritance gives the post-depositional ^{10}Be accumulation, which was used in the CRONUScalc program (Marrero et al., 2016). This allows transformation of the time-independent (St) ages to time-dependent or (Lm) ages.

We present four depth profiles from different terrace surfaces levels in the Kangra Basin. The depth-profile simulations are generated using the procedures described by Hidy et al., (2010). For the Monte-Carlo simulations, we used several key parameters that were determined in connection with our field observations, the most important of which involves potential bioturbation or anthropogenic activities.

Most of the terraces in the Kangra region have been cultivated over centuries. In our sample site selection, we tried to avoid modern day cultivation fields. Although we cannot rule out past agricultural cultivation of our sample sites, the depth-profile results suggest that there has been no significant mixing of sediments. Importantly, even now, people in the area do not use heavy machineries for agriculture even now, so anthropogenic impact below 10-15 cm is unlikely. In all depth profile locations, we observed only a thin soil cover of 10 to 20 cm above well rounded boulders. This thin soil layer is sandy and contains quartz clasts of 2 to 3 cm diameter. In our study area, we did not encounter any areas where thinker soils are preserved. For this reason, we have performed our Monte Carlo simulations assuming 0 to 20 cm of total surface erosion (the "erosional threshold").

Table S 4.1:GPS points projected to N50°E azimuth line to calculate offset of T3

Latitude(°)	Longitude(°)	Upstream distance from JMT(km)	Elevation (m)	Error in elevation (m)
32.06111	76.22889	2.6	626	3
32.05722	76.22722	2.3	617	2
32.07194	76.22694	3.2	639	2
32.08167	76.23694	4.2	649	3
32.06611	76.23194	3.15	639	2
32.07722	76.23004	3.4	643	1
32.02313	76.2507	1.5	607	2
32.01111	76.21333	-0.9	530	2
32.01417	76.21722	-0.6	535	1
32.01806	76.20583	-1.25	527	2
32.02056	76.20833	-0.85	534	3
32.01889	76.21001	-1.1	529	1
32.01751	76.20503	-1.5	523	2

Table S4.1*: Multiple point-averaged hand-held GPS measurements projected to a N50°E azimuth and the elevations plotted against upstream distance from the trace of the JMT.*

Composite stream and terrace profile: An indicator of active tectonics

Geomorphic markers are useful for quantifying the offset across a given structure, and if the markers can be dated, they can reveal average offset rates (Lave and Avouac, 2000). Fluvial terraces that cross active structures are particularly well suited for this purpose. Measuring the vertical offset of a dated terrace would yield the surface uplift rate of the fault since the terrace formed. If the fault geometry is known, the surface uplift rate can be used to evaluate the slip rate and the shortening rate across the fault (Thakur et al., 2014).

Methodology

Terrace identification and allocation was initially performed by analyzing satellite-derived digital elevation models; further control on the spatial distribution was achieved by field observations including hand-held GPS measurements, on-site measurement of terrace heights, and Google Earth satellite image analysis. For this study, we used 30-m resolution Cartosat 1 data for the stream profile and terrace profile analysis. Our procedure for extracting terrace extents and terrace profiles along the Baner Khad is described in the main text. To derive an independent constraint on the terrace heights, we measured multiple point-averaged elevation data from GPS measurements and DEM data. The average of the GPS elevation data from terrace T3 (the best preserved terrace in this area that crosses the Jwalamukhi thrust) has been used to define the mean terrace elevation, whereas the range of elevation values define the uncertainty. The GPS points are listed in Table S 4.1.

Appendix 3: Supplementary material for chapter 5

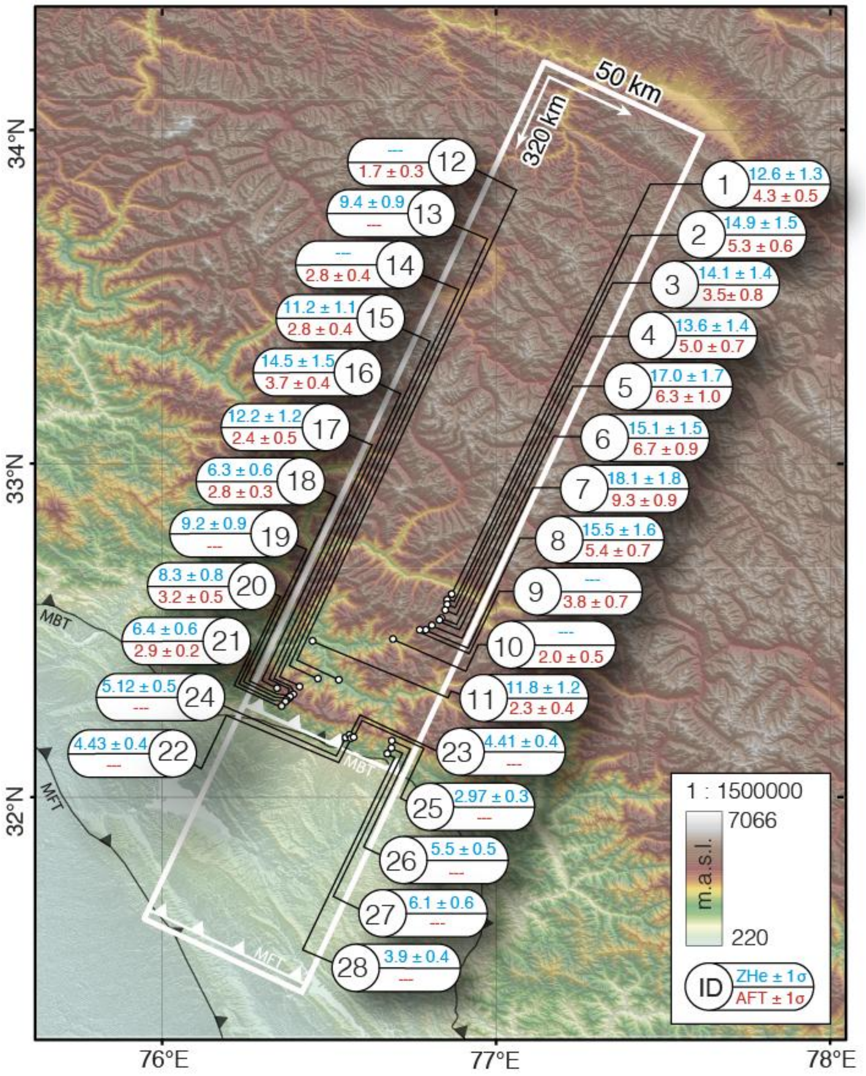

Figure S5.1: *Sample locations and obtained mineral cooling ages from the Dhauladhar range and Pir Panjal range. ZHe and AFT ages are compiled from this study and Deeken et al., (2011).*

Analytical details

Zircon (U-Th/He)-dating

Standard mineral separation procedures were conducted at the University of Potsdam. All samples yield high quantity of Zircon-phenocrysts. By handpicking sufficient sized and pristine zircon grains (80-150 µm) were screened for large inclusions, cracks and their state of alteration using a binocular microscope magnification. The grain dimensions were measured for the calculation of the alpha-correction factor after Farley et al. (1996). Afterwards the single grains were packed in Nb-tubes for U-Th/He analysis and measured at the University of Tübingen using a Patterson Helium extraction line, which is equipped with a 960nm diode laser to extract the helium gas. After Helium analysis the grain packages was dissolved for U, Th, and Sm measurements using an ICP-MS. At least three aliquot replicates per sample have been analyzed.

The analytical error of the mass spectrometer measurements are generally very low and do not exceed 2%. In contrast, the reproducibility of the sample age constitutes a much larger error. We therefore report the mean U-Th/He age and the standard deviation of the measured aliquots as the sample error. For single grain ages we apply a 3% 1-sigma-error-based on the reproducibility of standard measurements in the lab.

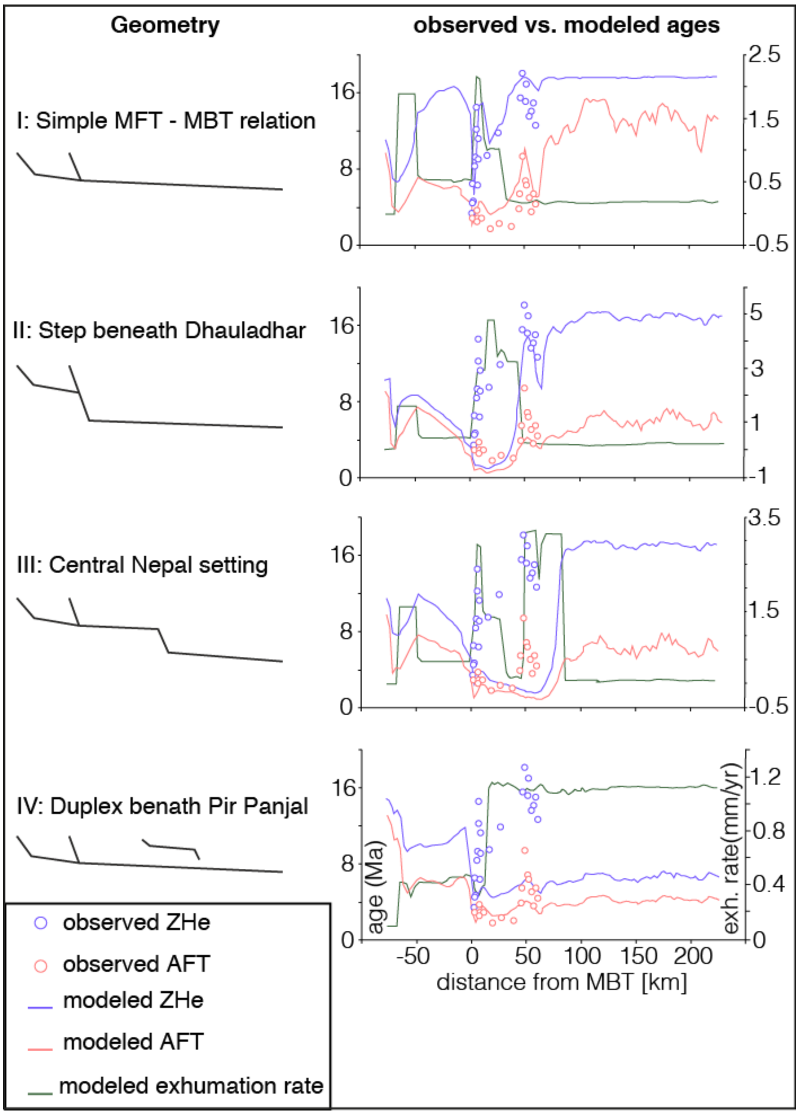

Figure S5.2: Comparison between the observed (dots) ages and the predicted (lines) ages of each thermochronometer (right column). On the left column the particular inferred subsurface geometries are shown. Note, that the dots represent each measured data point, while the lines show the predicted mean age over the whole model width (50 km) at the sample point location. This was done to allow a fast evaluation of the complete model area with just a small data input.

PECUBE forward and inversion modeling

For the model runs we divided the model timing into four subsequent steps. This was consistent for all inversions. The first step acts just as the overlapping, i.e. the pre-activity-phase and should allow the complete relaxations for all isotherms. The second step represents the warm-up-stage, where the MBT-activation is slowly established. The third step ensures a steady acceleration of the fault's slip rate and last but not least, the fourth step gives the assumed recent slip rate on the MBT.

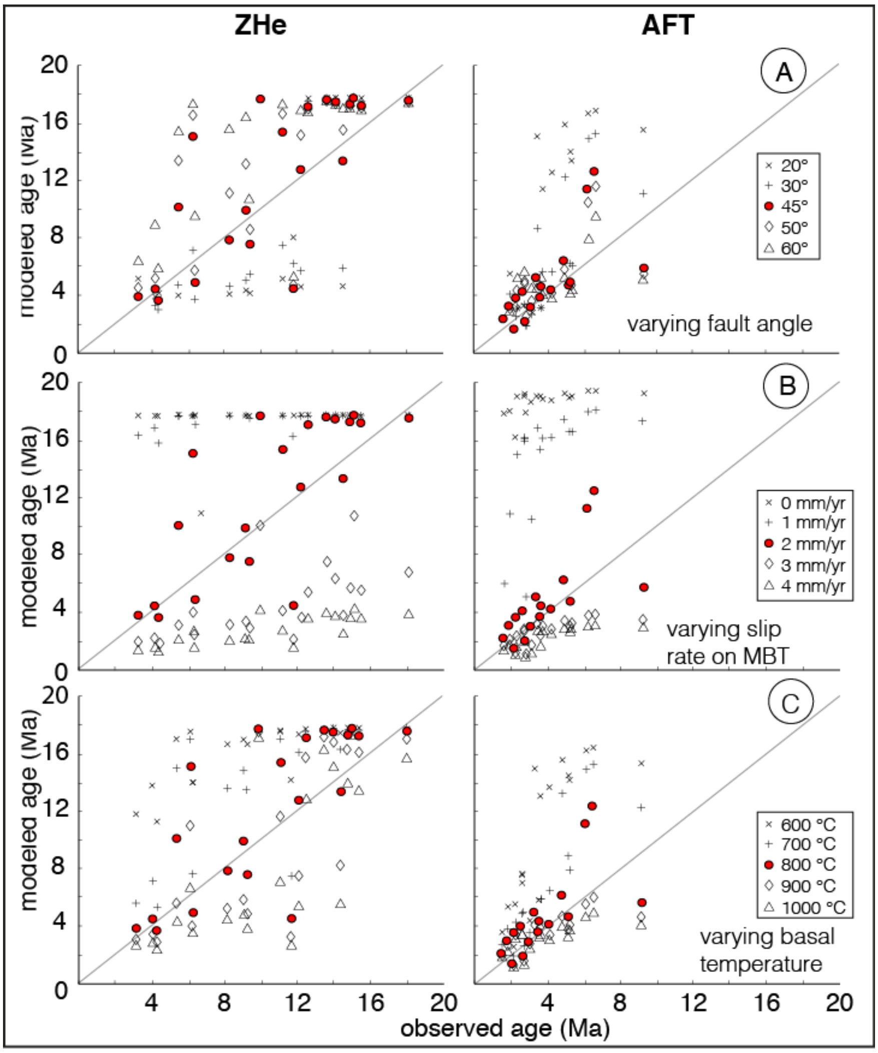

Figure S5.3: Results of observed vs. modelled ages obtained by varying one parameter at a time, while the others remain constant. The red dots denote the lowest misfit between the observed vs. modelled ages.

Modelling Parameters:

To model the thermal evolution of Himalayan mountain front along Dhauladhar Range segment and its test different models of the related kinematics since the Miocene, we used 320 km x 50 km wide spatial window and test this. Based on published balanced cross section and other structural information we could reconstruct depth and extent of the MHT (e.g. Powers et al., 1998; Schulte-Pelkum et al., 2005). Although PECUBE is a powerful tool to examine the 3D subsurface thermal structure and its evolution, all results has to be interpreted with caution, as several factors can strongly influence the obtained results, such as spatial modelling resolution, number of free parameters and the misfit between observed and predicted values (Braun et al., 2012). Also the spatial distribution of the initial models and their amount govern, in which way and which timing the NA approximates a particular minimum misfit area. An insufficient distribution could lead to a unidirectional approximation within the parameter space. Therefore, the initial random sampling has to be executed as uniform as possible. Also the fact, that the initial sampling is executed randomly, should state, that there is a demand to perform at least more than one model per setting, to evaluate the obtained results. Last, the chosen subsurface geometry and its interlinking play an important role for the model behavior concerning the way a particle trajectory could take. And this in turn controls, how fast and in which pattern a closure temperature isotherm gets deformed by advection. After the determination of the meaningful spatial boundaries, the overall modeling procedure comprises at least four steps. Within the first step, an appropriate subsurface geometry has to be found, to produce a first approximation on reliable surface age patterns, which coincide with the present surface topography. I used the most reliable geometry to go further with. Once we found a meaningful parameter combination out of the conducted forward model runs, the obtained values were taken as the basis for the following inverse model runs. The inversion process itself is described in detail in chapter 5.4.3.1.

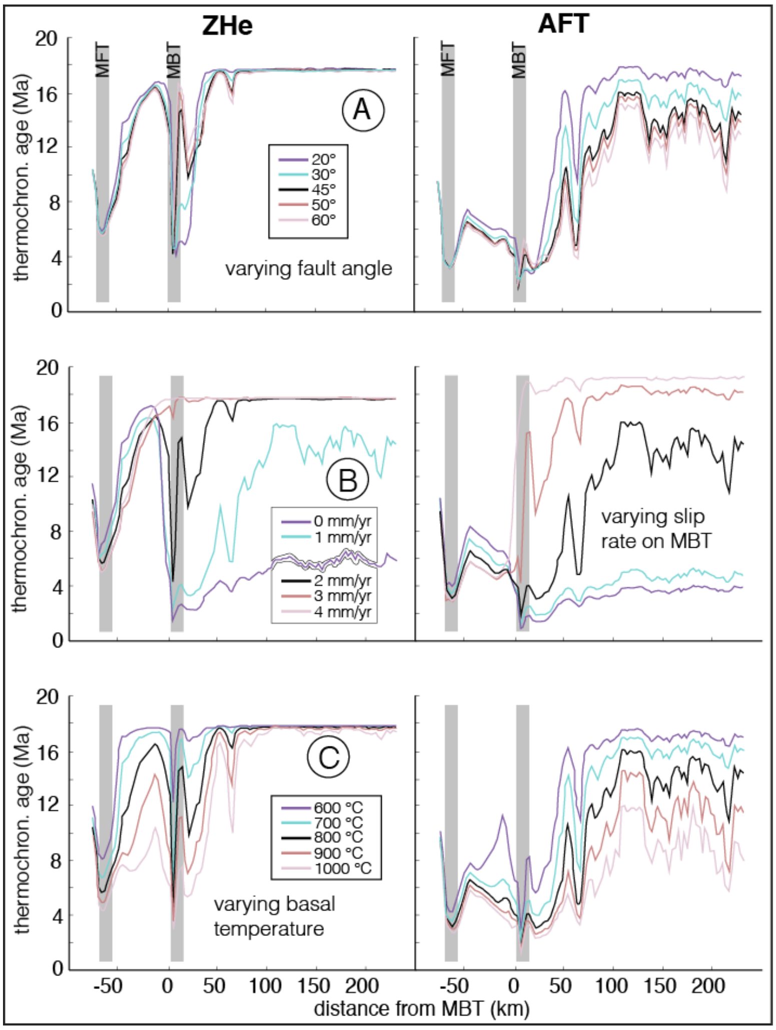

Figure S5.4: Comparison of observed vs. modelled ages based on variations of a single parameter space. These plots define the model-wide sensitivity of changing the influx parameter.

Spatial boundaries and model resolution

The Model was executed within a 50 km per 320 km elongated rectangular frame, which trend goes 25° to the NNE (Figure 14). We chose these values in order to fulfill simplicity requirements for geodynamic modeling, which are in our case: (1) The model width reflects the most linear part of the central Dhauladhar range, its bounding faults, and most analyzed cooling ages are located. (2) The code PECUBE in its simplest version just allows runs orthogonal to the fault's surface trace, which strikes 115° ESE in our case. (3) The length supplies our model with enough material, when taking the lateral particle trajectories into account (Braun et al., 2012; Huntington et al., 2007). (4) Finally the rectangularity guaranties as low as possible edge-interferences while having an efficient computing capacity bounding all taken samples.

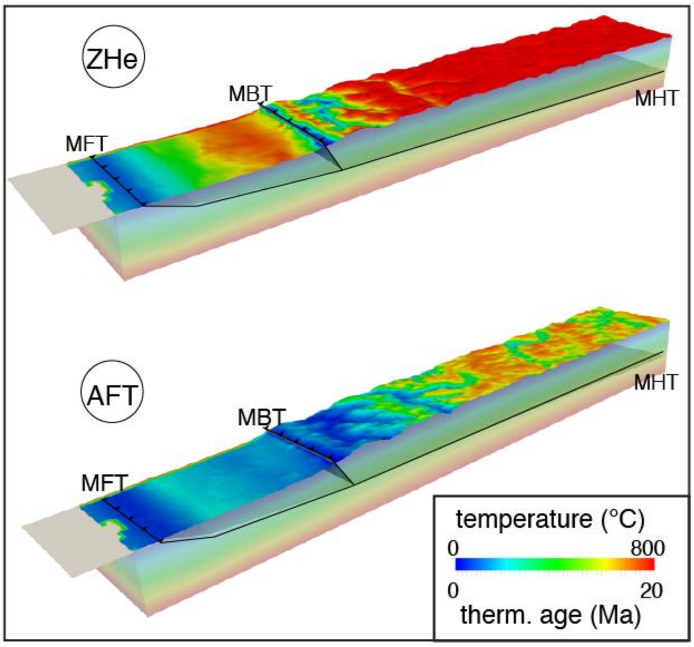

Figure S5.5: 3D representation of the modeled surface ages obtained from the forward model runs. The results show a good correlation between observed and modeled ages, so the Inverse runs had been started on the basis of this forward model. The surface color-coding mentions the modeled surface ages while the coloring in z-direction demonstrates the temperature field.

We extracted the surface topography from a SRTM v2 digital elevation model with a resolution of 90 m per pixel. This resolution was downgraded to around 3 km to (1) allow a fluent performance of the code run and to (2) obtain minimal reasonable results for calculation of ages and exhumation rates. (Coutand et al., 2014; Valla et al., 2011) show that the threshold for acceptable results ranges between 750 m and 1000 m per cell. Above this resolution (smaller cell size) no further improvement of the inversion predictions is attainable, while in contrast lower resolutions (increased cell size) leads to a rising error.

Regardless to this restriction, Valla et al. (2011) also points out that optimal information on relief and denudation can be obtained from a spatial resolution, which covers around 10 % of the topographic wavelength. The valley spacing around the Dhauladhar range is around 30 km with an amplitude of around 3 km. Therefore, the used resolution of 3 km seems to be meaningful. Nevertheless, we conducted several inversions with different resolutions (1 km, 3 km, 9 km), to prove, if there are vast changes within the resulting parameter values and to evaluate the spatial influence of the 3D topography within our area of interest. Besides the three main thrust structures (MFT, MBT, MHT) no additional faults such as the MCT or the contemporaneous frontal fault and Sub-Himalayan thrust belt had been build into the model.

A very good correlation between observed and predicted ages had also been obtained from that geometry (Fig. S5.2, Geometry I). Also, the exhumation rate (Figure S5.2, grey lines, right axis) shows a center of exhumation on spot at the front, giving reasonable high rates for a strongly affected area.

We observed a different situation by extending a deep seated MBT ramp beneath the frontal range (Figure S5.2, Geometry II). While the apparent correlation between the observed and predicted ages and a related distinct age-elevation relationship had been shifted to the Pir Panjal area, the frontal range yields far too young and equally distributed ages.

To prove the absence of a mid-crustal ramp within the Dhauladhar segment, in a third attempt we incorporated a “Nepal-like” setting of the Décollement (Figure S5.2, Geometry III). There, a step along the MHT trace forces the particle paths to bend upwards, producing a higher exhumation rate beneath the Pir Panjal. This “flat-ramp” - structure is also inferred for the neighboring regions, where tectonic windows interpreted as a result from higher exhumation rates above mid-crustal ramps (figure 2, Kishtwar and Rampur).

We also evaluated, if a duplex structure beneath the Pir Panjal range could yield reliable modeled ages (Figure S5.2, Geometry IV). The obtained slow exhumation and the absence of any localized uplift structure also negating the presence of such a stacked thrust sheet structure. Contrary to all prior models, a narrow high-uplift zone evolves at the very orogenic front, but the high exhumation rates stay constant throughout the whole model length and shows only minor variations along its trace.

First we discovered, that the slip rate on the MBT and the related uplift rate, which is closely related to the angle of the fault has the largest influence in the surface age pattern. As can be seen from figure 20 A, the range in ages is largest between 1 mm.a^{-1} and 4 mm.a^{-1} slip rate. The zero rate had been included to investigate a purely temperature driven uplift across the MBT, while the décollement acts as a source of horizontal advection and motion only. Depending on both, slip rate and dip angle, the vertical uplift rate varies between 0.9 mm.a^{-1} and 2 mm.a^{-1}.

Next, we assigned the influx of changing only the angle of the MBT by varying its values in 5 steps between very flat 20° and very steep 60°. Figure S5.4A shows the obtained surface age pattern. The angle mainly effects the ZHe ages at the front while the same thermochronometer remains relatively unaffected across the Pir Panjal. Despite three disturbed AFT ages, the angle has only minor effects on the behavior along both, the front and the interior. The lowest misfit between observed and predicted ages in relation to the frontal fault dip however, lay around 40 - 45°.

We gained an alternative setting from changing only the slip rate on the MBT (Figures S5.3, S5.4). Here low rates show little effects on the ZHe ages at the front and no influences on the interior part. From medium velocities on, its influence is more and more pronounced throughout the whole model length. This is inversely related to the AFT ages, were low slip rates show a vast influx, but high rates produce a smaller cluster. The most favorable slip rate was found at around 2 - 3 mm.a^{-1}.

Further, we explored the effect of variation in the basal temperature of the model (Figure S5.4C). Since the models' thermal field is limited by the afore mentioned Dirichlet boundary condition, where a fixed basal temperature controls the geothermal gradient, a range between 600°C and 1000°C had been applied.

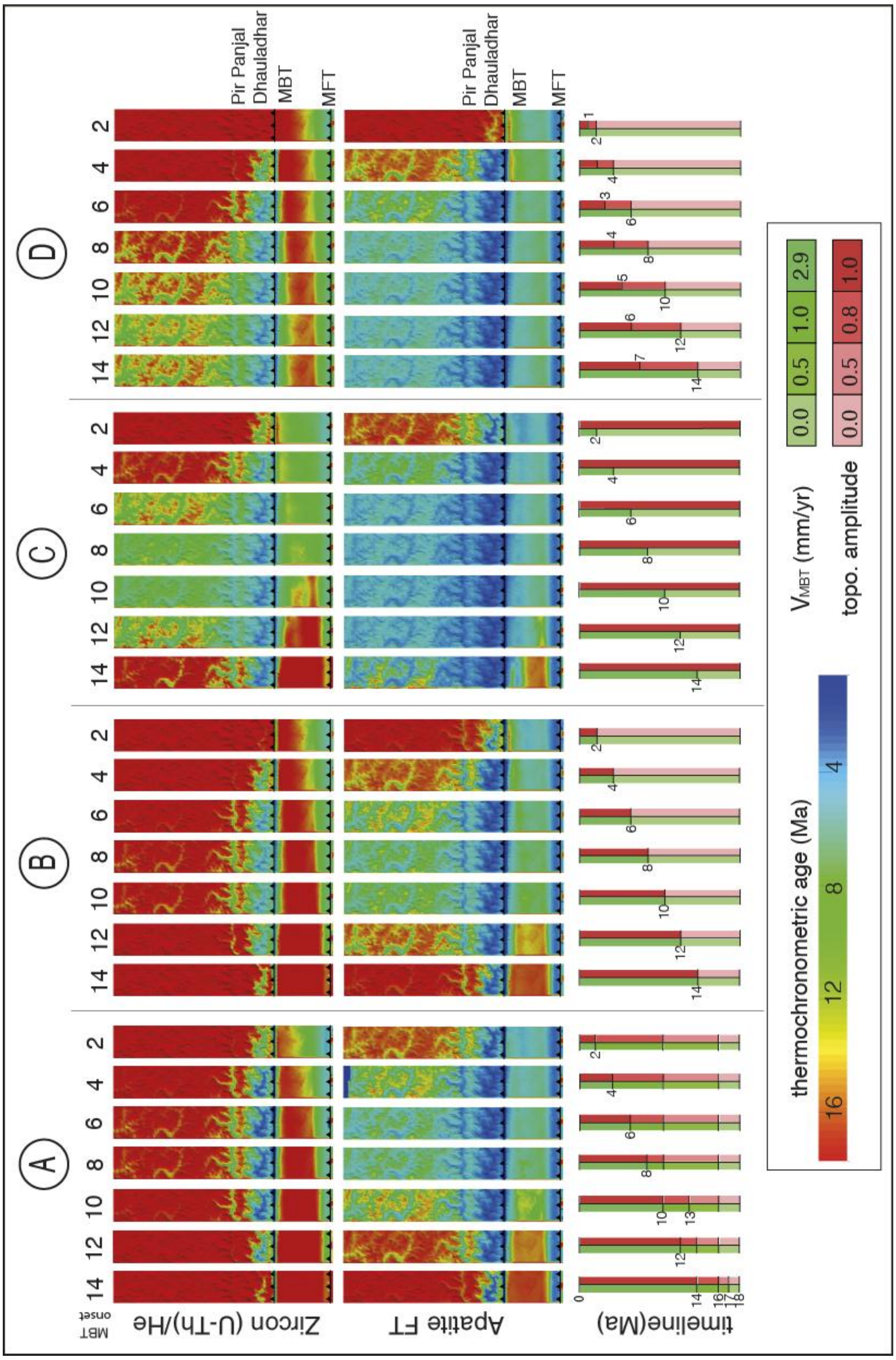

Figure S5.6: *Results of the last modeling attempt, exploring the different MBT onset timings in relation to the denudation induced evolution the topographic amplitude. Note that transit times > 10 Myr seem to be not consistent with the observed surface age pattern. MFT Main Frontal Thrust, MBT Main Boundary Thrust.*

As it is shown in figures S5.3C and 5.4C, changing only the basal temperature has strong effects on the ZHe thermochronometer, while the AFT ages seem to be relatively unviolated, except for lower temperatures. Optimal basal values from 750°C to 800°C had been found, as all ages were determined from the hanging wall of the obducted décollement, which never exceeds shallow crustal depths. The surface age distribution for both, AFT- and ZHe- thermochronometer are presented in figure S5.5.